Durham E-Theses

Bounds on axion parameters from supernova emission

Murphy, Paul

How to cite:

Murphy, Paul (1991) *Bounds on axion parameters from supernova emission*, Durham theses, Durham University. Available at Durham E-Theses Online: http://etheses.dur.ac.uk/6059/

Bounds on Axion Parameters from Supernova Emission

A thesis presented for the degree of

Doctor of Philosophy

by

Paul Murphy

University of Durham
Department of Physics
May 1991

1 4 NOV 1991

Abstract

The strong CP problem and axion theory are introduced. The existing bounds on the axion mass m_a and decay constant F_a are reviewed along with the recent bounds which were derived as a result of the supernova SN1987A.

Current supernova theory is described. The method of terrestrial detection of supernova neutrinos is outlined. The neutrino detections from SN1987A and their importance in confirming theoretical expectations are explained. The methods of obtaining axion constraints from the limits on their production in the newly born neutron star at the centre of a supernova are described. Particular emphasis is placed on the process $NN \rightarrow NNa$, which is known as axion-nucleon-nucleon bremsstrahlung.

The process $pp \rightarrow pp\pi^0$ is studied since this is similar to $NN \rightarrow NNa$. One boson exchange (OBE) models of the inter-nucleon potential are employed. Although OBE Born approximation amplitudes give the right order of magnitude for $\sigma_{pp \rightarrow pp\pi^0}$, a good fit to the data can not be obtained with these alone. Further study would be required to determine the best theoretical form for the $pp \rightarrow pp\pi^0$ matrix element and thus the $NN \rightarrow NNa$ matrix element.

Axion energy production rate in a nascent neutron star is studied. OBE models are used to give a representation for the $NN \rightarrow NNa$ matrix element. Relativistic kinematics is employed. Errors in, and omissions from, the work of previous authors are discussed. It is concluded that, despite various theoretical deficiencies, previous estimates of axion emission rate were not unreasonable. The density dependence of the nucleon mass is briefly considered and it is concluded that large changes in the axion emission rate can result. Further study of this matter would be useful.

Acknowledgements

In memory of my father-in-law

Gerald A. Hayes

15:5:33-12:12:90

His life was gentle, and the elements
So mix'd in him that Nature might stand up
And say to all the world, "This was a man!"

William Shakespeare

Declaration

I declare that no material in this thesis has previously been submitted for a degree at this or any other University.

Statement of Copyright

The metric, spinor and Dirac gamma matrix conventions used in this thesis are those of **F.Halzen and A.D.Martin,** *"Quarks and Leptons: An Introductory Course in Modern Particle Physics."*(Wiley Interscience, 1984).

Contents

1 Introduction

The standard $SU(3)_C \otimes SU(2)_L \otimes U(1)_Y$ model of fundamental interactions is a great success. Indeed, there are no confirmed experimental results that contradict it. As there is a limit to the energies which can be probed using conventional terrestrial accelerator experiments some particle physicists are giving thought to alternative methods of exploring the fundamental interactions and particles. One such method is by considering the stars. Numerous "particle physics experiments" are continually occuring in all astrophysical bodies, as the various constituent particles scatter one another. For instance, in the centre of the Sun proton-proton scattering occurs at a tremendous rate and, in fact, the energy produced by the resulting conversion of hydrogen into helium sustains life on earth. Any disagreement between particle interactions in the real world and the current theoretical model of these interactions may result in a mismatch between the detected and predicted particle flux from astrophysical bodies. The aim of this thesis is to consider a particular hypothetical particle (the axion) and its possible emission from a particular type of astrophysical body (Type II supernovae) and hence put bounds on the axion parameters.

One unsatisfactory aspect of the standard model of fundamental interactions is that it does not offer an explanation as to why the strong interactions, which are described by the $SU(3)_c$ sector of the model, should respect Charge-Parity (CP) invariance. This unsatisfactory aspect is known as "The Strong CP Problem". The axion is a hypothetical particle which is an essential element of a possible solution of the strong CP problem which is particularly pleasing aesthetically. This solution, which is a straightforward extension of the standard model, was proposed by R.D.Peccei and H.R.Quinn[1,2]. Although the original axion model has been experimentally rejected, variant "invisible" axion models have been developed which, as yet, have not been ruled out.

At present there is no positive hint to suggest that the axion exists. The acceptable range for the properties of the axion can be constrained by particle physics experiments, astrophysical observations and cosmological considerations. Astrophysical observations give more restrictive contraints than do terrestrial particle physics experiments. All stellar objects are potential axion emitters. By demanding that axion emission from various stars is insignificant and does not al-

ter the confirmed predictions of current astrophysical models one can constrain the parameters of axion models. The strong CP problem, the axion and the present constraints on axion model parameters are discussed in Chapter 2.

In early 1987 both light and neutrinos from a nearby supernova explosion, code named SN1987A, were detected on earth. The measurements of the properties of particles which were emitted by this event, were in general agreement with contemporary astrophysical models of supernovae. This agreement provided another astrophysical scenario through which one could constrain the axion's properties. In Chapter 3 current supernovae theory is outlined with reference to the importance of SN1987A as confirmation of the general predictions of the theory. The axion bounds which can be subsequently derived are also discussed.

The dominant axion production mechanism in the nascent neutron star which forms at the centre of a supernova is axion-nucleon-nucleon bremsstrahlung $NN \rightarrow NNa$. Obviously this process cannot be examined experimentally and so the cross-section for axion production must be calculated from a theoretical model for the relevant matrix element. A similar process to $NN \rightarrow NNa$ is pion production in proton-proton scattering $pp \rightarrow pp\pi^0$. The process $pp \rightarrow pp\pi^0$ can and has been experimentally studied. Thus $pp \rightarrow pp\pi^0$ provides a potentially useful test bed for assumptions concerning the $NN \rightarrow NNa$ matrix elements. One boson exchange models of the pion production matrix element are discussed in Chapter 4 and are used to compute the cross-section for the process.

In Chapter 5 axion production in a nascent neutron star due to the process $NN \rightarrow NNa$ is discussed. Chapter 5 includes a critical account of the approximations used and the errors introduced by previous authors. A more complete treatment of the emission rate due to $NN \rightarrow NNa$ is presented and used to determine, at least in order of magnitude, the corrections to the emission rates which have been computed by other authors. Also, the effect these changes may have on previously derived axion bounds is discussed.

2 Axion Theory and Axion Bounds

In this chapter I shall outline the basic principles of axion theory. Also, in Section 2.4, I shall give a brief review of the present limits that have been obtained experimentally or otherwise. Good, general references for this chapter are, Sikivie[3,4], Raffelt[5], Cheng[6] and Kim[7].

2.1 The Strong CP Problem

Strong interactions conserve CP and P to a high degree of accuracy. Simply stated, the strong CP problem is the problem of explaining why this is the case.

The naive QCD Lagrangian, describes the interaction between quark fields q_i of flavour i and real mass m_i via gluon exchange,

$$\mathcal{L}_{QCD} = \sum_{i=1}^{N_f} [\bar{q}_i(i\gamma^\mu D_\mu)q_i - m_i(\bar{q}_{i_L}q_{i_R} + \bar{q}_{i_R}q_{i_L})] - \text{Tr}\left[G_{\mu\nu}G^{\mu\nu}\right]/(2g^2) \qquad (2.1)$$

where N_f is the number of quark flavours, $G_{\mu\nu}$ is the gluon field strength tensor, g is the strong coupling constant, D_μ is the covariant derivative and $q_{i_{R,L}} = (1\pm\gamma^5)q_i$ are the left, right components of the quark field q_i. This Lagrangian, with real quark masses, does conserve CP and P. However, this is not the whole story.

The quark masses in the QCD Lagrangian originate in the weak sector of the standard model[8]. Since CP is not conserved in weak interactions one must allow for complex quark masses in general. Complex masses imply CP violation since $i\bar{q}\gamma_5 q = i(\bar{q}_L q_R - \bar{q}_R q_L)$ is odd under P and CP.

Furthermore, the QCD vacuum is a superposition of vacuum states[9] each of which has a different topological charge, n, *i.e.*

$$|\theta_v\rangle = \sum_n e^{in\theta_v}|n\rangle, \qquad (2.2)$$

where $|\theta_v\rangle$ is the QCD vacuum, and $|n\rangle$ is a particular vacuum state of topological charge n, defined by

$$n = -\frac{1}{16\pi^2}\int Tr(G_{\mu\nu}\tilde{G}^{\mu\nu})d^4x, \qquad (2.3)$$

3

with

$$\tilde{G}_{\mu\nu} = \frac{1}{2}\epsilon_{\mu\nu\rho\sigma}G^{\rho\sigma}, \quad (\epsilon_{0123} = -1). \qquad (2.4)$$

So, if we insist on employing a single vacuum state for the theory, e.g. the one with $n = 0$, then to mimic the effect of the $e^{in\theta_v}$ terms in (2.2), the term

$$\mathcal{L}_{\theta_v} = -n\theta_v = \frac{\theta_v}{16\pi^2}\text{Tr}\left[G_{\mu\nu}\tilde{G}^{\mu\nu}\right], \qquad (2.5)$$

must be added to the QCD Lagrangian. This term also violates CP by virtue of the antisymmetric tensor, $\epsilon_{\mu\nu\rho\sigma}$, in the definition of $\tilde{G}_{\mu\nu}$, (2.4).

Introducing the above two ideas into the QCD Lagrangian gives

$$\mathcal{L}'_{QCD} = \sum_{i=1}^{N_f}[\bar{q}_i(i\gamma^\mu D_\mu)q_i - m_i\bar{q}_{i_L}q_{i_R} - m_i^*\bar{q}_{i_R}q_{i_L}]$$

$$-\text{Tr}\left[G_{\mu\nu}G^{\mu\nu}\right]/(2g^2) + \frac{\theta_v}{16\pi^2}\text{Tr}\left[G_{\mu\nu}\tilde{G}^{\mu\nu}\right], \qquad (2.6)$$

which explicitly violates P and CP. Note that the last term in (2.6) is a 4-divergence and hence only contributes surface terms to the Lagrangian. However, due to the existence of colour instantons which enable vacuum-to-vacuum transitions to occur, the full θ-vacuum of QCD must be taken into account and the last term of (2.6) does have physical consequences[9].

Using $SU(N_f) \otimes U(1)_V$ transformations one can give all the quark masses the same phase, i.e.

$$m_i = |m_i|e^{i\delta}, \qquad (2.7)$$

A $U(1)_A$ transformation ($q_i \rightarrow q_i e^{i\alpha\gamma_5}$) gives an infinitesimal change in the Lagrangian of

$$\delta\mathcal{L}_A = \sum_{i=1}^{N_f} 2im_i\alpha\bar{q}_i\gamma_5 q_i - \frac{2\alpha N_f}{16\pi^2}\text{Tr}\left[G_{\mu\nu}\tilde{G}^{\mu\nu}\right] \qquad (2.8)$$

The second term in (2.8) arises because of the Adler-Bell-Jackiw (ABJ) anomaly in the axial current. One can use an axial rotation *either* to eliminate the θ_v term,

4

or to rotate δ to zero thus giving the quarks real masses. However, the effective θ-term

$$\mathcal{L}_{\overline{\theta}} = \frac{\overline{\theta}}{16\pi^2} \text{Tr}\left[G_{\mu\nu}\tilde{G}^{\mu\nu}\right], \tag{2.9}$$

with $\overline{\theta} = \theta_v - N_f\delta$, is unchanged by axial rotations of the quark fields.

One consequence of strong CP violation is to give the neutron an electric dipole moment. Experimental limits on the neutron electric dipole moment give an upper limit on $\overline{\theta}$ of 10^{-8}[10,11]. The strong CP problem asks why $\overline{\theta}$ is so small. Since $N_f\delta$ and θ_v originate in different sectors of the standard model there is no reason, a priori, to expect that these two parameters will cancel.

It is worth noting that if just one of the quark masses were zero one could use the $SU(N_f) \otimes U(1)_V$ transformations to set $\delta = \theta_v/N_f$ and hence $\overline{\theta} = 0$. It is, however, unlikely that any of the quark "current" masses are zero since zero quark masses are inconsistent with current algebra estimates.

2.2 The Peccei-Quinn Mechanism

Peccei and Quinn[1,2] devised a method of setting $\overline{\theta}$ to zero dynamically which can be used when none of the quarks has zero mass. Their method employs an alternative Lagrangian in which the quark mass terms are replaced by Yukawa interactions with a scalar field. The simplest version of such a Lagrangian is:

$$\mathcal{L}_{PQ} = \sum_{i=1}^{N_f}[\overline{q}_i(i\gamma^\mu D_\mu)q_i - K_i\phi\overline{q}_{i_L}q_{i_R} - K_i^*\phi^\dagger\overline{q}_{i_R}q_{i_L}]$$

$$-\text{Tr}\left[G_{\mu\nu}G^{\mu\nu}\right]/(2g^2) + \frac{\theta_v}{16\pi^2}\text{Tr}\left[G_{\mu\nu}\tilde{G}^{\mu\nu}\right] + V(\phi^\dagger\phi). \tag{2.10}$$

The scalar potential $V(\phi^\dagger\phi)$ is a Higgs potential and the quark masses, $m_i = K_i\langle\phi\rangle$, will be generated upon spontaneous symmetry breakdown when $\langle\phi\rangle \neq 0$.

If there were no chiral anomaly in the axial vector current, (2.10) would be invariant under the chiral transformation,

$$q_i \rightarrow e^{i\alpha\gamma_5}q_i \quad , \quad \phi \rightarrow e^{-2i\alpha}\phi, \tag{2.11}$$

which is known as the Peccei-Quinn symmetry, $U(1)_{PQ}$. This quasi-symmetry can be used to eliminate the θ_v-term in the Lagrangian via the ABJ anomaly.

The $SU(N_f) \otimes U(1)_V$ transformations can then be used to give all the Yukawa couplings, K_i, the same phase δ, i.e.,

$$K_i = |K_i| e^{i\delta}. \tag{2.12}$$

One can then absorb $e^{i\delta}$ into a global redefinition of the ϕ field and thus make $\mathcal{L}_{PQ}$ manifestly CP conserving, with $\theta_v = 0$ and real Yukawa couplings. It is natural that $\overline{\theta} = 0$ in this theory. However, it is possible to improve on this and show that $\overline{\theta} = 0 (\text{mod } \pi)$.

The minimum of the Higgs potential occurs at

$$\phi_v = v e^{i\omega}. \tag{2.13}$$

The vacuum of the theory could lie anywhere on the circle in the complex plane defined by equation (2.13). Once a particular direction, i.e. the value of ω, is chosen the $O(1)$ symmetry of (2.10) is broken. The scalar potential is indifferent to the value of ω. However, ω is not indifferent in the full theory because of the ABJ anomaly; its value can be determined.

Starting from $\mathcal{L}_{PQ}$ we first use $U(1)_{PQ}$ to set $\theta_v = 0$ and $SU(N_f) \otimes U(1)_V$ to give all the K_i's the same phase as before. We shall keep $\delta \neq 0$, however. ω can be determined by minimising the Yukawa interaction energy

$$\langle \sum_{i=1}^{N_f} (K_i \overline{q}_{i_L} q_{i_R} \phi + K_i^* \overline{q}_{i_R} q_{i_L} \phi^\dagger) \rangle_0 = \sum_{i=1}^{N_f} |K_i| \langle \overline{q}_{i_L} q_{i_R} \rangle v \cos(\delta + \omega), \tag{2.14}$$

where it has been assumed that the quark condensates $\langle \overline{q}_{i_L} q_{i_R} \rangle$ are real. This is probable for $\theta_v = 0$[3].

The minimum of (2.14) occurs for

$$\omega = \pi - \delta, \tag{2.15}$$

which substituted in (2.13) gives $\langle \phi \rangle = -v$ as the vacuum of the theory. Substi-

6

tuting this vacuum expectation value into $\mathcal{L}_{PQ}$ gives

$$m_i = -|K_i|v \tag{2.16}$$

and

$$\bar{\theta} = \theta - \arg(m_1...m_{N_f}) = n\pi = 0(\mathrm{mod}\ \pi). \tag{2.17}$$

It can be shown that θ is cyclic with period 2π when quarks are present[3]. Obviously $\bar{\theta}$ is therefore also cyclic. Since $\bar{\theta} \to -\bar{\theta}$ under P and CP, there are two P and CP conserving values for $\bar{\theta}$, 0 and π. The result (2.17) thus tells us that $\mathcal{L}_{PQ}$ solves the strong CP problem.

2.3 The Axion

The axion, a, is the pseudo-Goldstone boson associated with the spontaneous breaking of the Peccei-Quinn quasi-symmetry, $U(1)_{PQ}$. Taking $\theta = \delta = 0$ and hence $\omega = \pi$, the axion field can be defined by:

$$\begin{aligned}\phi &= ve^{i(\pi - \frac{a}{v})} + \eta, \\ &= \langle\phi\rangle + ia + \eta + O(\frac{a^2}{v}),\end{aligned} \tag{2.18}$$

where η is a heavy particle.

One can estimate the mass of the axion by substituting $(\pi - \frac{a}{v})$ for ω in the Yukawa interaction energy, *i.e.*

$$-(\sum_{i=1}^{N_f} |K_i|\langle\bar{q}_i q_i\rangle)v[1 - \frac{1}{2}(\frac{a}{v})^2] = constant + \frac{1}{2}m_a^2 a^2 + O(\frac{a^4}{v^4}), \tag{2.19}$$

with

$$\begin{aligned}m_a &= \sqrt{(\sum_{i=1}^{N_f} |K_i|\langle\bar{q}_i q_i\rangle)/v} \\ &= \sqrt{\sum_q m_q\langle\bar{q}q\rangle/v^2} \approx \frac{F_\pi m_\pi}{v},\end{aligned} \tag{2.20}$$

where F_π is the pion decay constant. This evaluation of the axion mass is very crude since it neglects the mixing of the axion with $\pi^0, \eta \ldots$ *etc.* A more accurate

7

result which includes this mixing is

$$m_a \simeq \frac{F_\pi m_\pi}{v} N_f \sqrt{\frac{z}{(1+z+w)(1+z)}},$$

(2.21)

where $z \equiv m_u/m_d \simeq 0.568$ and $w \equiv m_u/m_s \simeq 0.029$.

2.3.1 The Peccei-Quinn-Weinberg-Wilczek Axion

That the Peccei-Quinn mechanism implies the existence of the axion was realised by Weinberg[12] and Wilczek[13]. The standard axion model which incorporates the Peccei-Quinn mechanism into the Weinberg-Salam model is known as the Peccei-Quinn-Weinberg-Wilczek (PQWW) axion. To make the Peccei-Quinn mechanism compatible with the standard $SU(3)_C \otimes SU(2)_L \otimes U(1)_Y$ model of fundamental interactions, one must introduce a second Higgs doublet. The quark Yukawa couplings and the Higgs potential are chosen to have the form:

$$-\sum_{i,j=1}^{\frac{N_f}{2}} [K_i^{u_j} (\overline{u}_{i_L} \quad \overline{d}_{i_L}) \begin{pmatrix} \phi_1^0 \\ \phi_1^- \end{pmatrix} u_{j_R} + K_i^{d_j} (\overline{u}_{i_L} \quad \overline{d}_{i_L}) \begin{pmatrix} -\phi_2^{-*} \\ \phi_2^{0*} \end{pmatrix} d_{j_R}$$

$$+ \text{ Hermitian conjugate}] - V(\phi_1^\dagger \phi_1, \phi_2^\dagger \phi_2, (\phi_1^\dagger \phi_2)(\phi_2^\dagger \phi_1)).$$

(2.22)

The classical action density is invariant under the PQ symmetry

$$q_j \rightarrow e^{i\alpha\gamma_5} q_j,$$
$$\phi_1 \rightarrow e^{-2i\alpha} \phi_1$$
$$\text{and} \quad \phi_2 \rightarrow e^{-2i\alpha} \phi_2.$$

(2.23)

which is broken by the QCD gluon anomaly. The axion is now

$$a = (v_1 \text{Im} \phi_1^0 - v_2 \text{Im} \phi_2^0)/\sqrt{v_1^2 + v_2^2}.$$

(2.24)

The simple axion mass equations (2.20), (2.21) still hold in order of magnitude with $v = \sqrt{v_1^2 + v_2^2} \simeq 250 GeV$. From (2.21) this gives $m_a \approx 100 keV$. Such an axion has not been found in the laboratory and the PQWW axion is effectively ruled out [7]. The terrestrial limits on axion existence are discussed in Section 2.4.1.

2.3.2 The Invisible Axion

In the PQWW axion model $U(1)_{PQ}$ is broken at the electroweak breaking scale, $v \simeq 250 GeV$. However, it is alternatively possible to break $U(1)_{PQ}$ at a much larger energy scale. This implies, through (2.21), that the axion becomes very light and, since the axion couplings are inversely proportional to v (see Section 2.3.4 below), very much decoupled. The predicted rates of axion production in the laboratory can, in this way, be made so small that the axion would be "invisible" to all laboratory experiments. This possibility was pointed out by Kim[14] and Dine, Fischler and Sredniki[15]. The Dine-Fischler-Sredniki (DFS) model has the following scalar sector,

$$
-\sum_{i,j=1}^{\frac{N_f}{2}} [K_i^{u_j} (\, \overline{u}_{i_L} \quad \overline{d}_{i_L} \,) \begin{pmatrix} \phi_1^0 \\ \phi_1^- \end{pmatrix} u_{j_R} + K_i^{d_j} (\, \overline{u}_{i_L} \quad \overline{d}_{i_L} \,) \begin{pmatrix} -\phi_2^{-*} \\ \phi_2^{0*} \end{pmatrix} d_{j_R}
$$

$$
+ \text{Hermitian conjugate}] - V(\phi_1^\dagger \phi_1, \phi_2^\dagger \phi_2, (\phi_1^\dagger \phi_2)(\phi_2^\dagger \phi_1), \Phi^\dagger \Phi, (\phi_1^\dagger \phi_2)\Phi), \tag{2.25}
$$

where Φ is an $SU(3)_C \otimes SU(2)_L \otimes U(1)_Y$ singlet scalar field. The classical action density is invariant under the PQ symmetry

$$
\begin{aligned}
q_j &\to e^{i\alpha\gamma_5} q_j, \\
\phi_1 &\to e^{-2i\alpha} \phi_1, \\
\phi_2 &\to e^{-2i\alpha} \phi_2 \\
\text{and} \quad \Phi &\to e^{-2i\alpha} \Phi,
\end{aligned} \tag{2.26}
$$

which is broken only by the gluon anomaly. The axion is now

$$
a = (v_1 \text{Im}\phi_1^0 - v_2 \text{Im}\phi_2^0 + v_\Phi \text{Im}\Phi)/v, \tag{2.27}
$$

where $v = \sqrt{v_1^2 + v_2^2 + v_\Phi^2}$ and $v_\Phi = \langle \Phi \rangle$. Since Φ is an $SU(3)_C \otimes SU(2)_L \otimes U(1)_Y$ singlet field v_Φ, and hence v, can be much larger than 250GeV. Constraints on the symmetry breaking scale will be discussed in Section 2.4.

2.3.3 Alternative Axion Models

It is, of course, possible to construct a number of axion models by changing the structure of the scalar sector of the theory but the two previous models are

9

probably the most important. One extension of these is worth mentioning, this is the "hadronic" axion model[7]. In the hadronic axion model the axion only couples through its mixing with the pion and does not have any couplings to the fundamental fermions.

In a general PQ scheme, several conventional, or exotic, quark fields q_j may participate in the PQ symmetry transformations. In general, the transformation of each field under $U(1)_{PQ}$ is characterised by its Peccei-Quinn charge, X_j, according to

$$q_{j_L} \to e^{iX_j\alpha/2}q_{j_L}.$$ (2.28)

The so-called colour anomaly,

$$N = \sum_j X_j,$$ (2.29)

enters into many general expressions which will be discussed in the following section.

2.3.4 The Axion Couplings

The coupling of the axion to a fermion, f, can be written as

$$\mathcal{L}_{a\bar{f}f} = g_{af}\bar{f}\gamma_\mu\gamma_5 f\partial^\mu a = \frac{c_f}{2F_a}\bar{f}\gamma_\mu\gamma_5 f\partial^\mu a,$$ (2.30)

where c_f is a model dependent constant, typically of the order unity, and F_a is the axion decay constant. Different notations and normalisation conventions for F_a exist in the literature. I shall use F_a such that $F_a = (f_a)_{Raffelt}$ where $(f_a)_{Raffelt}$ is the decay constant used by Raffelt[5]. One expects that F_a is of the order of v since this is the scale of the symmetry breaking which is the only scale in the theory. The exact value of F_a can be computed in terms of the vacuum expectation values of the scalar fields employed in a particular model. A general method of doing this is given by Sikivie [4]. For the present purposes we note that F_a is of the order of v and that in the DFS model of (2.25), for example,

$$F_a = N\sqrt{v_\Phi^2 + \frac{4v_1^2 v_2^2}{v_1^2 + v_2^2}}.$$ (2.31)

In terms of F_a the axion mass equation (2.21) becomes[5]

$$m_a \simeq \frac{F_\pi m_\pi}{F_a}\sqrt{\frac{z}{(1+z+w)(1+z)}} \simeq \left(\frac{0.6 \times 10^7 GeV}{F_a}\right)eV. \qquad (2.32)$$

The constant c_f in (2.30) has two contributions. The first is from the direct coupling of the axions to fermions via the Yukawa interaction terms in the theory. The second is due to the mixing of the axion with the mesons $\pi, \eta \ldots etc.$ which occurs when the quark condensates $\langle \bar{q}q \rangle$ form. This complicates the determination of the axion coupling to fermions which also couple to pions. We will meet this complication later in the section when we consider axion-nucleon couplings. For electrons there is no axion-pion mixing term. In the DFS axion model

$$c_e = \frac{\cos^2 \beta}{N_{fm}}, \qquad (2.33)$$

where $\cot \beta$ is the ratio of the weak sector vacuum expectation values (v_1/v_2) in the DFS model and $N_{fm} \geq 3$ is the number of quark families. In a hadronic axion model the axion does not couple to electrons so $c_e = 0$.

There has been a great deal of confusion in the literature as to whether one should use a pseudovector axion-fermion coupling as in (2.30) or a pseudoscalar axion-fermion coupling of the form $m_f c_f (\bar{q}\gamma_5 q)/F_a$. The situation has been clarified by Iwamoto[16] and Careena and Peccei[17]. The pseudovector (axial-vector) current $J_{5\mu} \bar{f}\gamma_\mu \gamma_5 f$ is conserved at the classical level in the chiral fermion limit $(m_f = 0)$. The related pseudovector coupling is the correct coupling to use for the Nambu-Goldstone boson (axion, pion,...) associated with the spontaneous breaking of $U(1)_A$. The pseudoscalar coupling is only equivalent to the pseudovector coupling when it is sandwiched between on-shell fermions, *i.e.* fermions which satisfy the free particle Dirac equation (see Section 4.2.2). One cannot continue to employ the simpler pseudoscalar coupling if the axion couples to off-shell propagator fermions for which this equivalence no longer holds. It is therefore preferable to stick to using the pseudovector coupling so as to be correct in all cases.

The mixing of the axion with the pion also leads to an axion photon coupling of the form[5]

$$\mathcal{L}_{a\gamma\gamma} = \frac{c_\gamma \alpha}{8\pi F_a}F_{\mu\nu}\tilde{F}^{\mu\nu}a \qquad (2.34)$$

where $\tilde{F}_{\mu\nu} = (1/2)\epsilon_{\mu\nu\rho\sigma}F^{\rho\sigma}$, $\alpha \simeq 1/137$ is the electromagnetic fine structure con-

stant, $F_{\mu\nu}$ is the electromagnetic field strength tensor and c_γ is again a model dependent constant. A general expression for c_γ is

$$c_\gamma = \frac{E}{N} - \frac{2}{3}\frac{4+z+w}{1+z+w} \simeq \frac{E}{N} - 1.92, \qquad (2.35)$$

where $z \equiv m_u/m_d \simeq 0.568$, $w \equiv m_u/m_s \simeq 0.029$ and E is the model dependent coefficient of the electromagnetic anomaly. For typical GUT axion models $E = 8N/3$[5]. The most important thing to note about the axion couplings is that they are inversely proportional to F_a so that the axion is less strongly coupled for large F_a.

The axion-nucleon coupling is the most important axion coupling in nascent neutron stars which will be considered in later chapters. These couplings have been described by Kaplan [18], Srednicki[19] and Mayle et al. [20,21]. The constants c_n and c_p are given by

$$c_p = \left(c_u - \frac{1}{K}\right)\Delta u + \left(c_d - \frac{z}{K}\right)\Delta d + \left(c_s - \frac{w}{K}\right)\Delta s,$$
$$c_n = \left(c_u - \frac{1}{K}\right)\Delta d + \left(c_d - \frac{z}{K}\right)\Delta u + \left(c_s - \frac{w}{K}\right)\Delta s, \qquad (2.36)$$

where $K = 1 + z + w$. For a given quark flavour, q, the interaction strength with protons depends on the proton fraction δq of the spin carried by this flavour, i.e. $S_\mu \Delta q \equiv \langle p|\bar{q}\gamma_\mu\gamma_5 q|p\rangle$ where S_μ is the proton spin. The parameters Δq have to be determined experimentally. From deep inelastic scattering measurements it is found that

$$\Delta u = \Delta s + 0.966$$

and

$$\Delta d = \Delta s - 0.284.$$

The value of Δs is, as yet, uncertain. In the naive quark model one assumes that strange quarks do not carry any of the proton spin and thus $\Delta s = 0$. However, recent measurements by the European Muon Collaboration indicate that $\Delta s \neq 0$. It is found that $\Delta s = -0.257$ [22], which is supported by analyses of elastic

neutrino proton scattering which yield $\Delta s = -0.15 \pm 0.09$ [23,24]. As for the constants c_u, c_d and c_s, in the DFS model

$$c_u = \frac{\sin^2 \beta}{N_{fm}} \tag{2.37}$$

and

$$c_d = c_s = \frac{\cos^2 \beta}{N_{fm}}; \tag{2.38}$$

while in the hadronic axion model

$$c_u = c_d = c_s = 0, \tag{2.39}$$

so the nucleon coupling comes only from the pion mixing factors.

2.4 Bounds on Axion Parameters

Once we know the axion couplings we can calculate, in principle, the cross-sections for reactions involving the axion. This allows us to derive bounds on the parameters involved in axion models, in particular, the axion coupling constants and, as a result, the axion decay constant, F_a, and mass, m_a. Axion bounds have been derived in a variety of ways. In the following sections I shall review the present status of axion bounds. As a general statement we can say that the region for F_a which cannot yet be excluded experimentally covers only a few orders of magnitude, but it is still possible that the axion exists in a limited mass range. The impact of the existence, or otherwise, of the axion goes beyond its ability to solve the strong CP problem. The axion is also important to cosmologists in that it may provide a solution to the infamous "missing mass problem".

2.4.1 Terrestrial Bounds

There are several particle physics experiments which are relevant for constraining axion parameters. The principle consequence of the experimental limits derived from axion reactions is to raise of the acceptable value of F_a much above the electroweak scale. This, of course eliminates the PQWW axion. The invisible axion

models are virtually unaffected by the restrictions imposed by particle physics experiments. The review by Kim [7] covers these laboratory bounds in some detail and the bounds are also quoted in the Particle Data Group Tables [25]. Here, I shall quote a selection of the experimental results which are taken from the Particle Data Group Tables [25] in which the original references can be found.

i) K meson decay

For example, there is a limit on the $K^+ \to \pi^+ a$ branching ratio of

$$BR(K^+ \to \pi^+ a) < 3.8 \times 10^{-8}. \tag{2.40}$$

ii) Heavy quarkonium decays

The branching ratios for the decays $\Upsilon \to a\gamma$ and $J/\psi \to a\gamma$ have been bounded, for example,

$$BR(\Upsilon \to a\gamma) < 9.1 \times 10^{-4} \tag{2.41}$$

and

$$BR(J/\psi \to a\gamma) < 1.4 \times 10^{-5}. \tag{2.42}$$

iii) Nuclear transitions

Many bounds have been placed on axion emission in nuclear transitions, for example,

$$BR(^{12}C^* \to^{12} C\ a) < 1.5 \times 10^{-4}. \tag{2.43}$$

The above BR bounds, together with other similar laboratory bounds, eliminate the possibility of a weak interaction scale axion and give a bound on F_a,

$$F_a \gtrsim 10^3 GeV, \tag{2.44}$$

i.e.

$$m_a \lesssim 6\ keV. \tag{2.45}$$

2.4.2 Astrophysical Bounds

The above terrestrial bounds on the axion are not very restrictive. Much more restrictive bounds have been derived by considering the effect of axion emission on
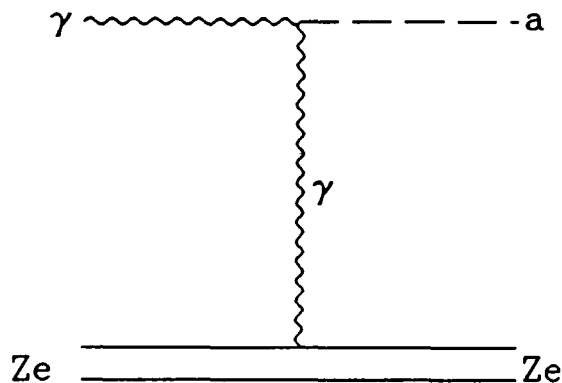
Figure 2.1 The Primakoff Axion Production Process.

the models of various astrophysical bodies. The bounds thus derived depend on the theoretical model for the astrophysical body in question. One must therefore bear in mind that any change in the standard astrophysical model may change the bounds on the axion parameters. Fairly comprehensive reviews can be found in Pantziris and Kang [26] and Kim [7], although these do not include the recent work on supernovae bounds which resulted from SN1987A. A recent review by Raffelt [5] is very comprehensive. In the following sections I shall quote some of the lower bounds on F_a which have been derived by considering astrophysical bodies. This should give a good indication of the possibilities. For more details I refer the reader to Raffelt[5].

2.4.2.1 The Sun

The dominant axion production processes in the Sun are the Primakoff process as shown in Figure 2.1 and the Compton-like process as shown in Figure 2.2. Axions can also be produced via the bremsstrahlung emission process, $e^-(Z, A) \rightarrow (Z, A)e^-a$.

15
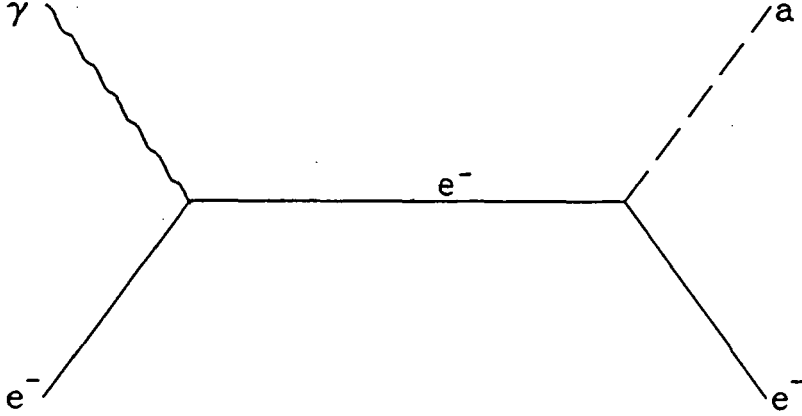
Figure 2.2   The Compton-like Axion Production Process, $\gamma e^- \to a e^-$.

One obtains a limit on the axion coupling by requiring that the total axion luminosity be less than the known solar luminosity, *i.e.* $L_a < L_\odot$. The axion luminosity due to the Compton-like and axion bremsstrahlung processes is found to be[27]

$$L_a = 6.0 \times 10^{21} L_\odot \frac{m_e^2}{\pi} g_{ae}^2.$$ (2.46)

so the condition $L_a < L_\odot$ gives a bound on the axion electron coupling of

$$g_{ae} \lesssim 4.5 \times 10^{-7} GeV^{-1},$$ (2.47)

which for the DFS axion with $\cos\beta = 1/\sqrt{2}$, *i.e.* $c_e = 1/6$ in (2.33), gives from (2.32),

$$F_a \gtrsim 2 \times 10^5 \; GeV$$ (2.48)

and

$$m_a \lesssim 30 eV.$$ (2.49)

16

The axion luminosity resulting from the Primakoff process is found to be [27]

$$L_a = 1.7 \times 10^{17} L_\odot g_{a\gamma}^2, \qquad (2.50)$$

for which $L_a < L_\odot$ gives a limit on the axion-photon-photon coupling of

$$g_{a\gamma} \lesssim 2.4 \times 10^{-9}. \qquad (2.51)$$

Taking a typical value for c_γ of 0.75 the resulting limits on the axion decay constant and the axion mass are

$$F_a \gtrsim 3.6 \times 10^5 GeV \qquad (2.52)$$

and

$$m_a \lesssim 17 eV. \qquad (2.53)$$

It is assumed in deriving the above, and indeed the majority of the astrophysical constraints, that the axion coupling to matter is so weak that the axions, once produced, leave the star without any other interactions.

2.4.2.2 Red Giants and the Horizontal Branch Stars

During a star's red giant phase the helium core of the star increases in mass. As this occurs the core temperature and density increase. Eventually the conditions become such that helium burning can occur. If axions exist, the additional cooling that their emission provides could prevent helium ignition. Using this argument Dearborn, Schramm and Steigman[28] derived a limit on the axion electron coupling by considering axion production via axion bremsstrahlung $e^- + (Z, A) \rightarrow e^- + (Z, A) + a$. They found [†] that helium can ignite providing

$$\frac{c_e m_e}{F_a} \leq 3 \times 10^{-13}, \qquad (2.54)$$

In the DFS axion model $c_e = \cos^2 \beta$ where $\cot \beta = v_1/v_2$, v_1 and v_2 being the weak sector Higgs vacuum expectation values. If $c_e = 1/6$ the bounds on F_a and m_a

---

[†] The bound given here is taken from Raffelt[5] and includes a correction to the emission rate used by Dearborn, Schramm and Steigman[28].

implied by the above are

$$F_a \gtrsim 2.8 \times 10^8 GeV \tag{2.55}$$

and

$$m_a \lesssim 0.02 eV. \tag{2.56}$$

For the hadronic axion $c_e = 0$ so no bound can be given.

Axion emission can reduce the time a star spends in its helium burning stage on the horizontal branch of the Hertzsprung-Russell diagram. By considering this reduction of the helium burning lifetime, Raffelt and Dearborn[29] derived a limit on the axion-photon coupling. The Primakoff process is the relevant axion production process. They found a bound of

$$\frac{c_\gamma \alpha}{2\pi F_a} < 10^{-10} GeV^{-1}, \tag{2.57}$$

i.e.

$$\frac{c_\gamma}{F_a} < 8.6 \times 10^{-8} GeV^{-1}, \tag{2.58}$$

which gives, for $c_\gamma = 0.75$,

$$F_a \gtrsim 8.7 \times 10^6 \ GeV \tag{2.59}$$

and

$$m_a \lesssim 0.7 \ eV. \tag{2.60}$$

2.4.2.3 White Dwarfs

By considering the effect of axion emission on the white dwarf cooling curve Nakagawa *et al* [30] have derived a limit on the axion-electron coupling of

$$\frac{c_e m_e}{F_a} \leq 3.7 \times 10^{-13}, \tag{2.61}$$

which is slightly less restrictive than the Red Giant bound discussed in the last section.

18
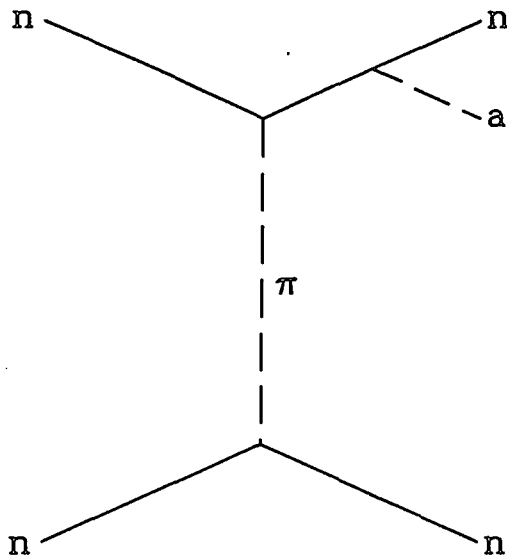
Figure 2.3   Neutron-Neutron-Axion Bremsstrahlung, $nn \rightarrow nna$.

2.4.2.4 Neutron Stars

Neutron stars have high core temperatures ($T_c \sim 10^9 K$) and core densities ($\rho_c \sim 10^{15} \ g \ cm^{-3}$). Under these conditions the dominant axion energy loss mechanism is via axion bremsstrahlung from neutron-neutron scattering as shown in Figure 2.3.

The diagram in Figure 2.3 represents an approximation which will be discussed in much more detail in Chapters 4 and 5.

At high temperatures the axion bremstrahlung loss could be greater than the neutrino energy loss. This has been considered by Iwamoto[31] and Pantziris and Kang[26]. Pantziris and Kang used an incorrect axion emission formula; they mistakenly used the pseudoscalar coupling to nucleons for both the axion and the pion. Iwamoto found a bound of

$$g_{an}^{PS} \lesssim 4 \times 10^{-10}, \tag{2.62}$$

where g_{an}^{PS} is the pseudoscalar axion-nucleon coupling constant. Iwamoto con-

19

verted this into the bounds

$$F_a \gtrsim 3 \times 10^8 \; GeV \qquad (2.63)$$

and

$$m_a \lesssim 0.02 \; eV, \qquad (2.64)$$

although this conversion is very dependent upon assumptions about neutron structure and cannot be considered reliable.

2.4.2.5 Supernovae

SN1987A in the Large Magellenic Cloud has aroused much interest in the particle physics community. Various novel particle phenomena might play a role in the extreme conditions present in a supernova. As the rest of this thesis is devoted to supernova bounds on axions, I shall only briefly cover these topics in this section.

The observations of SN1987A neutrinos were in general agreement with current theoretical models of supernovae in which the principle energy loss is via neutrino emission. Axion emission would compete with neutrino emission and, unless limited, could upset the agreement between theory and experiment.

The most important axion energy loss mechanism is nucleon-nucleon-axion bremsstrahlung, $NN \rightarrow NNa$. Various authors have derived limits on axion-nucleon coupling constants. The most comprehensive work comes from Mayle *et al* [20,21] and Burrows *et al* [32] who incorporated axion emission into numerical models of the newly born neutron star at the centre of SN1987A. The important restricting criterion is the duration of the neutrino pulse as detected (See Chapter 3). From these papers one can deduce that if $g_{ap} = g_{an} = g_a$ then

$$g_a \lesssim 5 \times 10^{-11}. \qquad (2.65)$$

In order to convert this into a bound on F_a one must consider the details of the quark structure of the nucleons and the details of particular axion models.

20

However, with reasonable confidence we can take the above limit to imply that,

$$F_a \gtrsim 10^9 \ GeV \qquad (2.66)$$

and

$$m_a \lesssim 0.005 \ eV. \qquad (2.67)$$

2.4.3 Cosmological Bounds

The original discussions of the cosmological constraints on axions have recently received severe qualifications[5]. In the framework of a broad class of inflationary scenarios, axions would probably dominate the mass density of the universe, but no rigorous bound on F_a can be derived. In the absence of inflation, or if the universe reheated beyond F_a after inflation, cosmic strings appear which efficiently radiate axions. The resulting mass density in axions is so large that it would be greater than the critical density of the universe unless

$$F_a \lesssim 10^{10} \ GeV \quad \text{and} \quad m_a \gtrsim 10^{-3} eV, \qquad (2.68)$$

according to Davies and Shellard[33] or,

$$F_a \lesssim 10^{12} \ GeV \quad \text{and} \quad m_a \gtrsim 10^{-5} eV, \qquad (2.69)$$

according to Harari and Sikivie[34]. No clear decision has been made, as yet, as to which of these bounds is correct.

3 Supernovae, SN1987A and Axion Bounds

3.1 Introduction

As we have already mentioned, one of the most spectacular events in modern astrophysics occurred on the 23rd of February 1987, when light and neutrinos from a supernova explosion in the Large Magellenic Cloud, which is a satellite of our Milky Way Galaxy, about 170,000 light years away, reached earth. The event, code-named SN1987A, the first visual supernova since Kepler observed one almost 400 years ago.

In this chapter I shall outline the current thinking on supernovae, explain the impact of the measurements from SN1987A and review the bounds on axion parameters that have been computed by considering axion emission from supernovae.

3.2 Stellar Evolution[9,35,36]

For almost the entire life of a star the heat generated by nuclear fusion creates a thermal pressure which counters the tendency of gravity to make the star collapse. In the first series of fusion reactions hydrogen is converted into helium, which is energetically favourable since the mass of the helium nucleus is slightly less than the combined masses of the four hydrogen atoms from which it forms. Our Sun is presently fuelled by hydrogen burning, as are all the other stars in the "main sequence". Hydrogen burning occurs mainly through the chain of reactions

$$p + p \rightarrow {}^{2}H + e^{+} + \nu_{e},$$
$$ {}^{2}H + p \rightarrow {}^{3}He + \gamma, \tag{3.1}$$
$$\text{and} \quad {}^{3}He + {}^{3}He \rightarrow \alpha + 2p.$$
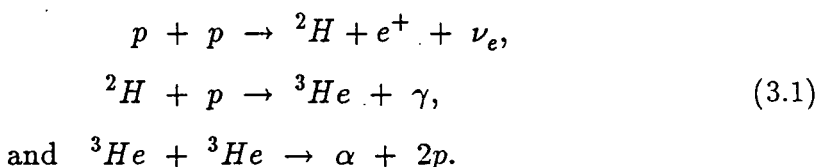
Hydrogen burning continues until all the hydrogen in the core of the star has been used up. The helium core then contracts under the influence of gravity whilst hydrogen burning continues in a shell around the core. Due to the contraction the core eventually becomes hot enough for the conversion of helium to carbon to occur,

$$ {}^{4}He + {}^{4}He \rightarrow {}^{8}Be,$$
$$ {}^{8}Be + {}^{4}He \rightarrow {}^{12}C + \gamma. \tag{3.2}$$
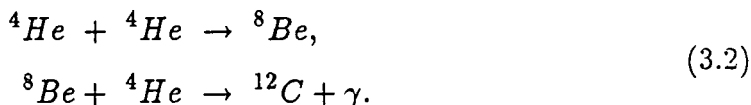
As successive fuels are exhausted further reactions may occur. The last cycle of
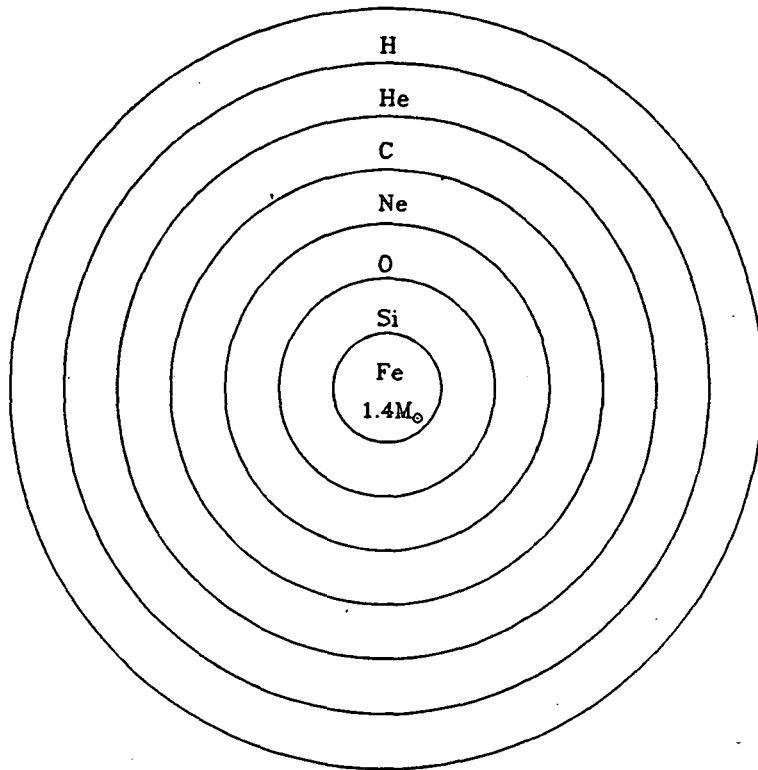
Figure 3.1 The Onion-like Structure of an Old Star (not to scale).

fusion combines silicon nuclei to form iron. This is the final stage since the ^{56}Fe nucleus is the most strongly bound of all nuclei and further fusion would absorb rather than release energy. The star will have an onion-like structure at this stage as shown in Figure 3.1. An iron core will be surrounded by a shell of silicon and beyond this are shells of oxygen, neon, carbon and helium. The outer envelope is mostly hydrogen.

Only the most massive stars, $M \gtrsim 8M_\odot$, proceed all the way to the iron core stage. A star of similar size to our Sun, $0.8M_\odot \lesssim M \lesssim 3M_\odot$, will get no further than helium burning. The smallest stars, $M \lesssim 0.8M_\odot$, will stop with hydrogen burning.

A larger star consumes its fuel much more quickly since the internal temperatures and pressures are higher. The calculated lifetime of the Sun in the main sequence, *i.e.* hydrogen burning, is about 10^{10} years, whereas a star of $M \sim 10M_\odot$ can reach the end of its life in the order of 10^7 years. No matter how long it takes, all the usable fuel in the core will eventually be exhausted.

When fusion ends in a small star, $M \lesssim 6$–$8M_\odot$, it becomes a white dwarf. A

white dwarf is supported against gravity by electron degeneracy pressure. Stars more massive than about 6–8$M_\odot$ end their life in an explosive Type II supernova.

3.3 Type II supernovae[5,9,35]

In the final day before a Type II supernova explodes, the fusion of silicon to form iron starts to occur at the centre of the star. Fusion continues at the edge of the iron core where silicon burns and adds more iron to the core increasing its size and mass. The core is an inert sphere under great external pressure, as there is no nuclear energy production inside the core.

The mass of the core is close to the Chandrasekhar mass limit which is the maximum mass a star can have while supported against gravity by electron degeneracy pressure. Numerically, $M_{Ch} = 5.8Y_e^2M_\odot \approx 1.4M_\odot$ where $Y_e \approx Z/A$ is the electron ratio per baryon. The central core temperature is $\simeq 0.7MeV$. The maximum density is around $10^{10}gcm^{-3}$ which is four orders of magnitude below that of nuclear matter. At this point, the core becomes unstable to two reactions, the photodissociation of iron, $\gamma + {}^{56}\text{Fe} \to 13\alpha + 4n$, and electron capture, $e^- + p \to n + \nu_e$. Iron photodissociation absorbs energy, and the neutrinos from electron capture escape the core, thus draining more energy. Further compression fails to increase the pressure enough to resist gravity which results in an increase in the rate of the above two reactions and a virtual free fall collapse.

During the collapse the core density and temperature increase. At a density of around 3×10^{11} $g\,cm^{-3}$, the mean free path of the neutrinos becomes smaller than the core radius and from then on the neutrinos are effectively trapped in the collapsing core. The infall is only stopped when the medium reaches nuclear densities and the equation of state stiffens. The sudden halt of the collapse leads to a "bounce" which forms an outgoing shock wave enclosing a mass of $\sim (0.8 - 0.9)M_\odot$, which is well inside the core. The shock wave moves outwards dissociating the nuclei it passes. When it reaches the neutrinosphere, the nuclear dissociation reduces the neutrino cross-section and leads to a sudden burst of neutrinos leaving the star. After about one second the shock reaches the edge of the iron core by which time a nascent neutron star has formed and about half of the neutron star binding energy, where $E_b \sim (2 - 3) \times 10^{53}ergs$, has been emitted. The shock is believed to lead eventually to the optical fireworks, although the exact mechanism

is still a matter of some contention. Further evolution of the star is essentially a cooling phenomenon.

3.4 Neutrino Observatories[35]

Various ongoing experiments can detect the neutrinos that come from stellar sources. The first of these was designed by Davis *et al* to measure the flux of neutrinos from the Sun. Davis *et al*'s detector consists of a large tank of CCl_4 which is buried deep beneath the earth's surface in a mine. Neutrinos are detected via the reaction

$$\nu_e + {}^{37}Cl \rightarrow {}^{37}Ar + e^-. \tag{3.3}$$

Since neutrinos are weakly interacting particles any experiment which is designed to detect them must be large and also deeply buried to reduce background interference.

Experiments such as that of Davis *et al*, which depend upon reactions like (3.3), can detect neutrino fluxes but not directions. Neutrino detectors which can distinguish direction do now exist. These detectors were not, however, originally designed to detect neutrinos but to try and discover proton decay

Grand unified theories (GUTs) predict that the proton will decay with a lifetime of $\sim 10^{30}$ years, much greater than the age of the universe $\sim 10^{10}$ years. Experiments designed to detect proton decay must therefore observe a large volume of matter. One type of detector that has been used consists of a few thousand tonnes of water surrounded by, or interspersed with, photomultiplier tubes. These are designed to detect the three cones of Čerenkov light emitted by the decay $p \rightarrow e^+\pi^0 \rightarrow e^+\gamma\gamma$, for example. The detectors must be situated deep underground in order to minimise fake events produced by cosmic rays.

The water, proton-decay detectors can also detect neutrinos via the Čerenkov light emitted by the electrons or positrons which are scattered or produced by neutrino interactions. The dominant detection process is

$$\overline{\nu}_e + p \rightarrow n + e^+, \tag{3.4}$$

which can only detect $\overline{\nu}_e$ and gives an approximately isotropic distribution of

Table 3.1 Characteristics of the Kamiokande II Detector.

Location	Kamioka (Japanese Alps)
Depth	1km
Detector fluid	H_2O
Mass	3000 tonnes
Electron Threshold	9 MeV
Number of electrons	2.27×10^{32}
Detectors	20in diameter PMT Čerenkov light

positrons. Some detections are via elastically scattered electrons,

$$\nu + e \rightarrow \nu + e, \tag{3.5}$$

which can occur for any ν species and is peaked in the forward direction. Čerenkov light detection provides information about the incident neutrino energy spectrum, and can be used to determine the direction from which the neutrino arrives and record the precise time of the event. These are all improvements over the radiochemical detectors such as that of Davis and collaborators.

Two particular detectors are worth mentioning at this point for reasons which will become apparent in the next section. These two are the American "IMB" [37] and the Japanese "Kamiokande II "[38] detectors. Table 3.1 describes some characterisics of the Kamiokande II detector. Note that not all of the 3000 tonnes of water are used for neutrino experiments due to the stringent background requirements.

The IMB detector is located in a salt mine near Fairport, Ohio, at a depth of 1570m of water equivalent. The detectors are 2048 8in. diameter photomultiplier tubes arranged on an approximately 1m grid. The timing, pulse height and geometry of photomultiplier hits are used to reconstruct the vertex, direction and energy of charged particle tracks.

The main differences between the two detectors are in the usable masses and in the thresholds for detecting neutrino events. The IMB detector has the larger

usable mass, which is 6.8 kilotonnes, however, the IMB detector is less sensitive to low-energy events because of the higher background rates and lower efficiency in Čerenkov light collection; the threshold is around $20MeV$.

3.5 SN1987A[5]

Supernova 1987A has been one of the most exciting scientific events of this century. It is almost 400 years since a supernova, visible to the unaided eye, has occurred. This one was not only detected in all parts of the electromagnetic spectrum, but also through neutrino emission. The neutrino detection marked the birth of extra-solar-system neutrino astronomy.

The star which exploded was the blue supergiant Sanduleuk-69202, estimated to be about 20 times heavier than the Sun. Massive stars ($\geq 10M_{\odot}$) have been generally assumed to be the progenitors of Type II supernovae, and SN1987A confirms this.

For over 20 years it has been known that the gravitational collapse events, believed to be associated with Type II supernovae and neutron star or black hole formation, are copious neutrino sources. In fact, the major form of energy transport in these objects comes from neutrino interactions. It has long been predicted that if an event occurred within the galaxy, the resulting neutrinos could be detected.

Tables 3.2 and 3.3 summarise the data obtained at the Kamiokande II [39] and IMB[40] detectors which is associated with the neutrino burst from SN1987A[5]. In each table the time is with respect to the first observed event, which for the IMB detector was at 7 : 35 : 41.374 (UT) and for the Kamiokande II detector was at 7 : 35 : 35 (UT) on the 23rd February 1987. The angles are the polar angles with respect to the direction away from the supernova. The energy is the measured energy of the electron or positron.

As mentioned in Section 3.2, about half of the neutrino binding energy is emitted within the first second after the core bounce. To simply assume that, for the next few seconds, neutrinos are emitted from a fixed neutrinosphere with a thermal spectrum is naive; however, such a cooling model is sufficiently detailed to allow for a comparison with the sparse data from the neutrino observations of SN1987A. Loredo and Lamb[41] performed the most detailed analysis along these

Table 3.2   SN1897A Neutrino Detections at the KII Detector.

Event	Time (sec)±60	Angle (deg)	Energy (MeV)
1	0.00	18±18	20.0±2.9
2	0.11	40±27	13.5±3.2
3	0.30	108±32	7.3±2.0
4	0.32	70±30	9.2±2.7
5	0.51	135±23	12.8±2.9
6	0.69	68±77	6.3±1.7
7	1.54	32±16	35.4±8.0
8	1.73	30±18	21.0±4.2
9	1.92	38±22	19.8±3.2
10	9.22	122±30	8.6±2.7
11	10.43	49±26	13.0±2.6
12	12.44	91±39	8.9±1.9

Table 3.3   SN1897A Neutrino Detections at the IMB Detector.

Event	Time (sec)±0.05	Angle (deg)	Energy (MeV)
1	0.00	80±10	38.0±7
2	0.41	44±15	37.0±7
3	0.65	56±20	28.0±6
4	1.14	65±20	39.0±7
5	1.56	33±15	36.0±9
6	2.68	52±10	36.0±6
7	5.01	42±20	19.0±5
8	5.58	104±20	22.0±5

Table 3.4   Loredo and Lamb's[41] Best Fit, and Inferred, Parameters.

m_{ν_e}	0 MeV
T_0	4.47 MeV
τ	4.15 sec
α	2.26
$t_{off}(K\mathrm{II})$	0 sec
$t_{off}(IMB)$	0 sec
E_b	2.86×10^{53} erg
R	22.6 km
$N_{det}(K\mathrm{II})$	12.5
$N_{det}(IMB)$	5.51

lines. They preferred an exponential cooling model with a constant neutrinosphere radius, R_{obs}, and a time varying temperature

$$T(t) = T_0 e^{-t/(4\tau)}, \tag{3.6}$$

where τ is the luminosity decay time scale. They used a parameter

$$\alpha \equiv \frac{R_{obs}}{10km}\frac{50kpc}{D}g^{\frac{1}{2}}, \tag{3.7}$$

where D is the distance to SN1987A and g is a weight factor which is unity if only left-handed neutrinos of any given flavour are being emitted (three flavours were assumed). They took the electron neutrino mass as a free parameter to allow for signal dispersion, and they introduced two separate offset times for the IMB and Kamiokande II detectors between the arrival of the first neutrinos and the first detected event. Thus they allowed the six parameters $T_0, \tau, \alpha, m_{\nu_e}, t_{off}(IMB)$ and $t_{off}(K\mathrm{II})$ to vary in order to achieve a maximum likelihood result.

Table 3.4 gives their best fit values along with the inferred neutron star radius, R, the total binding energy and the expected number of neutrino detections in each detector.

Loredo and Lamb's results confirm the standard picture of neutron star formation. In particular, the expected values for the neutrinosphere temperature, the cooling time scale and the total amount of energy which was radiated in neutrinos are confirmed. For the present purposes it is most important to note that the cooling time scale is not excessively shortened by novel effects. This result is insensitive to even extreme choices of an assumed neutrino mass. This means signal dispersion does not have a large effect.

3.6 SN1987A Axion Bounds

If axions exist, their emission from SN1987A would provide a cooling mechanism which is additional to the cooling by neutrino emission. The detected neutrino signal from SN1987A is in good agreement with supernova models which employ neutrino cooling exclusively. This means that any additional cooling due to axion emission must be restricted if the SN1987A neutrino signal is to remain in agreement with theoretical expectations.

Axion emission from a nascent neutron star can be divided into two qualitatively different regimes: "freely streaming" and "trapping". In the freely streaming regime the axion mean free path for absorption is large compared to the radius of the neutron star, and axions, once produced, "freely stream" into the vacuum of space. This implies a weak axion coupling. In the trapping regime, axions interacted sufficiently strongly that their mean free path for absorbtion is small compared to the radius of the neutron star; in this case they are said to be trapped and are effectively emitted from an axionsphere which parallels neutrino emission from a neutrinosphere.

In either regime, one expects that the axion luminosity, L_a, must be less than the neutrino luminosity, L_ν, if the cooling time for the nascent neutron star is not to be considerably shortened. Even smaller axion luminosities may also have a considerable effect so $L_a \lesssim L_\nu$ should give a conservative bound on the axion luminosity. During the exponential cooling phase $L_\nu \sim 3 \times 10^{53} erg\ sec^{-1}$. In order to obtain a bound on the axion coupling one must treat the free-streaming and trapped regimes differently.

3.6.1 Free-streaming Axions

If we assume that axions stream freely out of the core once they are produced then we only need to calculate the axion energy production rate in order to compute the axion luminosity. The dominant axion production process in the conditions relevant to the nascent neutron star is nucleon-nucleon-axion bremsstrahlung; $NN \rightarrow NNa$. The axion emission rate, which is identical to the axion production rate in the freely streaming regime, will be discussed in detail in Chapter 5.

Free streaming axion emission from hot neutron stars through nucleon-nucleon-axion bremsstrahlung was first calculated in the degenerate limit by Iwamoto[31]. In the nascent neutron star neither a degenerate or non-degenerate nucleon limit is appropriate. Brinkmann and Turner[42] have computed the axion production rate for intermediate conditions. Their results are given in Table 5.7, along with degenerate and non-degenerate nucleon approximations, and examined in Section 5.3.3.3. For the present purposes it is sufficient to note that some of their approximations are questionable and their treatment of $np \rightarrow npa$ is incorrect; however, their emission rate should still be of the right order of magnitude.

Two groups, Burrows et al[32], and Mayle et al[20,21], have incorporated free streaming axion emission rates into numerical simulations of nascent neutron star cooling. They can thus self-consistently calculate the expected SN1987A neutrino profile for given values of the axion-neutron and the axion-proton coupling and so determine the maximum coupling which would be consistent with the neutrino detections.

Mayle et al[21] used the non-degenerate approximation to the axion emission rates (see Section 5.3.3.1) and specifically used the DFS axion model. They quote conservative bounds of

$$F_a \gtrsim 1.7 \times 10^{10} GeV \qquad (3.8)$$

and

$$m_a \lesssim 3.6 \times 10^{-4} eV, \qquad (3.9)$$

when the naive quark naive quark model is used and

$$F_a \gtrsim 4.3 \times 10^9 GeV \qquad (3.10)$$

31

and

$$m_a \lesssim 1.4 \times 10^{-3} eV, \tag{3.11}$$

when the EMC model is used.

Burrows *et al*[32] used Brinkmann and Turner's[42] numerical values of the axion emission rate for arbitrary degeneracy. They employed a "generic axion model" with equal couplings to protons and neutrons. Using the naive quark model they found that for

$$F_a \gtrsim 6 \times 10^9 GeV, \tag{3.12}$$

i.e.

$$m_a \lesssim 10^{-3} eV, \tag{3.13}$$

the computed neutrino profiles were consistent with the neutrinos detected from SN1987A.

Raffelt[5] has attempted to combine these bounds by introducing numerical factors to account for various differences and omissions of each group's work. However, in order to account properly for the "back-reaction" of axion cooling on the numerical models, a co-operative study involving the numerical codes of both groups would be required. Burrows *et al*'s code tends, in general, to have lower core temperatures than that of Mayle *et al* which probably explains the difference between the bounds each group obtained.

In Chapter 5 I shall discuss some uncertainties in the axion emission rate and the approximate effect these may have on the above limits. The actual effect cannot be calculated without substituting the revised rates into the numerical simulations of Burrows *et al* and Mayle *et al*.

3.6.2 Axion Trapping

In the axion trapping regime the most important ingredient is the axion mean free path for absorbtion. This has been calculated, in the non-degenerate limit, by Burrows *et al*[43]. By incorporating this information into their nascent neutron star simulation code they find that cooling times will be unacceptably reduced

unless

$$F_a \lesssim 2 \times 10^7 GeV, \qquad (3.14)$$

i.e.

$$m_a \gtrsim 0.3eV. \qquad (3.15)$$

Values in this range are not quite excluded by alternative astrophysical bounds such as the red giant bounds of Section 2.3.3 for some variations of the hadronic axion model[5] of Section 2.4.2.2. I shall not consider this axion window any further. For details I refer the reader to Burrow's *et al*'s work[43], and also the review by Raffelt[5] which discusses this work and the axion window, Turner's window, which axion trapping calculations aim to explore.

4 Pion Production and the Nucleon-Nucleon Interaction
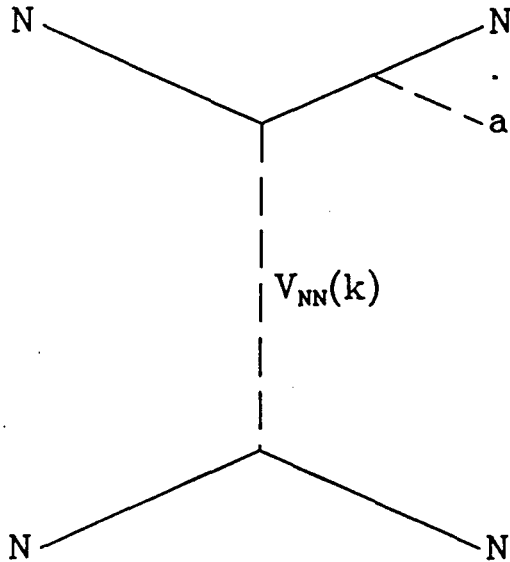
Figure 4.1   Born Approximation Diagram for Axion Production in Nucleon-Nucleon Scattering.

4.1 Introduction

The dominant axion production process in the interior of a nascent neutron star is nucleon-nucleon-axion bremsstrahlung. The simplest way to calculate a matrix element for this process is by assuming that the Born approximation is valid. In order to calculate the Born approximation matrix element for axion production in nucleon-nucleon scattering one includes diagrams of the form shown in Figure 4.1. In Figure 4.1 $V_{NN}(k)$ represents the nucleon-nucleon potential in momentum space. Naively, one might expect the dominant contribution to be that in which $V_{NN}(k)$ is represented purely by pion exchange. This is the approximation which has been used in the literature to derive bounds on the axion parameters from their production in supernovae.

A similar process to the above is that of pion production in proton-proton scattering which, at least as a first approximation, one might expect to be com-

momentum p and mass m_N a factor

$$P_N(p, m_N) = \frac{i(\not p + m_N)}{p^2 - m_N^2} \tag{4.1}$$

is required. Diagramatically this is represented by

$$\frac{i(\not p + m_N)}{p^2 + m_N^2}$$

iv) Vertex factors for nucleons and mesons will be treated in the following subsections.

b) *The Scalar Meson*

The nucleon-nucleon-meson interaction Lagrangian for a scalar meson, $\alpha^{(s)}$, is

$$\mathcal{L}_s = g_s \overline{\psi} \psi \alpha^{(s)}, \tag{4.2}$$

where ψ is a nucleon field. This interaction Lagrangian gives us the diagramatically represented Feynman rule,

i.e. a vertex factor of ig_s.

The propagator for a scalar meson with momentum p and mass m_s is given by

$$P_s(p, m_s) = \frac{i}{p^2 - m_s^2}. \tag{4.3}$$

Figure 4.3   An Example of a OBE Diagram for Nucleon-Nucleon Scattering.

A nucleon-nucleon potential model which can be applied, in an unambiguous way, to axion and pion production is that of Holinde[44]. In the simplest version of his work the inter-nucleon potential is represented by the exchange of various mesons. This is a direct extension of Yukawa's interaction which is based on the exchange of a pion. The Feynman diagrams required for this approach are of the form shown in Figure 4.3 in which α is a particular exchanged meson.

Once the masses and couplings of the mesons have been specified, the elastic scattering phase shifts can be determined[44,45]. The determination of the phase shifts is rather involved and will not be described here. Holinde[44] takes the exchanged mesons' coupling constants and masses as free parameters which are varied to obtain the best fit to the experimental phase shift data.

Holinde *et al*'s[44,46] recent work considers the inclusion of multiple meson exchanges in the inter-nucleon potential. For simplicity, I will only consider single meson exchange contributions, *i.e.* the one boson exchange model (OBE), for use in pion or axion production.

36

In this section I will give details of the mesons and their interactions with nucleons. The purpose of this is two-fold. Firstly, it will serve as a reference for Feynman rules used for pion and axion production. Secondly, the nucleon-nucleon interaction provides a straightforward example in which to introduce the conventions and certain calculational techniques.

4.2.1 Feynman Rules for Nucleons and Mesons

This section gives the Feynman rules for the multiplicative factors to be used in determining $-i\mathcal{M}$, where $\mathcal{M}$ is a matrix element, from Feynman diagrams involving nucleons and mesons.

a) *The Nucleon*

The nucleon is a spin $\frac{1}{2}$ fermion. There are two species of nucleon, the proton and the neutron, which together form an isospin $\frac{1}{2}$ doublet. The proton has $\mathcal{I}_3 = +\frac{1}{2}$ and the neutron has $\mathcal{I}_3 = -\frac{1}{2}$. Isospin for nucleon-nucleon interactions will be considered further in subsection (e). The required Feynman rules for nucleons are:

i) For an external, incoming nucleon with momentum p and spin s, a multiplicative factor of $u(p,s)$ is required. Diagramatically this is represented by
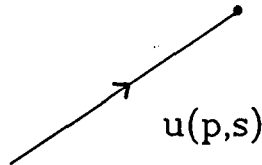
where $u(p,s)$ is a four component spinor.

ii) For an external, outgoing nucleon with momentum p and spin s, a multiplicative factor $\bar{u}(p,s)$ is required. Diagramatically this is represented by
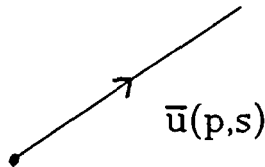
where $\bar{u}(p,s) = u^\dagger \gamma^0$ is a four component conjugate spinor.

iii) For a nucleon propagator (an internal line in a Feynman diagram) with

momentum p and mass m_N a factor

$$P_N(p, m_N) = \frac{i(\not{p} + m_N)}{p^2 - m_N^2}$$

(4.1)

is required. Diagramatically this is represented by

$$\frac{i(\not{p} + m_N)}{p^2 + m_N^2}$$

iv) Vertex factors for nucleons and mesons will be treated in the following subsections.

b) *The Scalar Meson*

The nucleon-nucleon-meson interaction Lagrangian for a scalar meson, $\alpha^{(s)}$, is

$$\mathcal{L}_s = g_s \overline{\psi} \psi \alpha^{(s)},$$

(4.2)

where ψ is a nucleon field. This interaction Lagrangian gives us the diagramatically represented Feynman rule,

i.e. a vertex factor of ig_s.

The propagator for a scalar meson with momentum p and mass m_s is given by

$$P_s(p, m_s) = \frac{i}{p^2 - m_s^2}.$$

(4.3)

38

Diagramatically the propagator is represented by

$$\circ\!\!-\ \text{--}\ \text{--}\ \text{--}\ \text{--}\ \text{--}\ \text{--}\!\!-\!\circ$$
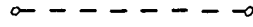
$$\frac{i}{p^2+m_s^2}.$$

An example of a scalar meson is the σ meson.

c) *The Pseudoscalar Meson*

For a pseudoscalar meson, $\alpha^{(ps)}$ *e.g.* π, there are two possible nucleon-nucleon-meson interaction Lagrangians:

i) the pseudoscalar coupling

$$\mathcal{L}_{ps} = ig_{ps}\overline{\psi}\gamma_5\psi\alpha^{(ps)}; \tag{4.4}$$

and,

ii) the pseudovector (or axial) coupling

$$\mathcal{L}_{pv} = \frac{f_{ps}}{m_{ps}}\overline{\psi}\gamma_5\gamma^{\mu}\partial_{\mu}\alpha^{(ps)}\psi. \tag{4.5}$$

This gives two possible vertex factors for the vertex
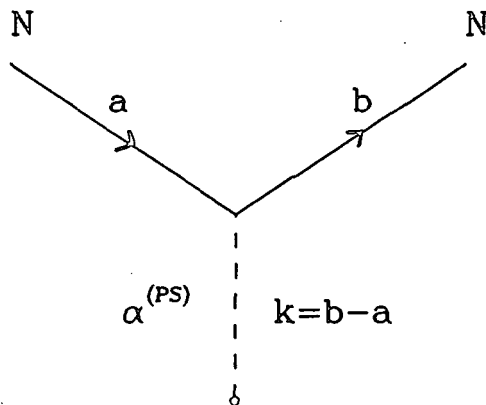
These are:

i) the pseudoscalar vertex factor $-g_{ps}\gamma_5$ and

ii) the pseudovector vertex factor $\frac{f_{ps}}{m_{ps}}\gamma_5\slashed{k}$.

Historically, the ps-coupling was preferred over the pv-coupling, since in conventional field theory, the latter is not renormalisable. However, for the description of low energy phenomena the pv-coupling is to be preferred, since it is directly related to the partially conserved axial current. Note that both couplings are identical if the the nucleons at the vertex are both on-shell-and $g_{ps} = 2m_N f_{ps}/m_{ps}$.

The propagator for a pseudoscalar meson of momentum p and mass $m_p s$ is the same as that for a scalar meson, i.e.

$$P_{ps}(p, m_{ps}) = \frac{i}{p^2 - m_{ps}^2}. \tag{4.6}$$

For an external, pseudoscalar meson line, which will be required for pion production, the multiplicative factor is 1.

d) *The Vector Meson*

The nucleon-nucleon-meson interaction Lagrangian for a vector meson, $\alpha^{(v)}$, is [44,45]

$$\mathcal{L}_v = g_v \overline{\psi} \gamma^\mu \psi \alpha_\mu^{(ps)} + \frac{f_v}{4m_N} \overline{\psi} \sigma^{\mu\nu} \psi f_{\mu\nu}^{(v)}, \tag{4.7}$$

where

$$\sigma^{\mu\nu} = \frac{i}{2}[\gamma^\mu, \gamma^\nu] \tag{4.8}$$

and

$$f_{\mu\nu}^{(v)} = \partial_\mu \alpha_\nu^{(v)} - \partial_\nu \alpha_\mu^{(v)}. \tag{4.9}$$

The first term of (4.7) is the vector part, and the second term is the tensor part of the interaction. This interaction term gives a vertex factor

$$i[g_v \gamma^\mu + \frac{f_v}{4m_N} i\sigma^{\mu\nu} k_\nu]$$

for a vertex,
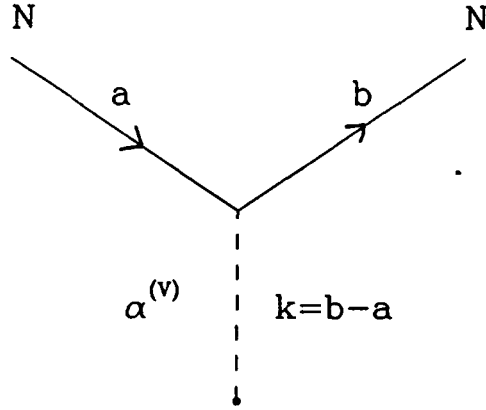
The propagator for a vector meson of momentum p and mass m_v is given by

$$P_{v\mu\nu}(p, m_v) = \frac{i(p_\mu p_\nu/m_v^2 - g_{\mu\nu})}{p^2 - m_v^2}. \tag{4.10}$$

e) *Isospin Considerations*

In any diagram for meson exchange it is necessary to take isospin into account. This can be done by adding isospin factors to the Feynman rules given above. Nucleons, as stated in subsection (a), are isospin-$\frac{1}{2}$ particles. The state of a nucleon is represented by an isospinor $\chi^{(I_3)}$ where

$$\chi_p \equiv \chi^{(I_3=1/2)} = \begin{pmatrix} 1 \\ 0 \end{pmatrix} \equiv \text{proton} \tag{4.11}$$

and

$$\chi_n \equiv \chi^{(I_3=-1/2)} = \begin{pmatrix} 0 \\ 1 \end{pmatrix} \equiv \text{neutron}. \tag{4.12}$$

Including isospin factors, one has, for an incoming or outgoing nucleon, the Feynman rule factor $N(p, m_N)$ or $\overline{N}(p, m_N)$ respectively, where

$$N(p, m_N) = \chi u(p, m_N) \tag{4.13}$$

and

$$\overline{N}(p, m_N) = \overline{u}(p, m_N)\chi^\dagger. \tag{4.14}$$

Exchanged mesons can be either isovector or isoscalar objects. Table 4.1 gives the isospin, spin and parity assignments for exchanged mesons included in Holinde's model.

Table 4.1   Spin, Isospin and Parity Assignments of Mesons

I $\backslash$ J^P	0^-	0^+	1^-
0	η	σ	ω, ϕ
1	π	δ	ρ

For isoscalar particles the vertex factors are multiplied by one and thus these particles only couple to nucleons with the same value of I_3. For isovector particles each vertex is multiplied by τ_i , where τ_i ($i = 1,2,3$) are the Pauli isopsin matrices;

$$ \tau_1 = \begin{pmatrix} 0 & 1 \\ 1 & 0 \end{pmatrix} \quad \tau_2 = \begin{pmatrix} 0 & -i \\ i & 0 \end{pmatrix} \quad \text{and } \tau_3 = \begin{pmatrix} 1 & 0 \\ 0 & -1 \end{pmatrix} . \tag{4.15} $$

Also, each propagator is multiplied by δ_{ij}, the isospin space metric. Thus, for example, the pion vertex factor would be $f_\pi \gamma_5 \not{k} \tau_i / m_\pi$, and the propagator would be $i\delta_{ij}/(p^2 - m_\pi^2)$. The combination of these factors in a matrix element will be discussed in Section 4.2.2.

f) Nucleon-Nucleon-Meson Form Factors

The Feynman rules discussed in the previous subsections are correct for point particles. However, it is well known that the nucleon and the exchange mesons are not pointlike, but are composite systems of finite size composed of quarks. In order to take the extended structure of hadrons into account phenomenologically, it is necessary to introduce a form factor, which is the momentum space Fourier transform of the matter distribution inside the hadron, at each vertex. Following Holinde[44], I will use a form factor

$$ F_\alpha(k^2) = \left(\frac{\Lambda_\alpha^2 - m_\alpha^2}{\Lambda_\alpha^2 - k^2} \right)^{n_\alpha}, \tag{4.16} $$

where

k is the meson four $-$ momentum,

Λ_α is the cut off mass,

$n_\alpha = 1$ for $\alpha = \pi, \eta, \sigma, \delta$,

and $n_\alpha = \dfrac{3}{2}$ for $\alpha = \rho, \omega, \phi$.
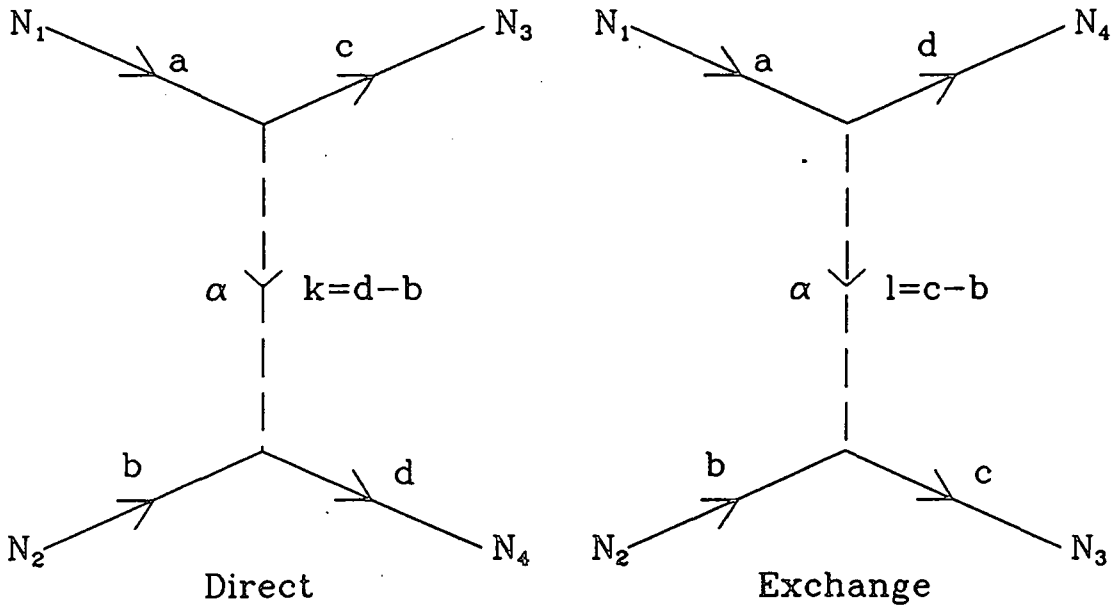
Figure 4.4 OBE Diagrams for NN Elastic Scattering.

Note that $F_\alpha(k^2 = m_\alpha^2) = 1$.

4.2.2 Born Approximation Matrix Elements for Nucleon-Nucleon Scattering

For each meson exchange there are two tree-level Feynman diagrams which contribute to the Born approximation of the nucleon-nucleon elastic scattering matrix element. These are shown in Figure 4.4.

In these diagrams the dashed propagator line represents any exchanged meson, α. The matrix element for nucleon-nucleon scattering in the Born approximation is of the generic form:

$$
\begin{aligned}
\mathcal{M}_{N_1 N_2 \to N_3 N_4} = i\big[& J_\alpha^{(\mu)}(a, s_a, c, s_c) P_{\alpha(\mu\nu)}(k, m_\alpha) J_\alpha^{(\nu)}(b, s_b, d, s_d) \\
& - J_\alpha^{(\mu)}(a, s_a, d, s_d) P_{\alpha(\mu\nu)}(l, m_\alpha) J_\alpha^{(\nu)}(b, s_b, c, s_c) \big],
\end{aligned}
\tag{4.17}
$$

where α represents the exchanged meson, μ and ν are vector indices which are only present when the exchanged meson is a vector particle (ρ, ω and ϕ), $P_\alpha(k, m_\alpha)$ represents the propagator of meson α with four-momentum k^μ and $j_\alpha(a, s_a, c, s_c)$ represents the nucleon current at the vertex at which the nucleons have momenta

43

a^μ and c^μ (incoming and outgoing respectively) and spins s_a and s_c. The minus sign in front of the second term in (4.17) is required because of the exchange of identical fermions, *i.e.* the nucleons. Isospin indices are suppressed in equation (4.17). Subsections (a) and (b) below will deal with specific examples of the Born approximation nucleon-nucleon scattering matrix.

a) Proton-Proton/Neutron-Neutron Matrix Elements

As isospin factors do not affect the matrix elements for proton-proton and neutron-neutron scattering I will deal with these matrix elements first. Subsection (b), below, will consider the differences made by isospin factors in the case of neutron-proton scattering. The matrix elements for proton-proton and neutron-neutron scattering are identical so the expressions given in this subsection apply equally to either case. In this and the following subsection I shall not explicitly include form factors; their inclusion in any expression is perfectly straightforward but notationally cumbersome.

The simplest example of a meson exchange matrix element is scalar meson exchange. In this case the vertex current is

$$J_s(a, s_a, c, s_c) = ig_s\overline{u}(c, s_c)u(a, s_a),\tag{4.18}$$

which, together with the scalar propagator, gives a matrix element

$$\begin{aligned}\mathcal{M}_{s(pp\to pp)} = i\Big[&-g_s^2\overline{u}(c, s_c)u(a, s_a)\frac{i}{k^2 - m_s^2}\overline{u}(d, s_d)u(b, s_b)\\&+ g_s^2\overline{u}(d, s_d)u(a, s_a)\frac{i}{l^2 - m_s^2}\overline{u}(c, s_c)u(b, s_b)\Big].\end{aligned}\tag{4.19}$$

The scalar mesons considered for OBE potentials are σ and δ.

The pseudoscalar current for the pseudoscalar meson is

$$J_{ps}(a, s_a, c, s_c) = -g_{ps}\overline{u}(c, s_c)\gamma_5 u(a, s_a),\tag{4.20}$$

while the pseudovector current is

$$J_{pv}(a, s_a, c, s_c) = \frac{f_{ps}}{m_{ps}}\overline{u}(c, s_c)\gamma_5(\not{c} - \not{a})u(a, s_a).\tag{4.21}$$

However, for on-shell nucleons, *i.e.* nucleons which satisfy the free particle Dirac

equation,

$$(\not{p} - m_N)u(p,s) = 0, \qquad (4.22)$$

the pseudovector current becomes

$$J_{pv}(a,s_a,c,s_c) = -\frac{2m_N f_{ps}}{m_{ps}}\overline{u}(c,s_c)\gamma_5 u(a,s_a). \qquad (4.23)$$

The pseudoscalar and pseudovector currents are identical for on-shell nucleons provided

$$g_{ps} = \frac{2m_N f_{ps}}{m_{ps}}. \qquad (4.24)$$

The matrix element for pseudoscalar exchange is given by

$$\begin{aligned}
\mathcal{M}_{ps(pp \to pp)} = i\Big[& g_{ps}^2 \overline{u}(c,s_c)\gamma_5 u(a,s_a)\frac{i}{k^2 - m_{ps}^2}\overline{u}(d,s_d)\gamma_5 u(b,s_b) \\
& - g_{ps}^2 \overline{u}(d,s_d)\gamma_5 u(a,s_a)\frac{i}{l^2 - m_{ps}^2}\overline{u}(c,s_c)\gamma_5 u(b,s_b)\Big].
\end{aligned} \qquad (4.25)$$

The pseudoscalar mesons considered for OBE models are π and η.

The vector meson current is

$$J_v^\mu(a,s_a,c,s_c) = i\overline{u}(c,s_c)[g_v\gamma^\mu + \frac{f_v}{2m_N}i\sigma^{\mu\nu}(c_\nu - a_\nu)]u(a,s_a). \qquad (4.26)$$

For on-shell nucleons, by using the Dirac equation, one can show that

$$J_v^\mu(a,s_a,c,s_c) = i\overline{u}(c,s_c)[(g_v + f_v)\gamma^\mu - \frac{f_v}{2m_N}(c^\mu - a^\mu)]u(a,s_a). \qquad (4.27)$$

Using the complete expression for the vector current (equation (4.26)) the matrix

element for vector exchange is given by

$$
\begin{aligned}
\mathcal{M}_{v(pp \to pp)} = \\
i\Bigg\{ \bigg[i\overline{u}(c,s_c)(g_v\gamma^\mu - \frac{f_v}{2m_N}i\sigma^{\mu\rho}k_\rho)u(a,s_a) \\
\times \frac{i(k_\mu k_\nu/m_v^2 - g_{\mu\nu})}{k^2 - m_{ps}^2} \\
\times \overline{u}(d,s_d)(g_v\gamma^\nu + \frac{f_v}{2m_N}i\sigma^{\nu\rho}k_\rho)u(b,s_b) \bigg] \\
- \bigg[i\overline{u}(d,s_d)(g_v\gamma^\mu - \frac{f_v}{2m_N}i\sigma^{\mu\rho}l_\rho)u(a,s_a) \\
\times \frac{i(l_\mu l_\nu/m_v^2 - g_{\mu\nu})}{l^2 - m_{ps}^2} \\
\times \overline{u}(c,s_c)(g_v\gamma^\nu + \frac{f_v}{2m_N}i\sigma^{\nu\rho}l_\rho)u(b,s_b) \bigg] \Bigg\}.
\end{aligned} \tag{4.28}
$$

Note however that the $k_\mu k_\nu/m_v^2$ term in the vector meson propagator has no effect. Due to the antisymmetry of $\sigma^{\mu\nu}$ this term does not contribute to the tensor part of the interaction. Also, if the two nucleons at a vertex are on-shell, which is obviously the case for nucleon-nucleon elastic scattering, the $k_\mu k_\nu/m_v^2$ term does not contribute to the vector part of the interaction either, since, for example,

$$
\begin{aligned}
J_v^\mu(a,s_a,c,s_c)k_\mu k_\nu &= i\overline{u}(c,s_c)(g_v - \frac{f_v}{2m_N}i\sigma^{\mu\rho}k_\rho)u(a,s_a)k_\mu k_\nu \\
&= i\overline{u}(c,s_c)(g_v \slashed{k}k_\nu - \frac{f_v}{2m_N}i\sigma^{\mu\rho}k_\rho k_\mu k_\nu)u(a,s_a) \\
&= i\overline{u}(c,s_c)g_v(\slashed{a} - \slashed{c})u(a,s_a) \\
&\equiv 0 \text{ from the Dirac equation.}
\end{aligned}
$$

Thus if the nucleon at, at least, one of the vertices of the propagator is on-shell the vector meson propagator becomes

$$
P_{v\mu\nu}(k,m_v) = \frac{-ig_{\mu\nu}}{k^2 - m_v^2}. \tag{4.29}
$$

The vector mesons considered are ρ, ω and ϕ.

b) Neutron-Proton Matrix Elements

Recall that each matrix element has two contributing diagrams, the direct and exchange diagrams (see Figure 4.4). For a particular meson exchange let us denote

the $pp \rightarrow pp$ matrix elements for the direct and exchange diagrams by $\mathcal{D}_\alpha$ and $\mathcal{E}_\alpha$ respectively, where α denotes the exchanged meson. Thus we have

$$\mathcal{M}_{\alpha(pp \rightarrow pp)} = \mathcal{D}_\alpha - \mathcal{E}_\alpha, \tag{4.30}$$

For pseudoscalar exchange, for example,

$$\mathcal{D}_{ps} = ig_{ps}^2 \bar{u}(c, s_c) \gamma_5 u(a, s_a) \frac{i}{k^2 - m_{ps}^2} \bar{u}(d, s_d) \gamma_5 u(b, s_b). \tag{4.31}$$

To compute np scattering matrix elements we must introduce the isospin factors, from subsection 4.2.1(e) , which will multiply $\mathcal{D}_\alpha$ and $\mathcal{E}_\alpha$. Let us take $N_1 = N_3 = n$ and $N_2 = N_4 = p$ (see Figure 4.4) as an illustration. For an isoscalar particle we have

$$\begin{aligned}
\mathcal{M}_{\alpha_{IS}(np \rightarrow np)} &= \chi^{\dagger(I_3=-\frac{1}{2})} \chi^{(I_3=-\frac{1}{2})} \chi^{\dagger(I_3=\frac{1}{2})} \chi^{(I_3=\frac{1}{2})} \mathcal{D}_\alpha \\
&\quad - \chi^{\dagger(I_3=\frac{1}{2})} \chi^{(I_3=-\frac{1}{2})} \chi^{\dagger(I_3=-\frac{1}{2})} \chi^{(I_3=\frac{1}{2})} \mathcal{E}_\alpha,
\end{aligned} \tag{4.32}$$

which gives

$$\mathcal{M}_{\alpha_{IS}(np \rightarrow np)} = \mathcal{D}_\alpha. \tag{4.33}$$

For an isovector particle we have

$$\begin{aligned}
\mathcal{M}_{\alpha_{IV}(np \rightarrow np)} &= \chi^{\dagger(I_3=-\frac{1}{2})} \tau_i \chi^{(I_3=-\frac{1}{2})} \delta^{ij} \chi^{\dagger(I_3=\frac{1}{2})} \tau_j \chi^{(I_3=\frac{1}{2})} \mathcal{D}_\alpha \\
&\quad - \chi^{\dagger(I_3=\frac{1}{2})} \tau_i \chi^{(I_3=-\frac{1}{2})} \delta^{ij} \chi^{\dagger(I_3=-\frac{1}{2})} \tau_j \chi^{(I_3=\frac{1}{2})} \mathcal{E}_\alpha
\end{aligned}, \tag{4.34}$$

which gives

$$\mathcal{M}_{\alpha_{IV}(np \rightarrow np)} = -\mathcal{D}_\alpha - 2\mathcal{E}_\alpha. \tag{4.35}$$

Taking the scalar mesons as an example we have

$$\mathcal{M}_{\sigma(pp \rightarrow pp)} = -ig_\sigma^2 \bar{u}(c, s_c) u(a, s_a) \frac{i}{k^2 - m_\sigma^2} \bar{u}(d, s_d) u(b, s_b) \tag{4.36}$$

and

$$\begin{aligned}
\mathcal{M}_{\delta(pp \rightarrow pp)} &= ig_\delta^2 \bar{u}(c, s_c) u(a, s_a) \frac{i}{k^2 - m_\delta^2} \bar{u}(d, s_d) u(b, s_b) \\
&\quad + 2ig_\delta^2 \bar{u}(d, s_d) u(a, s_a) \frac{i}{l^2 - m_\delta^2} \bar{u}(c, s_c) u(b, s_b).
\end{aligned} \tag{4.37}$$

Table 4.2   Exchanged Meson Coupling Constants and Masses

meson (α)	$g_\alpha^2/(4\pi)$ $(k^2 = m_\alpha^2)$	$g_\alpha^2/(4\pi)$ $(k^2 = 0)$	m_α (MeV)
π	14.4	14.17	138
η	6.0	4.56	548.5
ρ	0.77	0.37	712
	(6.6)	(6.6)	
ω	23	9.25	782.8
	(0.0)	(0.0)	
ϕ	5.0	0.85	1020
	(0.0)	(0.0)	
σ	8.2	6.22	550
δ	4.99	1.83	960

4.2.3 Exchanged Meson Coupling Constants and Masses

Table 4.2 gives the coupling constants and masses determined by Holinde[44] using a OBE model fit to the experimental nucleon-nucleon phase shifts. The cut-off mass used is the same for all the exchanged mesons,

$$\Lambda_\alpha = 1.53 \; GeV.$$

Holinde found that the inclusion of reasonable form factors at vertices was an important element of the model. In Table 4.2 the figures in brackets give the ratio of the tensor to vector coupling (f_v/g_v) for the vector mesons. The quality of the fit to the experimentally determined phase shifts is shown by the value for $\chi^2/\text{data} = 2.87$ [44].

4.3 π^0 Production in Proton-Proton Scattering

4.3.1 Pion Production Cross-section

The cross-section for the process $pp \to pp\pi^0$ is given by

$$\sigma_{pp \to pp\pi^0}(s) = \frac{1}{2F} \int \left(\frac{1}{4} \sum_{spins} |\mathcal{M}_{pp \to pp\pi^0}|^2\right) dQ_3, \tag{4.38}$$

where the factor $\frac{1}{2}$ takes account of the identical particles in the final state, the factor $\frac{1}{4}$ is included to average over initial particle spins, $F = 2s\sqrt{1 - 4m_N^2/s}$ is the 2-particle flux factor, $\mathcal{M}_{pp \to pp\pi^0}$ is the invariant amplitude for the process, the spin sum is over all combinations of proton spin projection values and dQ_3 is the Lorentz invariant 3-particle phase space.

Sections 4.3.1.1 and 4.3.1.2 will outline the Lorentz invariant phase space and the one boson exchange (OBE) approximation to the invariant amplitude. Section 4.3.1.3 discusses some details of the computational approach used in this work. The other sections, 4.3.1.4–6, discuss the results of numerical evaluations of $\sigma_{pp \to pp\pi^0}$ which use OBE approximations to the invariant amplitude.

4.3.1.1 Three Particle Phase Space

To compute the cross-section for $pp \to pp\pi^0$, one needs to integrate the spin-summed, squared matrix element, $\sum_{spins} |\mathcal{M}_{pp \to pp\pi^0}|^2$, over the Lorentz invariant phase space for the three final state particles. The details of the Born approximation amplitude will be given in the next section. In this section the treatment of the three particle phase space is explained.

Denoting the momenta of the two final state protons and the pion by $\vec{p}_c$, $\vec{p}_d$ and $\vec{p}_e$ respectively, three particle phase space is given by

$$dQ_3 = (2\pi)^4 \delta^4(P_I - c - d - e) \frac{d^3p_c}{(2\pi)^3 2E_c} \frac{d^3p_d}{(2\pi)^3 2E_d} \frac{d^3p_e}{(2\pi)^3 2E_e}, \tag{4.39}$$

where E_i represents the energy of particle i, P_I represents the sum of the four-momenta of the initial protons, and c, d and e represent the four-momenta of the two outgoing protons and the pion respectively.

A cross-section calculation is simplest in the centre of mass (c.o.m.) frame. The cross-section, phase space and matrix element are set up to be Lorentz invariant quantities. Rather than set up a special notation for the centre of mass frame I shall take all momenta and energies to represent c.o.m. quantities. In the c.o.m. frame one requires $(9-4) = 5$ independent variables in order to specify completely the four-momenta of the final state particles at a given c.o.m. energy. I will employ the following c.o.m. variables;

E_c — the energy of proton c,

E_d — the energy of proton d,

ϕ_c — the azimuthal angle of rotation of $\hat{p}_c$ about an incoming
proton direction, say $\hat{p}_a$

γ_c — the cosine of the angle between $\hat{p}_c$ and $\hat{p}_a$,

ϕ — the azimuthal angle of rotation of $\hat{p}_d$ about $\hat{p}_c$.

All that remains is to reduce the three particle phase space given in equation (4.39) to a form which contains just the above variables. Removing the delta function of three-momenta by integrating over d^3p_e one obtains

$$dQ_3 = \frac{1}{(2\pi)^5} \int d\Omega_c \int_0^{2\pi} d\phi \int \frac{p_c dp_c}{2E_c} \int \frac{p_d dp_d}{2E_d} \int_0^{\pi} \frac{sin\theta d\theta}{2E_e} \delta(\sqrt{s} - E_c - E_d - E_e),$$

(4.40)

where: Ω_c gives the orientation of $\hat{p}_c$ with respect to one of the incoming protons; θ and ϕ give the orientation $\hat{p}_d$ with respect to $\hat{p}_c$; $s = (c+d+e)^2$ is the Mandelstam s variable for the incoming protons, which equals the centre of mass energy; and

$$E_e = \sqrt{(\vec{p}_c + \vec{p}_d)^2 - m_e^2}$$
$$= (E_c^2 + E_d^2 + m_e^2 - m_c^2 - m_d^2 + 2p_c p_d \cos\theta)^{\frac{1}{2}}.$$

(4.41)

Now,

$$\delta(\sqrt{s} - E_c - E_d - E_e) = \left| \frac{\partial E_e}{\partial \cos\theta} \right|^{-1} \delta(\cos\theta - \alpha),$$

(4.42)

where α is given by,

$$(E_c^2 + E_d^2 + m_e^2 - m_c^2 - m_d^2 + 2p_c p_d \alpha)^{\frac{1}{2}} + E_c + E_d = \sqrt{s}.$$

(4.43)

50

So using,

$$p_c dp_c = E_c dE_c,$$

$$p_d dp_d = E_d dE_d$$

$$\text{and} \quad \frac{\partial E_e}{\partial \cos \theta} = \frac{p_c p_d}{E_e},$$

(4.44)

and performing the θ integration to remove the final state energy delta function given, the phase space integral becomes

$$dQ_3 = \frac{1}{256\pi^5} \int_0^{2\pi} d\phi_c \int_{-1}^1 d\gamma_c \int_0^{2\pi} d\phi \int dE_c \int dE_d. \quad (4.45)$$

In equation (4.45), the region of integration for E_c and E_d has been deliberately omitted. I shall specify this region by an argument taken from the Particle Data Group Tables[25].

In terms of invariant variables

$$E_c = \frac{[s + m_c^2 - s_{de}]}{2\sqrt{s}}, \quad (4.46)$$

and

$$E_d = \frac{[s + m_d^2 - s_{ce}]}{2\sqrt{s}}, \quad (4.47)$$

where

$$s_{ce} = (c + e)^2 = (P_I - d)^2 \quad (4.48)$$

and

$$s_{de} = (d + e)^2 = (P_I - c)^2. \quad (4.49)$$

Now

$$m_d^2 = [(d + e) - e]^2 = s_{de} + m_e^2 - 2e(d + e) \quad (4.50)$$

and

$$s = s_{de} + m_c^2 + 2c(d + e). \quad (4.51)$$

In the centre of mass frame of the particles with four-momenta d and e, (4.50)

51

and (4.51) become

$$m_d^2 = s_{de} + m_e^2 - 2E_e^* \sqrt{s_{de}} \qquad (4.52)$$

and

$$s = s_{de} + m_c^2 + 2E_c^* \sqrt{s_{de}} \qquad (4.53)$$

where E_c^* and E_e^* represent the energies of particles c and e in the centre of momentum frame of particles d and e. For a fixed value of s_{de} and s one can see from equations (4.52) and (4.53) that E_c^* and E_e^* are fixed. In this case the range of s_{ce} is determined by its values when $\hat{p}_c^*$ and $\hat{p}_e^*$ are parallel or anti-parallel, i.e.

$$s_{ce}^{\max} = (E_c^* + E_e^*)^2 - (p_c^* - p_e^*)^2 \qquad (4.54)$$

and

$$s_{ce}^{\min} = (E_c^* + E_e^*)^2 - (p_c^* + p_e^*)^2. \qquad (4.55)$$

This gives the range of E_d in the phase space integral, when E_c is fixed, as

$$E_d^{\min} = \frac{[s + m_c^2 - s_{ce}^{\max}]}{2\sqrt{s}} \qquad (4.56)$$

and

$$E_d^{\max} = \frac{[s + m_c^2 - s_{ce}^{\min}]}{2\sqrt{s}}. \qquad (4.57)$$

52

The full range for E_c, *i.e.* between the absolute minimum and maximum, is obvious,

$$E_c^{\text{min}} = m_c \tag{4.58}$$

and

$$E_c^{\text{max}} = \frac{[s + m_c^2 - (m_d + m_e)^2]}{2\sqrt{s}}, \tag{4.59}$$

since

$$s_{de}^{\text{min}} = (m_d + m_e)^2. \tag{4.60}$$

Thus the final version of the three particle phase space, with all the limits included, is,

$$dQ_3 = \frac{1}{256\pi^5} \int_{-1}^{1} d\gamma_c \int_{0}^{2\pi} d\phi_c \int_{0}^{2\pi} d\phi \int_{E_c^{\text{min}}}^{E_c^{\text{max}}} \int_{E_d^{\text{min}}(E_c)}^{E_d^{\text{max}}(E_c)} dE_d dE_c, \tag{4.61}$$

with $E_{c,d}^{\text{min,max}}$ as given in equations (4.58), (4.59), (4.56) and (4.57).

4.3.1.2 Born Approximation Matrix Elements

The second ingredient to computing the cross-section for the process $pp \to pp\pi^0$ is the invariant amplitude, or matrix element, for this process. For the purposes of this study I will employ a matrix element which is derived from one boson exchange diagrams. For any given meson exchange there are eight Feynman diagrams which contribute to the $pp \to pp\pi^0$ amplitude. These eight diagrams are shown in Figure 4.5.

In Figure 4.5:

a and b represent the incoming proton four$-$momenta,

c and d represent the outgoing proton four$-$momenta,

e represents the four$-$momentum of the produced pion,

α represents any exchanged meson,

and $\begin{pmatrix} k = d - b \\ k' = c - a \\ l = c - b \\ l' = d - a \end{pmatrix}$ represent the four$-$momenta of the exchanged meson.
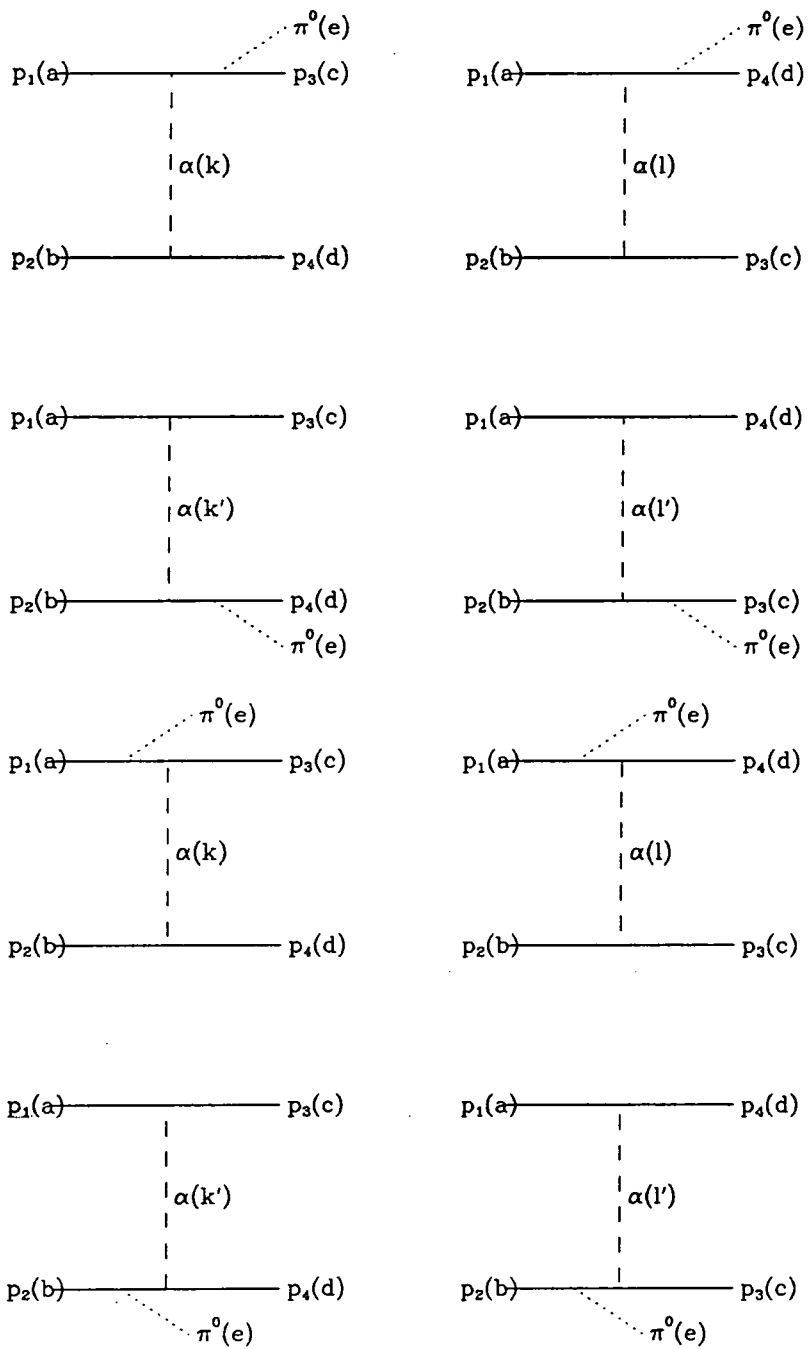
Figure 4.5   OBE Diagrams for Pion Production.

If a particular meson, α, is exchanged, the pion production matrix element is given by

$$
\mathcal{M}_{\alpha(pp \to pp\pi^0)}
$$

$$
= \sum_{s'_d} \overline{u}(d, s_d) \frac{f_\pi}{m_\pi} \gamma_5 (-\displaystyle{\not}q) \frac{iu(d', s'_d)}{d'^2 - m_N^2} \mathcal{M}_{\alpha(pp \to pp)}(a, b, c, d', s_a, s_b, s_c, s'_d)
$$

$$
+ \sum_{s'_c} \overline{u}(c, s_c) \frac{f_\pi}{m_\pi} \gamma_5 (-\displaystyle{\not}q) \frac{iu(c', s'_c)}{c'^2 - m_N^2} \mathcal{M}_{\alpha(pp \to pp)}(a, b, c', d, s_a, s_b, s'_c, s_d)
$$

$$
+ \sum_{s'_b} \mathcal{M}_{\alpha(pp \to pp)}(a, b', c, d, s_a, s'_b, s_c, s_d) \frac{i\overline{u}(b', s'_b)}{b'^2 - m_N^2} \frac{f_\pi}{m_\pi} \gamma_5 (-\displaystyle{\not}q) u(b, s_b)
$$

$$
+ \sum_{s'_a} \mathcal{M}_{\alpha(pp \to pp)}(a', b, c, d, s'_a, s_b, s_c, s_d) \frac{i\overline{u}(a', s'_a)}{a'^2 - m_N^2} \frac{f_\pi}{m_\pi} \gamma_5 (-\displaystyle{\not}q) u(a, s_a),
$$

(4.62)

where $\mathcal{M}_\alpha(a, b, c, d, d_a, s_b, s_c, s_d)$ represents the OBE matrix element for proton-proton scattering via the exchange of an α meson, as detailed in Section 4.2.2. Also, in equation (4.62), $a' = a - e$, $b' = b - e$, $c' = c + e$ and $d' = d + e$. For a concrete example, take σ exchange. In this case

$$
\mathcal{M}_{\sigma(pp \to pp)}(a, b, c, d, s_a, s_b, s_c, s_d) =
$$

$$
i\Big[-g_\sigma^2 \overline{u}(c, s_c) u(a, s_a) \frac{i}{(d - b)^2 - m_\sigma^2} \overline{u}(d, s_d) u(b, s_b)
$$

$$
+ g_\sigma^2 \overline{u}(d, s_d) u(a, s_a) \frac{i}{(c - b)^2 - m_\sigma^2} \overline{u}(c, s_c) u(b, s_b) \Big].
$$

(4.63)

The substitution of (4.63) into (4.62) will give the pion production matrix element for the exchange of a σ meson[†].

If several one boson exchanges are included the total matrix element will be the sum of the matrix elements derived from each meson exchange individually. Notationally,

$$
\mathcal{M}_{\pi\sigma\delta\cdots(pp \to pp\pi^0)}(a, b, c, d, e, s_a, s_b, s_c, s_d)
$$

$$
= \sum_{\alpha = \pi, \sigma, \delta, \ldots} \mathcal{M}_{\alpha(pp \to pp\pi^0)}(a, b, c, d, e, s_a, s_b, s_c, s_d).
$$

(4.64)

The formula for computing the cross-section for a 2-3 process, equation (4.38), contains the spin summed, squared matrix element, $\sum_{spins} |\mathcal{M}|^2$. In calculating

---

[†] To simplify the presentation of this expression, equation (4.63) does not explicitly include the necessary form factor. However, a form factor will be included for all numerical calculations of the $pp \to pp\pi^0$ cross-section (see Section 4.3.1.4).

cross-sections one normally derives an algebraic expression for $\sum_{spins} |\mathcal{M}|^2$, by using standard trace techniques [8]. However, because of the number of diagrams involved, any algebraic expressions for $\sum_{spins} |\mathcal{M}|^2$, would be complicated and lengthy. It is very difficult to check the validity of such an expression, and also, such lengthy algebraic expressions can become computationally inefficient. It is clearer and, for the more complicated matrix elements, quicker to compute the matrix element as a complex number for each spin combination and then to calculate $\sum_{spins} |\mathcal{M}|^2$ explicitly from these complex numbers. I have adopted this technique for $pp \rightarrow pp\pi^0$. The following section outlines the computational approach.

4.3.1.3 Computational Considerations

In Section 4.3.1.1. the three particle phase space, dQ_3, was reduced to a five dimensional integral over ϕ_c, γ_c, ϕ, E_c and E_d. In the centre of mass frame the matrix element becomes independent of ϕ_c. ϕ_c can be integrated over leaving a four dimensional integral at fixed s with

$$\int dQ_3 = \frac{1}{128\pi^4} \int_0^{2\pi} d\phi \int_{-1}^{1} d\gamma_c \int dE_c dE_d. \qquad (4.65)$$

The cross-section is thus given by,

$$\sigma_{pp \rightarrow pp\pi^0}(s) = \frac{1}{2^{10}\pi^4 F} \int \sum_{spins} |\mathcal{M}_{pp \rightarrow pp\pi^0}|^2 d\phi d\gamma_c dE_c dE_d. \qquad (4.66)$$

This four dimensional integral over the spin summed matrix element has been evaluated using an interpolating integration algorithm which uses selective subdivision, NAG Library[47] routine D01FCF. The results of this integration, for various OBE combinations are discussed in Section 4.3.1.4. In the following subsections (a) and (b) I shall detail the kinematical relationships and the method of matrix element evaluation which are needed to compute the cross-section.

a) Kinematics

Once the 5 four-vectors a, b, c, d and e have been specified all combinations of these can be evaluated directly. In this subsection I shall derive these four-vectors in the centre of mass frame in terms of s, γ_c, ϕ, E_c and E_d. I will choose

co-ordinates such that

> i) $\hat{z} = \hat{p}_a = -\hat{p}_b$,
>
> ii) $\hat{p}_c$ lies in the $x - z$ plane
>
> and iii) $\phi = 0$ when $\hat{z}$, $\hat{x}$ and $\hat{p}_d$ are co − planar.

Now,

$$s = (a + b)^2 = (E_a + E_b)^2, \tag{4.67}$$

and since $m_a = m_b = m_N$,

$$E_a = E_b = \frac{\sqrt{s}}{2} \quad \text{and} \quad p_a = p_b = \sqrt{E_a^2 - m_N^2}, \tag{4.68}$$

giving

$$a = (E_a,\ 0,\ 0,\ p_a) \tag{4.69}$$

and

$$b = (E_b,\ 0,\ 0,\ p_b), \tag{4.70}$$

c is simply given by

$$c = (E_c,\ p_c \sin\theta_c,\ 0,\ p_c \cos\theta_c), \tag{4.71}$$

where

$$p_c = \sqrt{E_c^2 - m_N^2} \quad \text{and} \quad \cos\theta_c = \gamma_c, \tag{4.72}$$

In order to find d, consider a second co-ordinate system $\hat{x}'$, $\hat{y}'$, $\hat{z}'$ such that

> i) $\hat{z}' = \hat{p}_c$,
>
> ii) $\hat{y}' = \hat{y}$
>
> and iii) $\hat{p}_a$ lies in the $x' - z'$ plane.

In this frame

$$\hat{p}'_d = (\sin\theta_{cd} \cos\phi,\ \sin\theta_{cd} \sin\phi,\ \cos\theta_{cd}),$$
$$\hat{x} = (\cos\theta_c,\ 0,\ \sin\theta_c),$$
$$\hat{y} = (0,\ 1,\ 0) \tag{4.73}$$
$$\text{and } \hat{z} = (-\sin\theta_c,\ 0,\ \cos\theta_c),$$

where θ_{cd} is the angle between $\hat{p}_c$ and $\hat{p}_d$.

Thus, in the unprimed frame

$$\hat{p}_d = (\hat{p}'_d\cdot\hat{x},\ \hat{p}'_d\cdot\hat{y},\ \hat{p}'_d\cdot\hat{y}), \qquad (4.74)$$

where

$$\hat{p}'_d\cdot\hat{x} = \cos\theta_c \sin\theta_{cd} \cos\phi + \sin\theta_c \cos\theta_{cd}$$

$$\hat{p}'_d\cdot\hat{y} = \sin\theta_{cd} \sin\phi,$$

and

$$\hat{p}'_d\cdot\hat{z} = -\sin\theta_c \sin\theta_{cd} \cos\phi + \cos\theta_c \cos\theta_{cd} \qquad (4.75)$$

and $\cos\theta_{cd}$ is given by the cosine rule, *i.e.*

$$\cos\theta_{cd} = \frac{(p_e^2 - p_c^2 - p_d^2)}{2p_c p_d}, \qquad (4.76)$$

where

$$p_d = \sqrt{E_d^2 - m_N^2}, \qquad (4.77)$$

$$p_e = \sqrt{E_e^2 - m_N^2}, \qquad (4.78)$$

and

$$E_e = 2E_a - E_c - E_d, \qquad (4.79)$$

from energy conservation. Thus, the 4-vector d is given by,

$$d = (E_d,\ \vec{p}'_d\cdot\hat{x},\ \vec{p}'_d\cdot\hat{y},\ \vec{p}'_d\cdot\hat{z}), \qquad (4.80)$$

and e can be found using four-momentum conservation, *i.e.*

$$e = a + b - c - d. \qquad (4.81)$$
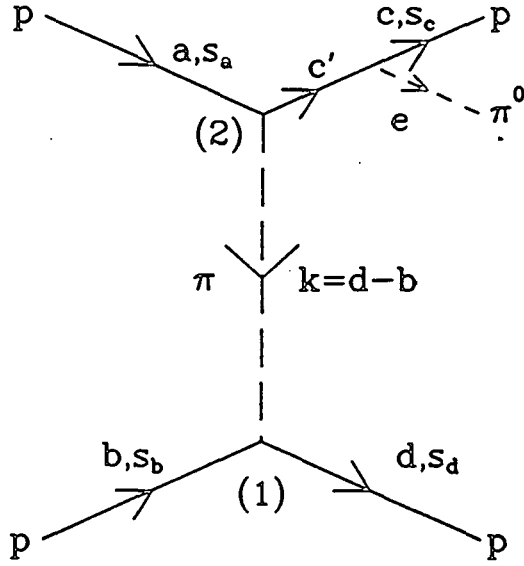
Figure 4.6 An Example of a OBE $pp \rightarrow pp\pi^0$ Diagram.

b) *Matrix Element Evaluation.*

The method used for calculating the matrix element for OBE $pp \rightarrow pp\pi^0$ diagrams can be seen most easily by studying one diagram in detail. For this example, the contributing diagram shown in Figure 4.6 will be considered.

Taking vertex (1) alone gives a current,

$$J_\pi(b, d, s_b, s_d) = \frac{f_\pi}{m_\pi} \overline{u}(d, s_d) A_\pi u(b, s_b), \tag{4.82}$$

where $A_\pi = \gamma_5 \not{k}$ represents the vertex matrix for a π-p-p vertex. In order to compute this current as a complex number for given spin projection combinations, ·it is necessary to use a particular representation for the spinors and Dirac gamma matrices. The spinors can be taken as[8]

$$u(a, s_a) = \sqrt{E_a + m_N} \begin{pmatrix} \chi^{(s_a)} \\ \frac{\vec{\sigma} \cdot \vec{p}}{E_a + m_N} \chi^{(s_a)} \end{pmatrix}, \tag{4.83}$$

where $\chi^{(1/2)} = \begin{pmatrix} 1 \\ 0 \end{pmatrix}$, $\chi^{(-1/2)} = \begin{pmatrix} 0 \\ 1 \end{pmatrix}$ and $\overline{u} \equiv u^\dagger \gamma^0$.

For the gamma matrices one can use the Dirac-Pauli representation in which

$$\gamma^0 = \begin{pmatrix} I & 0 \\ 0 & -I \end{pmatrix}, \tag{4.84}$$

$$\gamma^i = \begin{pmatrix} 0 & \sigma^i \\ -\sigma^i & 0 \end{pmatrix}, \tag{4.85}$$

and

$$\gamma^5 = \begin{pmatrix} 0 & I \\ I & 0 \end{pmatrix}, \tag{4.86}$$

where

$$I = \begin{pmatrix} 1 & 0 \\ 0 & 1 \end{pmatrix}, \tag{4.87}$$

and

$$\sigma^1 = \begin{pmatrix} 0 & 1 \\ 1 & 0 \end{pmatrix}, \quad \sigma^2 = \begin{pmatrix} 0 & -i \\ i & 0 \end{pmatrix} \text{ and } \sigma^3 = \begin{pmatrix} 1 & 0 \\ 0 & -1 \end{pmatrix}, \tag{4.88}$$

are the Pauli spin matrices.

From the above equations one can see that

$$\gamma_5 \not{k} = \begin{pmatrix} \vec{\sigma} \cdot \vec{p}_k & -E_k \\ E_k & -\vec{\sigma} \cdot \vec{p}_k \end{pmatrix}. \tag{4.89}$$

Using (4.83) and (4.89) in (4.82) one can compute J_π for each spin projection combination, of which there are four, by matrix multiplication.

The same technique can, of course, be used for vertex (2) of Figure 4.6 to obtain the current

$$J_{\pi\pi}(a, c, e, s_a, s_c) = \overline{u}(c, s_c) \frac{f_\pi}{m_\pi} \gamma_5(-\not{c}) \frac{i(\not{c}' + m_N)}{c'^2 - m_N^2} \frac{f_\pi}{m_\pi} (-\not{k}) u(a, s_a), \tag{4.90}$$

where

$$\not{c}' + m_N = \begin{pmatrix} E'_c + m_N & \vec{\sigma} \cdot \vec{p}_c{}' \\ \vec{\sigma} \cdot \vec{p}_c{}' & m_N - E'_c \end{pmatrix}. \tag{4.91}$$

Combining J_π and $J_{\pi\pi}$ with the pion propagator, $i.e.$

$$P_\pi(k, m_\pi) = \frac{i}{k^2 - m_\pi^2}, \tag{4.92}$$

gives the complex value of the matrix element for any spin projection for the

diagram shown in Figure 4.6,

$$
\begin{aligned}
&\mathcal{M}^{(1 \text{ diag.})}_{\pi(pp \to pp\pi^0)}(a,b,c,d,e,s_a,s_b,s_c,s_d) \\
&= iJ_\pi(b,d,s_b,s_d)\frac{i}{k^2 - m_\pi^2}J_{\pi\pi}(a,c,e,s_a,s_c)
\end{aligned}
\tag{4.93}
$$

To calculate the full matrix element, for a given spin projection combination, one adds the complex numbers related to all the diagrams to be included. $|\mathcal{M}_{pp \to pp\pi^0}|^2$ can then be calculated by taking the modulus squared of the matrix element for each spin projection combination and explicitly summing over these spin combinations.

The following vertex matrices are required to enable one to compute the contribution for any boson exchange. In these equations a represents any four-vector $(E_a, \vec{p}_a)$:

$$
\begin{aligned}
&\text{i) } \not{a} = \begin{pmatrix} E_a & -\vec{\sigma}\cdot\vec{p}_a \\ \vec{\sigma}\cdot\vec{p}_a & -E_a \end{pmatrix}, \\[2mm]
&\text{ii) } \gamma_5\not{a} = \begin{pmatrix} \vec{\sigma}\cdot\vec{p}_a & -E_a \\ E_a & -\vec{\sigma}\cdot\vec{p}_a \end{pmatrix}, \\[2mm]
&\text{iii) } \gamma^0 = \begin{pmatrix} I & 0 \\ 0 & -I \end{pmatrix}, \\[2mm]
&\text{iv) } \gamma^i = \begin{pmatrix} 0 & \sigma^i \\ -\sigma^i & 0 \end{pmatrix}, \\[2mm]
&\text{v) } \sigma^{0\nu}a_\nu = \begin{pmatrix} 0 & -i\vec{\sigma}\cdot\vec{p}_a \\ -i\vec{\sigma}\cdot\vec{p}_a & 0 \end{pmatrix} \\[2mm]
&\text{and} \quad \text{vi) } \sigma^{i\nu}a_\nu = \begin{pmatrix} \epsilon_{ijk}\sigma_j p_{ak} & -iE_a\sigma_i \\ -iE_a\sigma_i & \epsilon_{ijk}\sigma_j p_{ak} \end{pmatrix}.
\end{aligned}
\tag{4.94}
$$

The vertex matrices for the various boson exchanges were given in Section 4.2.1.

4.3.1.4 Cross-section Computations

In order to study the effect of including other particle exchanges, in addition to one pion exchange, various combinations of exchanges have been used to calculate

the $pp \rightarrow pp\pi^0$ cross-section as a function of laboratory energy,

$$T_{lab} = \frac{s}{2m_N} - 2m_N$$

These cross-sections have been computed over an energy range $0.3 \leq T_{lab} \leq 1.0$ GeV. The threshold for the process is at 0.286 GeV

To simplify the description of the result I shall denote the exchanges included as subscripts on the cross-section, σ. So, for example, $\sigma_{\pi\sigma\omega}$ will refer to the cross-section computed by including π, σ and ω exchanges in the matrix element. All the results quoted have been computed to within a numerical accuracy of 1%, and include the form factors described in Section 4.2.1.

a) *Single Boson Exchanges*

In this subsection each exchanged boson has been considered individually, *i.e.* just the diagrams containing the chosen boson have been included in the matrix element computation. The cross-section relating to each of the seven possible exchanged bosons has been computed. The results for each boson exchange are given in Table 4.3. Figure 4.7 shows plots of σ_π, σ_σ, σ_ω and σ_ρ. Also shown in Figure 4.7 are the experimental points with error bars[48,49] and an analytical least squares fit to these points [50]. In the figure the analytical fit is the solid line. It is given by the following set of equations;

$$\sigma = \frac{\pi}{2p_a^2}\kappa(p_r/p_0)^\lambda \frac{m_0^2\Gamma^2(q/q_0)^3}{(\langle M\rangle^2 - m_0^2)^2 + m_0^2\Gamma^2}, \qquad (4.95)$$

where

$$p_r^2(s) = \frac{[s - (m_N - \langle M\rangle)^2][s - (m_N + \langle M\rangle)^2]}{4s},$$

$$q^2(\langle M\rangle^2) = \frac{[\langle M\rangle^2 - (m_N - m_\pi)^2][\langle M\rangle^2 - (m_N + m_\pi)^2]}{4\langle M\rangle^2}$$

$$q_0^2 = q^2(m_0^2),$$

$$p_0^2 = (m_N + m_0)^2/4 - m_N^2,$$

$$\langle M\rangle = M_0 + (\tan^{-1} Z_+ - \tan^{-1} Z_-)^{-1}\frac{\Gamma_0}{4}\ln\frac{1 + Z_+^2}{1 + Z_-^2},$$

$$Z_+ = 2(\sqrt{s} - m_N - M_0)/\Gamma_0, \quad Z_- = 2(m_N + m_\pi - M_0)/\Gamma_0,$$

$$\kappa = 3.772, \quad \lambda = 1.262,$$

$$M_0 = 1.22 GeV, \quad m_0 = 1.188 GeV,$$

$$\Gamma_0 = 0.12 GeV, \quad \Gamma = 0.099 GeV.$$

π-exchange underestimates the $pp \to pp\pi^0$ cross-section over the whole of the energy range considered, but σ_π is always within a factor of 3 of the analytical fit to the data, as was determined by Turner et al [51]. (See Section 4.3.3.2)

σ_δ, σ_ϕ and σ_η are all much smaller than σ_π over the whole of the energy range I considered The values are so small that one might expect that the contribution of δ, ϕ and η exchange to be negligible. Following this line of argument, one could omit δ, ϕ and η exchange from a more detailed calculation of the $pp \to pp\pi^0$ cross-section. However, one is not justified in doing this as we shall see in subsection (b).

σ_ρ is consistently smaller than σ_π by about a factor of 2. From this information alone, one would expect ρ-exchange to give a significant contribution to the matrix element for $pp \to pp\pi^0$.

The results for ω and σ exchange are a little surprising if one expects π exchange to be dominant. For $T_{lab} \lesssim 0.93 GeV$, $\sigma_\sigma > \sigma_\pi$ and for $T_{lab} \lesssim 0.59 GeV$, $\sigma_\omega > \sigma_\pi$. $\sigma_\sigma > \sigma_\omega$ for the whole of the energy range considered. At $T_{lab} = 0.3 GeV$

$$\frac{\sigma_\sigma}{\sigma_\pi} = 16.7 \text{ and } \frac{\sigma_\omega}{\sigma_\pi} = 7.9,$$

which are rather large factors. This does not seem to be consistent with the view that one π-exchange is the dominant contribution to pion production.

The individual single meson exchange cross-sections can only give a rough guide to the importance of the various exchanges as they do not take into account any interference which may occur between the OBE diagrams. Some combinations of exchanged meson diagrams will be considered next.

Table 4.3 Single Boson Exchange Cross-sections

T_{lab} (Gev)	σ_π (μb)	σ_σ (μb)	σ_ω (μb)	σ_ρ (μb)	σ_δ (μb)	σ_ϕ (μb)	σ_η (μb)
0.30	0.332	5.51	2.62	0.136	0.0831	0.00914	0.00459
0.31	1.13	15.7	7.54	0.433	0.242	0.0265	0.0168
0.32	2.61	30.6	14.8	0.945	0.478	0.0524	0.0413
0.33	4.99	49.6	24.2	1.72	0.788	0.0862	0.0830
0.34	8.46	72.3	35.5	2.81	1.17	0.128	0.148
0.35	13.2	98.5	48.8	4.27	1.61	0.176	0.240
0.36	19.4	128.	63.7	6.12	2.12	0.231	0.366
0.37	27.3	160.	80.2	8.52	2.69	0.293	0.531
0.38	36.9	194.	98.2	11.4	3.32	0.361	0.740
0.39	48.3	231.	118.	14.9	3.99	0.434	0.998
0.40	61.7	269.	138.	19.0	4.72	0.513	1.31
0.42	94.6	352.	183.	29.2	6.33	0.685	2.11
0.44	136.	441.	233.	42.4	8.10	0.880	3.16
0.46	186.	534.	287.	58.8	10.0	1.09	4.49
0.48	244.	632.	345.	78.6	12.1	1.32	6.11
0.50	311.	735.	405.	102.	14.3	1.57	8.04
0.55	511.	999.	570.	176.	20.3	2.24	14.2
0.60	756.	1270.	751.	273.	26.8	2.99	22.3
0.65	1040.	1540.	945.	392.	33.6	3.80	32.1
0.70	1350.	1820.	1150.	534.	40.7	4.69	43.6
0.80	2030.	2360.	1590.	876.	55.3	6.58	70.9
0.90	2770.	2870.	2050.	1290.	70.0	8.62	102.
1.00	3540.	3350.	2520.	1770.	84.7	10.7	136.
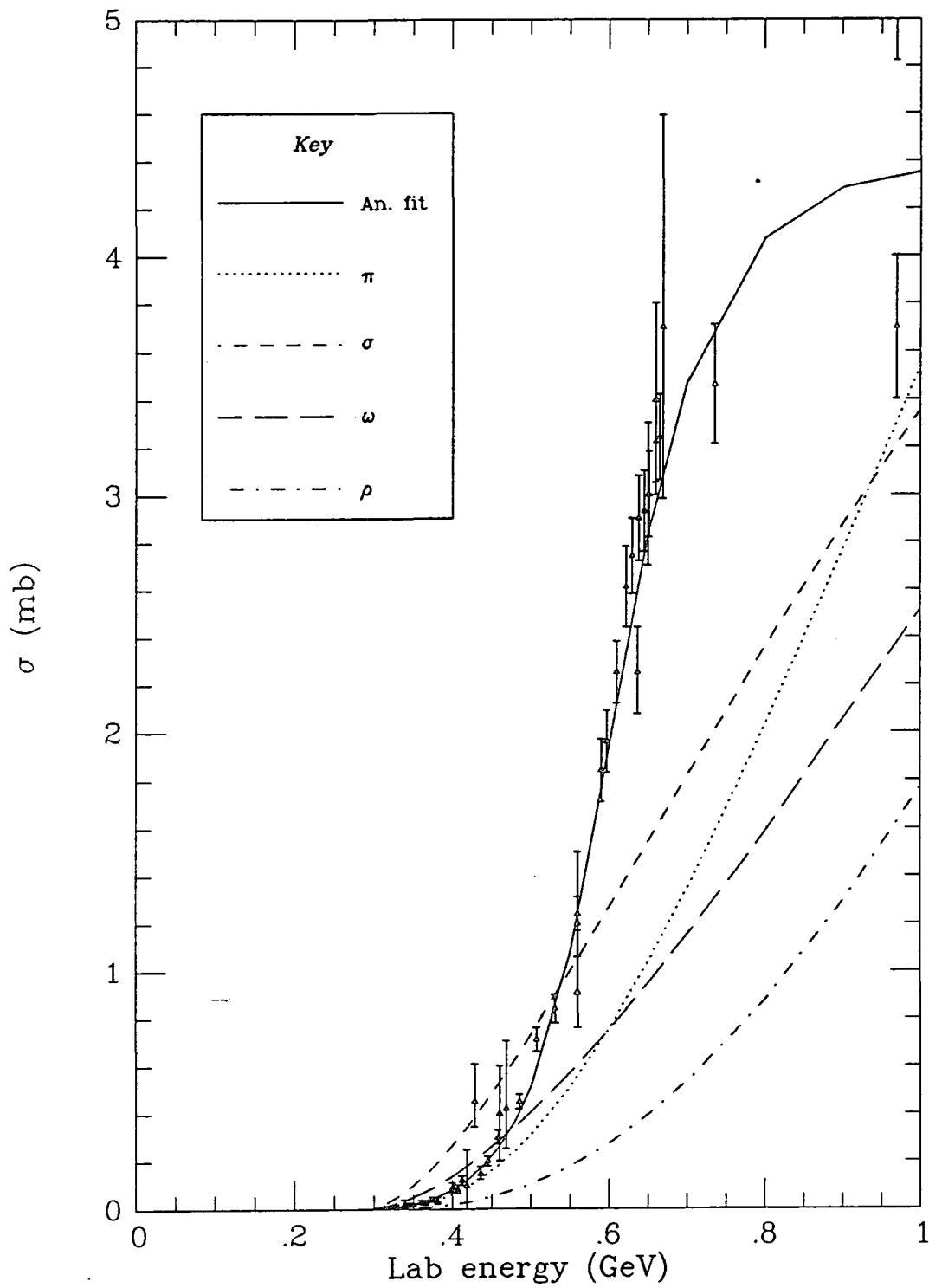
Figure 4.7 The Single Boson Exchange Cross-sections for $pp \rightarrow pp\pi^0$ with various exchanges.

b) *Combinations of meson exchanges*

One could just include all the possible meson exchanges and work out the corresponding $pp \rightarrow pp\pi^0$ cross-section. However, this would not give any information about the importance of each meson exchange. The results of the previous subsection suggest that δ, ϕ and η exchanges should be less important than π, ρ, σ and ω exchanges. The single meson exchanges of the previous subsection cannot tell us anything about the possible interference among the meson exchange contributions to the matrix element. In order to gain some insight into the effect of such interference I shall start with the OPE matrix element and add the other mesons individually. The first addition will be the σ meson, which gives the largest single meson exchange cross-section at $T_{lab} = 0.3 GeV$, and the last will be the η meson which gives the smallest. The full order will be σ, ω, ρ, δ, ϕ then η. The resulting cross-sections are given in Table 4.4.. Figure 4.8 shows σ_π, $\sigma_{\pi\sigma}$ and $\sigma_{\pi\sigma\omega}$, Figure 4.9 shows σ_π, $\sigma_{\pi\sigma\omega\rho}$ and $\sigma_{\pi\sigma\omega\rho\delta}$, and Figure 4.10 shows σ_π, $\sigma_{\pi\sigma\omega\rho\delta\phi}$ and $\sigma_{\pi\sigma\omega\rho\delta\phi\eta}$.

The first two additions are very interesting since they show that there is a strong cancellation between σ and ω-exchange contributions. $\sigma_{\pi\sigma}/\sigma_\pi \simeq 10$ at $T_{lab} = 0.3 GeV$ showing the dominant σ-exchange contribution which was foreseen in the previous subsection. However, $\sigma_{\pi\sigma\omega}/\sigma_\pi \simeq 0.26$ and $\sigma_{\pi\sigma\omega}/\sigma_{\pi\sigma} \simeq 0.03$. So although σ_σ and σ_ω are significantly greater than σ_π at $T_{lab} = 0.3 GeV$, $\sigma_{\pi\sigma\omega}$ is less than σ_π. This is indicative of the strong cancellation. One may have expected this since the σ-exchange and ω-exchange contributions to the co-ordinate space internucleon potential are of opposite signs[44]. At $T_{lab} = 1 GeV$ the effect of σ and ω addition is not so dramatic. Also, the addition of all other particles in turn does not give any dramatic indication of cancellation.

$\sigma_T \equiv \sigma_{\pi\sigma\omega\rho\delta\phi\eta}$, the cross-section which includes all the exchanged mesons, should be the best approximation to $\sigma_{pp \rightarrow pp\pi^0}$ that can be obtained using OBE amplitudes. This being the case, it is interesting to assess the other combinations, $\sigma_{comb} \equiv \sigma_\pi, \sigma_{\pi\sigma} \ldots etc.$, as approximations to σ_T. One can define a relative error magnitude as

$$\epsilon = \frac{|\sigma_T - \sigma_{comb}|}{\sigma_{comb}}. \tag{4.96}$$

Table 4.5 gives this relative error as a function of laboratory energy for each meson exchange combination. Figure 4.11 gives a graphical display of these errors.

Table 4.4 Combined Boson Exchange Cross-Sections

T_{lab} (Gev)	σ_π (μb)	$\sigma_{\pi\sigma}$ (μb)	$\sigma_{\pi\sigma\omega}$ (μb)	$\sigma_{\pi\sigma\omega\rho}$ (μb)	$\sigma_{\pi\sigma\omega\rho\delta}$ (μb)	$\sigma_{\pi\sigma\omega\rho\delta\phi}$ (μb)	$\sigma_{\pi\sigma\omega\rho\delta\phi\eta}$ (μb)
0.30	0.332	3.32	0.0852	0.0602	0.0407	0.0296	0.0389
0.31	1.13	9.28	0.356	0.294	0.173	0.164	0.226
0.32	2.61	17.9	0.966	0.846	0.486	0.512	0.709
0.33	4.99	29.0	2.08	1.86	1.08	1.20	1.65
0.34	8.46	42.4	3.87	3.50	2.08	2.34	3.22
0.35	13.2	57.7	6.49	5.89	3.59	4.09	5.58
0.36	19.4	75.4	10.1	9.17	5.72	6.55	8.88
0.37	27.3	95.0	14.9	13.5	8.60	9.83	13.3
0.38	36.9	117.	20.9	18.9	12.3	14.0	18.9
0.39	48.3	140.	28.2	25.6	16.9	19.4	25.9
0.40	61.7	165.	37.0	33.6	22.6	25.8	34.4
0.42	94.6	222.	59.2	54.1	37.3	42.4	56.2
0.44	136.	285.	88.0	80.9	57.1	64.6	85.0
0.46	186.	355.	124.	115.	82.4	93.0	122.
0.48	244.	432.	166.	155.	114.	128.	166.
0.50	311.	515.	216.	204.	151.	170.	221.
0.55	511.	746.	369.	359.	275.	307.	392.
0.60	756.	1010.	563.	566.	442.	491.	623.
0.65	1040.	1300.	794.	824.	657.	727.	914.
0.70	1350.	1610.	1060.	1140.	919.	1010.	1270.
0.80	2030.	2270.	1670.	1890.	1580.	1730.	2140.
0.90	2770.	2970.	2380.	2860.	2410.	2630.	3210.
1.00	3540.	3680.	3150.	3960.	3420.	3710.	4500.
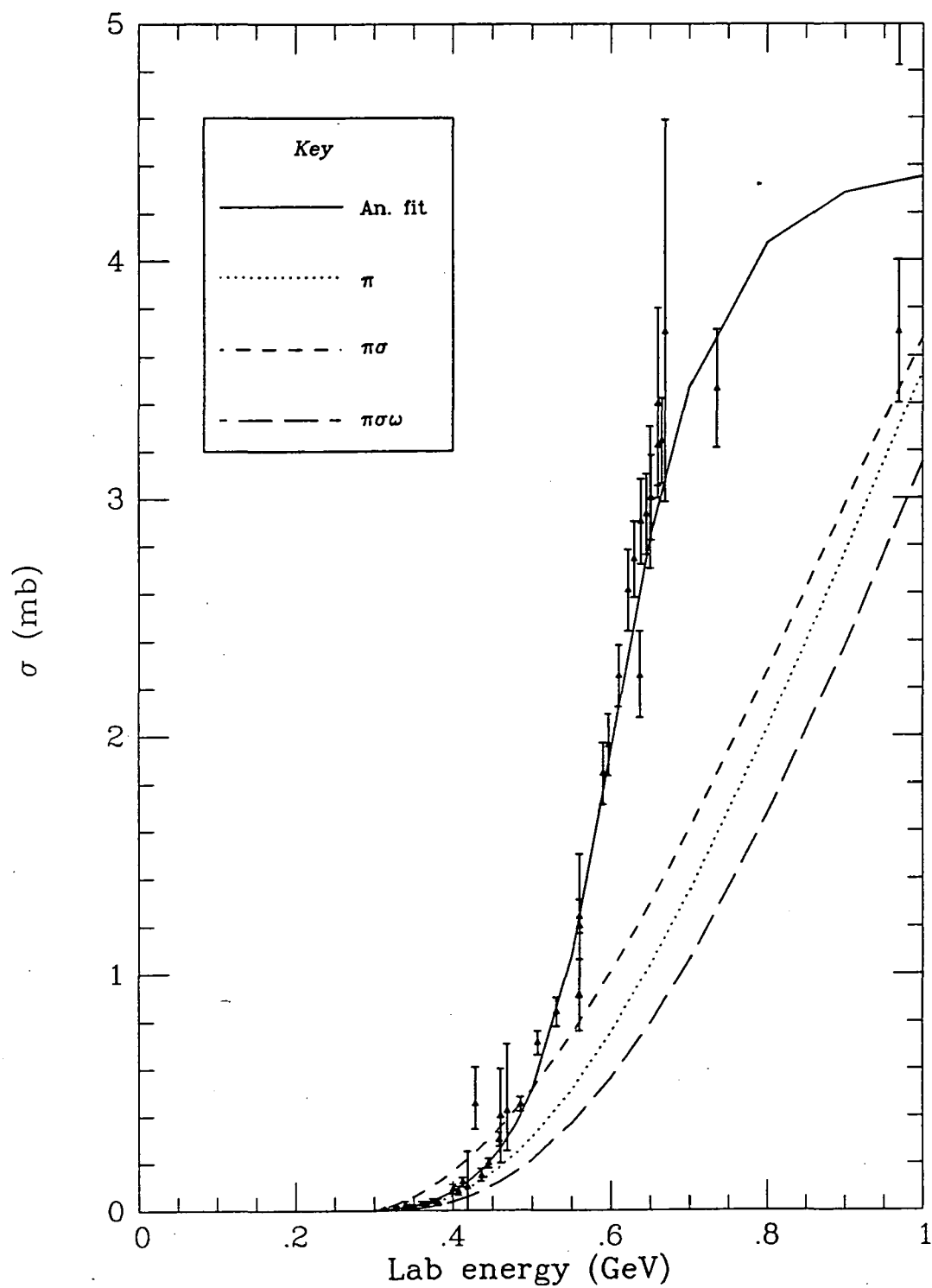
Figure 4.8   The Combined Boson Exchange Cross-sections σ_π, $\sigma_{\pi\sigma}$ and $\sigma_{\pi\sigma\omega}$ for $pp \to pp\pi^0$.
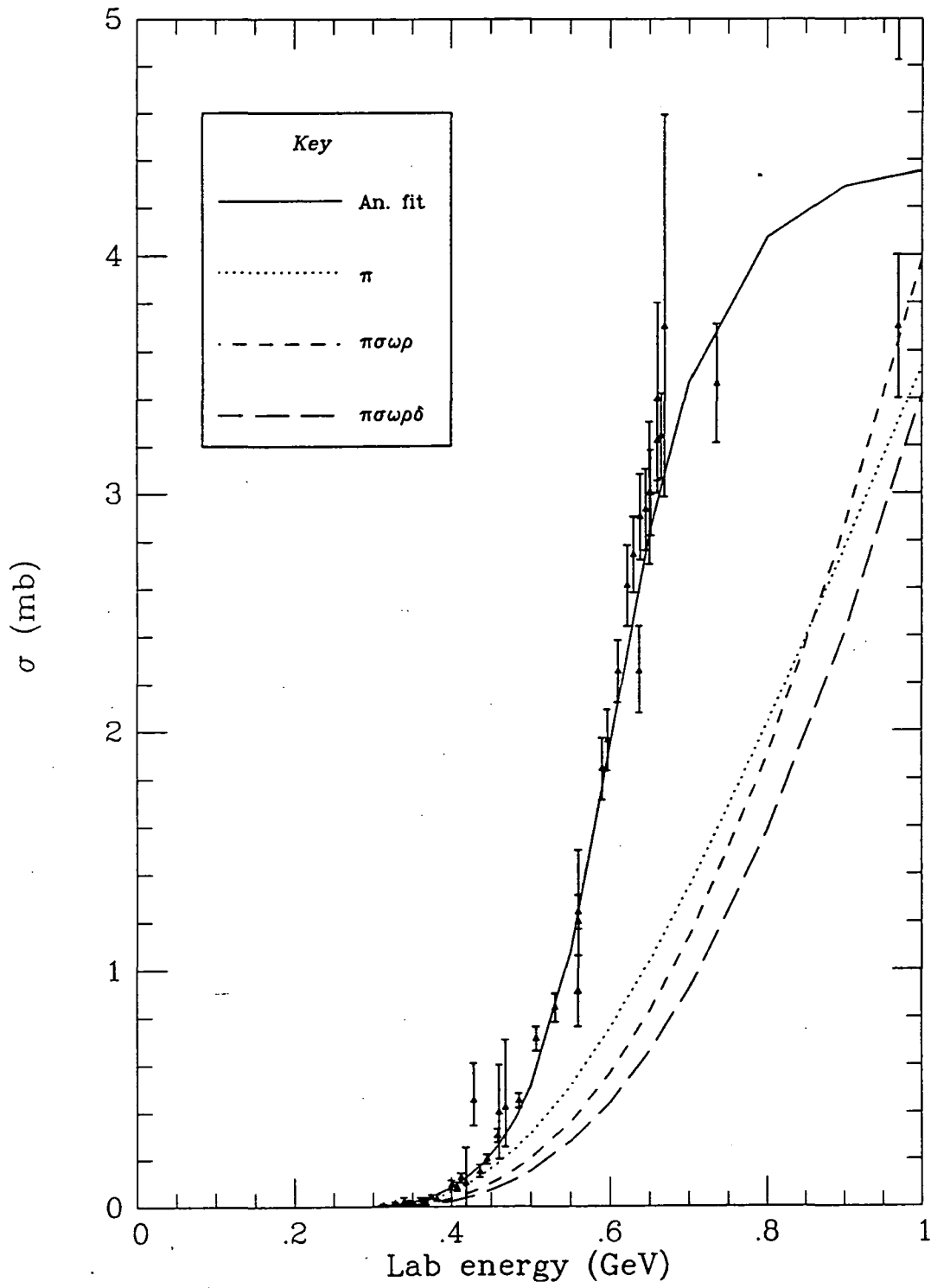
Figure 4.9 The Combined Boson Exchange Cross-sections σ_π, $\sigma_{\pi\sigma\omega\rho}$ and $\sigma_{\pi\sigma\omega\rho\delta}$ for $pp \rightarrow pp\pi^0$.
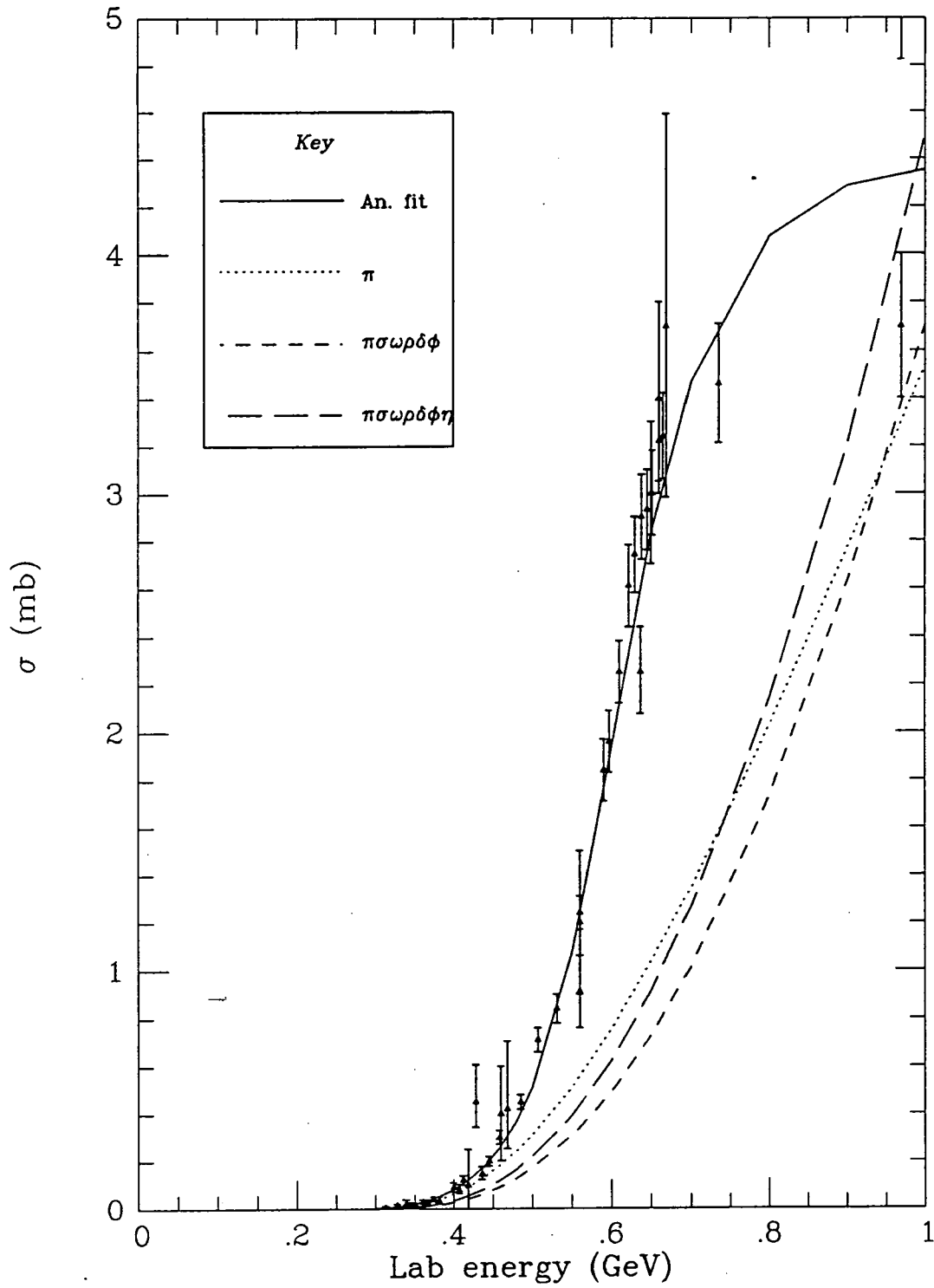
Figure 4.10 The Combined Boson Exchange Cross-sections σ_π, $\sigma_{\pi\sigma\omega\rho\delta\phi}$ and $\sigma_{\pi\sigma\omega\rho\delta\phi\eta}$ for $pp \to pp\pi^0$.

Table 4.5   "Errors" on Combined Boson Exchange Cross-Sections

T_{lab} (Gev)	ϵ_π	$\epsilon_{\pi\sigma}$	$\epsilon_{\pi\sigma\omega}$	$\epsilon_{\pi\sigma\omega\rho}$	$\epsilon_{\pi\sigma\omega\rho\delta}$	$\epsilon_{\pi\sigma\omega\rho\delta\phi}$	$\epsilon_{\pi\sigma\omega\rho\delta\phi\eta}$
0.30	0.88	0.99	0.54	0.35	0.05	0.31	0.00
0.31	0.80	0.98	0.37	0.23	0.30	0.38	0.00
0.32	0.73	0.96	0.27	0.16	0.46	0.38	0.00
0.33	0.67	0.94	0.21	0.11	0.52	0.38	0.00
0.34	0.62	0.92	0.17	0.08	0.55	0.37	0.00
0.35	0.58	0.90	0.14	0.05	0.55	0.36	0.00
0.36	0.54	0.88	0.12	0.03	0.55	0.36	0.00
0.37	0.51	0.86	0.11	0.02	0.54	0.35	0.00
0.38	0.49	0.84	0.09	0.00	0.54	0.35	0.00
0.39	0.46	0.81	0.08	0.01	0.54	0.34	0.00
0.40	0.44	0.79	0.07	0.02	0.52	0.34	0.00
0.42	0.41	0.75	0.05	0.04	0.51	0.33	0.00
0.44	0.37	0.70	0.03	0.05	0.49	0.32	0.00
0.46	0.35	0.66	0.02	0.06	0.48	0.31	0.00
0.48	0.32	0.62	0.00	0.07	0.46	0.30	0.00
0.50	0.29	0.57	0.03	0.09	0.46	0.30	0.00
0.55	0.23	0.47	0.06	0.09	0.43	0.28	0.00
0.60	0.18	0.38	0.11	0.10	0.41	0.27	0.00
0.65	0.12	0.29	0.15	0.11	0.39	0.26	0.00
0.70	0.06	0.21	0.20	0.12	0.38	0.25	0.00
0.80	0.06	0.06	0.28	0.13	0.35	0.24	0.00
0.90	0.16	0.08	0.35	0.12	0.33	0.22	0.00
1.00	0.27	0.22	0.43	0.13	0.32	0.21	0.00
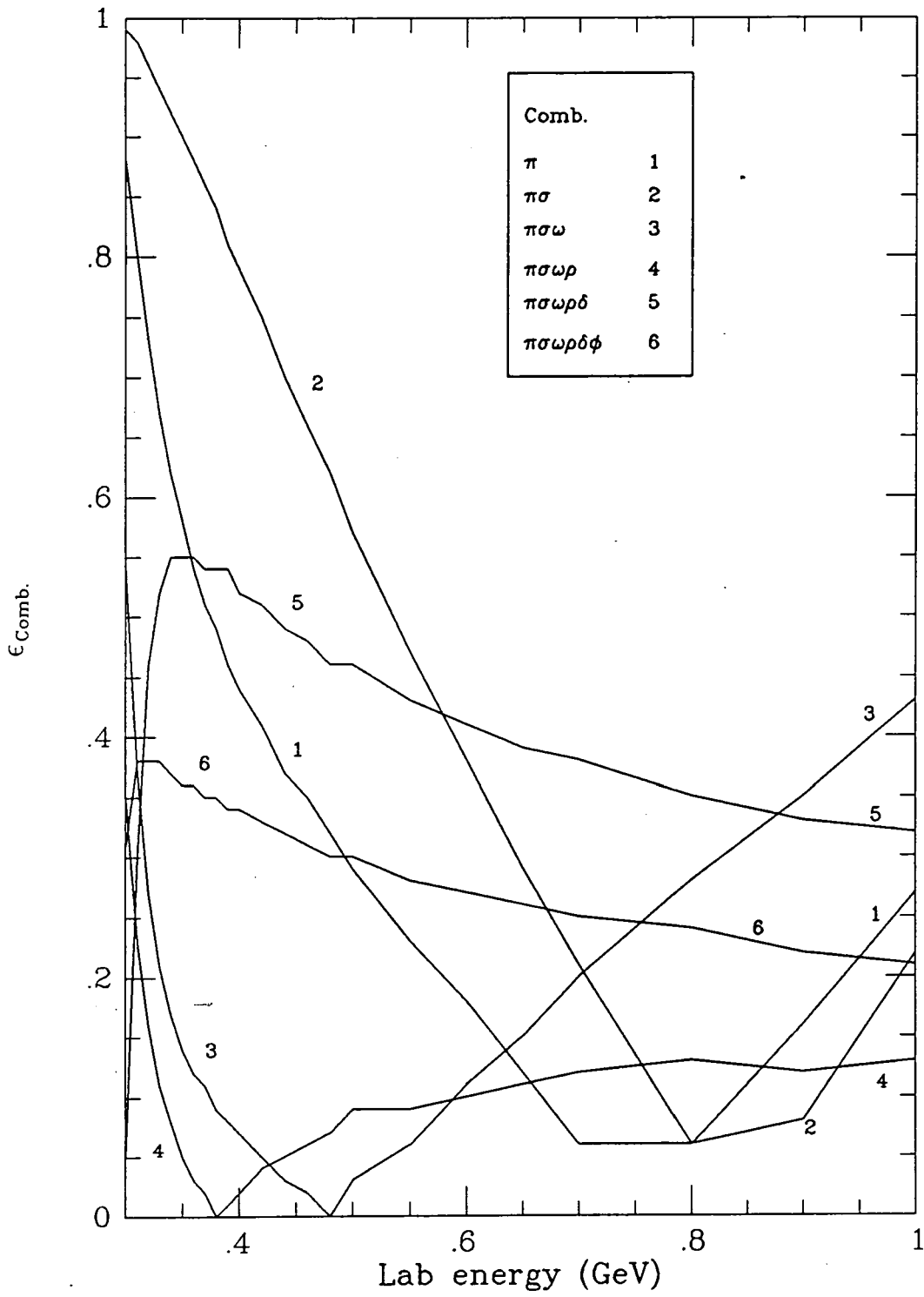
Figure 4.11 "Errors" on Combined Boson Exchange Cross-sections, defined in (4.96).

Table 4.5 and Figure 4.11 are useful for assessing the possibility of using subsets of the mesons which may give a reasonable representation of σ_T.

Firstly, one can test the expectation that δ, ϕ and η will be less important and could perhaps be ignored. If this were true one would expect that ϵ for $\sigma_{\pi\sigma\omega\rho}$ would be very small at all energies. From Table 4.5 and Figure 4.11 one can see that this is not the case. At $T_{lab} = 1.0 GeV$ $\epsilon_{\pi\sigma\omega\rho} = 0.13$ which may be acceptable, but at $T_{lab} = 0.3 GeV$ $\epsilon_{\pi\sigma\omega\rho} = 0.35$ which is probably not. One can understand this as follows. The single meson exchange cross-sections tell us about the magnitude of $\sum |\mathcal{M}_\alpha|^2$ where α is a given meson. Even if $\sum |\mathcal{M}_\alpha|^2$ squared is small for a given meson, for example ϕ, an interference term such as $\sum \mathcal{M}_\alpha \cdot \mathcal{M}_\beta^*$ which will be involved in calculating σ_T may not be negligible if $\mathcal{M}_\beta$ is large. So, for example, terms like $\sum \mathcal{M}_\phi \mathcal{M}_\sigma^*$ may give a significant contribution to σ_T.

Table 4.5 gives little evidence that any subset of mesons will give a reasonable representation of σ_T for all considered energies. There is certainly no sign of the representation of σ_T getting better as subsequent mesons are included with π in the order σ, ω, ρ, δ, ϕ then η. It seems that one must include all the meson exchanges if one is to be sure of obtaining a reasonable representation of the OBE amplitude.

4.3.1.5 The Importance of the Form Factors

I have recalculated the OPE cross-section for pion production with the form factor set to 1.0. I shall refer to the resulting cross-section function as σ'_π. σ'_π is plotted in Figure 4.12, and the values of σ'_π and σ_π are given in Table 4.6. σ'_π is consistently larger than σ_π. At $T_{lab} = 0.3 GeV$ $\sigma'_\pi/\sigma_\pi \simeq 1.3$ while at $T_{lab} = 1.0 GeV$ $\sigma'_\pi/\sigma_\pi \simeq 2.34$. This is consistent with the expected behaviour of a form factor which is to reduce the effective coupling as the modulus of the four-momentum transfer increases. As the form factor may reduce the cross-section by a factor of about 2 it is an important element of the calculation and omitting it introduces an unnecessary error.

It is interesting to note that by using $f_\pi = m_N m_\pi / F_\pi \simeq 1.4$ for the coupling constant of the produced pion as opposed to $f_\pi = 0.99$, which is the pion pseudovector coupling constant (see Section 4.2.3), σ'_π is reduced by a factor of about 2. This is approximately the same as the effect of including form factors. Turner *et*

73

Table 4.6   Cross-sections With and Without Form Factor

T_{lab} (Gev)	σ_π (μb)	σ'_π (μb)	T_{lab} (GeV)	σ_π (μb)	σ'_π (μb)
0.30	0.332	0.434	0.42	94.6	141.
0.31	1.13	1.50	0.44	136.	207.
0.32	2.61	3.52	0.46	186.	288.
0.33	4.99	6.79	0.48	244.	386.
0.34	8.46	11.7	0.50	311.	500.
0.35	13.2	18.4	0.55	511.	859.
0.36	19.4	27.4	0.60	756.	1320.
0.37	27.3	38.8	0.65	1040.	1890.
0.38	36.9	53.0	0.70	1350.	2550.
0.39	48.3	70.1	0.80	2030.	4140.
0.40	61.7	90.4	0.90	2770.	6040.
-	-	-	1.00	3540.	8200.

al [51] (see Section 4.3.3.2), who do not include form factors, use $f_\pi = 1.00$ at the exchanged pion vertices and $f_\pi = m_N m_\pi / F_\pi$ at the produced pion vertex and thus obtain similar results for OPE to those given in Section 4.3.1.4. $f_\pi = m_N m_\pi / F_\pi$ comes from the simplest version of the Goldberger-Treiman[52] relation which is only approximately true.

4.3.1.6 The Role of the Δ Baryon

The diagrams included in the previous computations are not the only possible diagrams, even in the Born approximation. As well as these diagrams which contain a proton propagator one should also consider diagrams like the one in Figure 4.13 which contain a $\Delta^+(\sim 1230 MeV)$ baryon propagator.

The Δ^+ is a $\pi^0 p$ resonance formed in this process, i.e.,

$$pp \rightarrow p\Delta^+ \rightarrow pp\pi^0$$

The threshold for Δ^+ production is at $T_{lab} = 0.63 GeV$ so the Δ^+ propagator
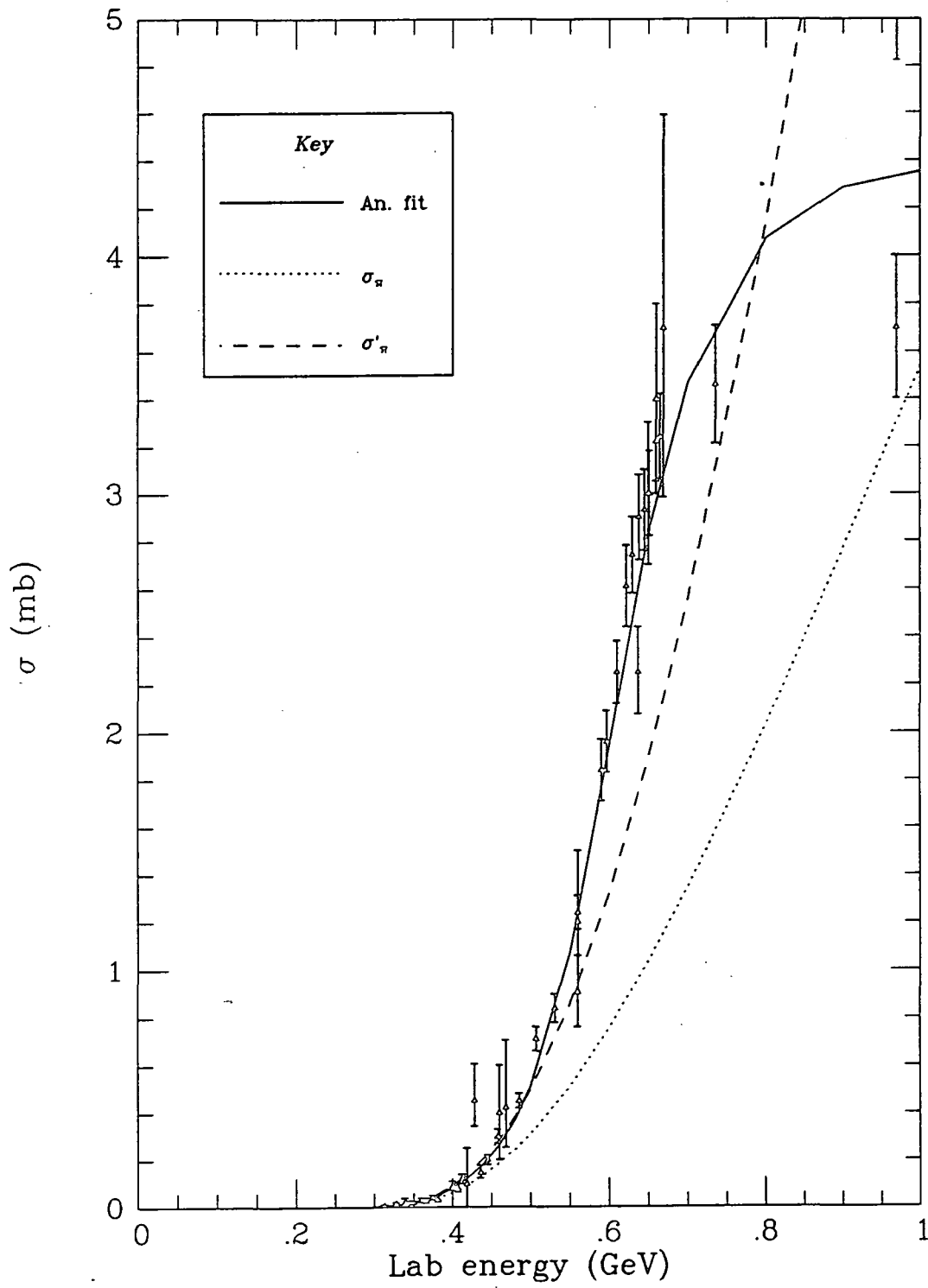
Figure 4.12 The Effect of the Form Factor (4.16) on the Cross-section for $pp \rightarrow pp\pi^0$.

75
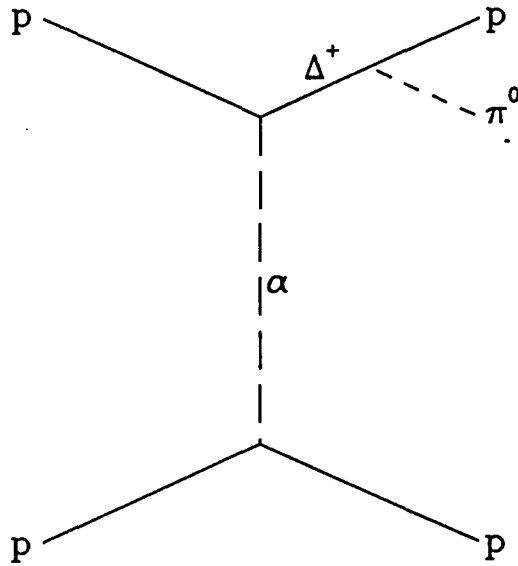
Figure 4.13   An Example Δ^+ Propagator Diagram fo $pp \rightarrow pp\pi^0$.

diagram should contribute to the $pp \rightarrow pp\pi^0$ matrix element. Figure 4.14 shows a plot of $\sigma_\pi - \sigma_A$, where σ_A is the analytic fit to the experimental data. This graph has a resonance like shape which leads one to expect that diagrams such as Figure 4.13 give a significant contribution to $pp \rightarrow pp\pi^0$.

By including more meson exchanges with the nucleon propagator one hopes that one is improving the representation of the background to the above resonance reaction. In order to verify this it would be necessary to compute $\sigma_{pp \rightarrow pp\pi^0}$ with the Δ^+ resonance diagrams included. There is some evidence in the literature that by including such diagrams one can get a reasonable fit to the data [53].

4.3.2 Conclusions About OBE Fits And Their Possible Application To Axion Production

By studying the process $pp \rightarrow pp\pi^0$ and the OBE approximations to the amplitude for this process one hopes to draw conclusions about the OBE fit that can best be used to describe the similar process $pp \rightarrow ppa$. Unfortunately, it is impossible to fit the $pp \rightarrow pp\pi^0$ cross-section very well with OBE diagrams alone
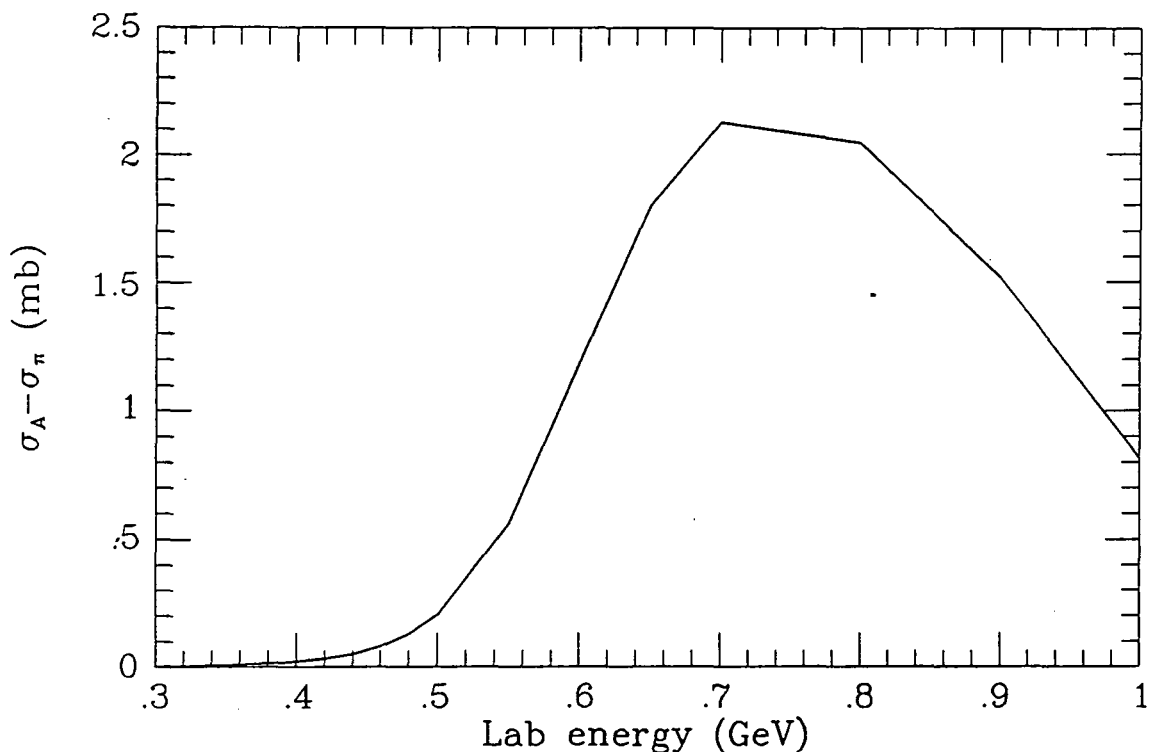
Figure 4.14 An Indication of the Importance of the Δ^+ Contribution to the $pp \rightarrow pp\pi^0$ Cross-section.

because Δ^+ resonance diagrams will also be important for this process. Without including Δ^+ resonance diagrams one can only conclude that OBE amplitudes give a $pp \rightarrow pp\pi^0$ cross-section which is of the right order of magnitude. It is worth noting here that the process $pp \rightarrow ppa$ in the nascent neutron star takes place at energies which are well below the threshold for Δ production and so one does not have the complication of the extra Δ diagrams for that process.

Having dispensed with the ideal of an exact or near exact fit to $pp \rightarrow pp\pi^0$ data being achieved one must resort to self-consistency arguments to justify the use of different meson exchange combinations. However, as we have seen in Section 4.3.1.4, there is no subset of the exchanged mesons which will give an acceptable representation of σ_T, the cross-section calculated from the matrix element which includes all seven meson exchanges. One must conclude from this study that all seven meson exchanges should be used for calculating the $pp \rightarrow ppa$ amplitude.

4.3.3 Reported Work on Pion Production and its Relationship to Axion Production

4.3.3.1 Choi, Kang and Kim's work on Pion Production

Choi, Kang and Kim[54] proposed a novel method of estimating the nucleon-nucleon-axion bremsstrahlung ($NN \to NNa$) spin averaged squared matrix element. The frequently used one pion exchange (OPE) amplitude may not be a sufficiently good approximation to the ($NN \to NNa$) amplitude, and Choi *et al*'s method was proposed as an improvement to this crude approximation or, at the very least, as a test for its validity.

The processes $pp \to ppa$ and $pp \to pp\pi^0$ are very similar since both the axion and the pion have pseudovector couplings to the proton. Naively, one would expect the differences between the amplitude for the two processes would be caused by the differences between the masses and the couplings of the axion and the pion. This observation is the motivation for Choi *et al*'s method.

For $pp \to pp\pi^0$ there exists experimental data on the cross-section above about $350 MeV$. A direct link with experiment is therefore available for this process, which is, of course, not available for axion production.

According to Choi *et al*, the spin summed, squared matrix element, $\sum |\mathcal{M}|^2$ for $pp \to ppa$ can be obtained from $\sigma_{pp \to pp\pi^0}$. This is achieved by dividing $\sigma_{pp \to pp\pi^0}$ by the phase space factor, multiplying by the flux factor, and replacing the pion-proton coupling constant by the axion-proton coupling constant. For the integrated Lorentz-invariant phase space of the final state, $pp\pi^0$, Choi *et al* use

$$dQ_3 = \frac{1}{128\sqrt{2}\pi^2} \sqrt{\frac{m_\pi}{m_N}} \frac{(\sqrt{s} - 2m_N - m_\pi)^2}{(1 + m_\pi/2m_N)^{\frac{3}{2}}}, \qquad (4.97)$$

which is valid when the final state particles are non-relativistic[55], and is accurate to about 5% over the laboratory energy range $0.3 \leq T_{lab} \leq 1.0 GeV$[51]. The flux factor employed is $2s\sqrt{1 - 4m_N^2/s}$. The axion pseudoscalar coupling constant is taken to be g/F_a where g is unknown, and the pion coupling constant is taken to be f_π/m_π , as in Section 4.3.1. Their phenomenological estimate of the spin

averaged, squared matrix element is

$$\frac{1}{8} \sum_{spins} |\mathcal{M}|^2_{a,phen} \simeq 256\sqrt{2}\pi^2 \left[\frac{m_\pi g}{f_\pi F_a}\right]^2 \sigma_{pp \to pp\pi^0} \left[\frac{m_N}{m_\pi}\right]$$

$$\times \frac{^3\sqrt{1 + m_\pi/2m_N}\sqrt{1 - 4m_N^2/s}}{(1 - 2m_N/\sqrt{s} - m_\pi/\sqrt{s})^2},$$ (4.98)

in which it is assumed that $\sum_{spins} |\mathcal{M}|^2$ is a constant for both axion production and pion production. †

The constant matrix element approximation for the $pp \to ppa$ gives

$$\frac{1}{8} \sum_{spins} |\mathcal{M}|^2_{a,const} = 32\left[\frac{f_\pi}{m_\pi}\right]^4 g_{an}^2 m_N^2 = 128\left[\frac{f_\pi}{m_\pi}\right]^4 \left[\frac{g}{F_a}\right]^2 m_N^4,$$ (4.99)

(see Section 5.3.2.2).

Choi *et al* define an over-estimation ratio for the OPE constant matrix element approximation as

$$r = \frac{\sum |\mathcal{M}|^2_{a,const}}{\sum |\mathcal{M}|^2_{a,phen}} = \frac{3.53 \times 10^3}{\tilde{\sigma}} \frac{(1 - 2m_N/\sqrt{s} - m_\pi/\sqrt{s})^2}{\sqrt{1 - 4m_N^2/\sqrt{s}}},$$ (4.100)

where $\sigma_{pp \to pp\pi^0} = \tilde{\sigma} \times 10^{28} cm^2$ has been used. They find that $r = 4.4$ and 3.4 for laboratory energies of 400 and 500 GeV respectively, and conclude that the OPE constant matrix element approximation does not unreasonably over-estimate the $pp \to ppa$ production rate.

In order that Choi *et al*'s phenomenological estimate of the axion production $\sum |\mathcal{M}|^2$ be reasonable it is necessary that

1) $\sum |\mathcal{M}|^2$ is a constant for both $pp \to ppa$ and $pp \to pp\pi^0$ and

2) the non-relativistic approximation to the phase space volume is applicable.

As regards (1), Brinkmann and Turner[42] show that the OPE approximation to the $pp \to ppa$ matrix element reduces to a constant if

---

† N.B. I have replaced "$g_A/2f_\pi$" in Choi *et al*'s expression by f_π/m_π for consistency with the Feynman rules defined previously. f_π in this thesis and the "f_π" of Choi *et al* are not the same quantity, their "f_π" represents the pion decay constant.

a) the nucleons are non-relativistic,

b) the axion mass can be set to zero for kinematical purposes and

c) the modulus of the four-momentum transfer is much larger than the pion mass.

The last of these approximations is questionable even in the condition in the nascent neutron star interior where Turner claims the approximation to be reasonable (see Section 5.3.2.2). There is no reason to expect that the full matrix element for pion or axion production reduces to a constant in any circumstances. It is the supposed full matrix element which enters into equation (4.98). It is not established that the OPE pion production matrix element should be constant for the laboratory energies pertinent to pion production.

As regards (2), this is probably a good approximation near threshold. However, the assumption of a non-relativistic pion contradicts the assumption of small pion mass which is necessary to obtain a constant matrix element in the OPE approximation (assumption b) above with pion replacing axion). Also, it is worth noting that the values of T_{lab} used to estimate r are not consistent with typical nascent neutron star temperatures of $20 - 80 MeV$.

A comparison of the Born approximation OPE cross-section with the experimentally measured cross-section for $pp \rightarrow pp\pi^0$ should be useful in testing the validity of using the Born approximation matrix element for $pp \rightarrow ppa$. However, the method of Choi et al contains too many crude, unjustified approximations to be anything more than an order of magnitude estimate of the validity, or otherwise, of the OPE approximation.

4.3.3.2 Turner, Kang and Steigman's Calculation of the Pion Production Cross-Section

Turner et al [51] have investigated the validity of the OPE pion production matrix element. They calculated the fully relativistic OPE matrix element for $pp \rightarrow pp\pi^0$ from the eight required Feynman diagrams (Figure 4.5). They obtained a rather lengthy expression for the summed matrix element (see [51]). Using this, they calculated the pion production cross-section for $0.3 \leq T_{lab} \leq 1.0 GeV$ and found agreement with the experimental data to within a factor of 3.

For this calculation, which was performed using a Monte Carlo integration algorithm, they employed the non-relativistic approximation to the phase space volume as given above (4.97). They found this approximation to be accurate to around 5%. Even so, there seems little point in using the non-relativistic approximation when it is perfectly straightforward to treat the phase space relativistically.

There are two errors in Turner *et al*'s spin summed squared matrix element. Firstly, the pion mass term in the denominator of the nucleon propagator is missing. Taking, for example, the first of the eight diagrams in Figure 4.5, with the proton and produced pion momenta represented by c and e respectively, the denominator of the proton propagator should be

$$[(c + e)^2 - m_N^2] = [2(c.e) + m_\pi^2].$$ (4.101)

In Turner *et al*'s matrix element the same nucleon propagator is given by $2(c.e)$. This error is probably not numerically serious. The second error concerns the pion coupling constant. Turner *et al* use different couplings for the exchanged and produced pions. Barring the momentum dependence of the coupling constant via a form factor, which Turner *et al* do not consider, the pion-proton-proton pseudovector coupling constant should be the same for all vertices with a value $f_\pi/m_\pi \simeq 7.16$, as is introduced in Section 4.2.3. Using this value of the coupling at all vertices would increase Turner *et al*'s results by a constant factor

$$\left(\frac{f_\pi}{m_\pi}\right)^6 m_\pi^4 4F_\pi^2 \simeq 1.76 \approx 2,$$

which is the factor Turner *et al* also quote for using one of their couplings,

$$1/m_\pi, \quad i.e. \ f_\pi \simeq 1,$$

throughout. They also quote a factor of $\sim 1/4$ if their alternative coupling $1/4F_\pi$ is used throughout. The use of two different pion coupling constants is not acceptable. By using the two different coupling constants Turner *et al* "mimic", possibly unintentionally, the order of magnitude of the effect of the form factor used in Section 4.3.1. A large omission from all the reported work on the Born approximation OPE pion production cross-section in relation to axion production is the form factor at the interaction vertices which takes account of the proton's structure. In the next chapter we shall employ the experience gained with pion production to estimate the axion production rate in supernovae.

5 Axion Production in a Nascent Neutron Star
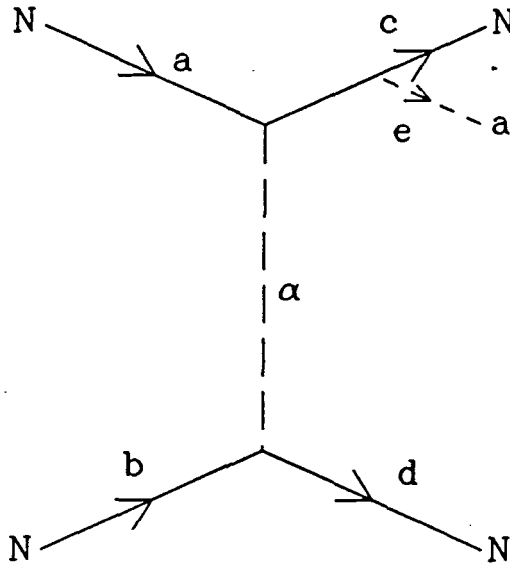
Figure 5.1   A Typical $NN \to NNa$ Diagram.

5.1 Introduction

The dominant axion production process in the interior of a nascent neutron star is nucleon-nucleon-axion bremsstrahlung[20,42], *i.e.* the process $NN \to NNa$. In the one-boson-exchange (OBE) approximation this reaction proceeds via diagrams of the form shown in Figure 5.1. Most work has centred on the one-pion-exchange (OPE) approximation which only includes diagrams in which $\alpha = \pi$.

The axion energy emission rate per unit volume, $\dot{\epsilon}_a$, is given by[42]

$$\dot{\epsilon}_a = \int dQ_2 dQ_3 S \sum_{spins} |\mathcal{M}|^2 E_e F_a F_b (1 - F_c)(1 - F_d), \tag{5.1}$$

where

$$dQ_2 = \frac{d^3 p_a}{(2\pi)^3 2E_a} \frac{d^3 p_b}{(2\pi)^3 2E_b}, \tag{5.2}$$

is the phase space for the two initial particles,

$$dQ_3 = \Pi_{i=c,d,e} \left[\frac{d^3 p_i}{(2\pi)^3 2E_i} \right] \delta^4(a + b - c - d - e) \qquad (5.3)$$

is the phase space for the three final state particles, S is the symmetry factor for identical particles in the initial and final particle states, $\sum_{spins} |\mathcal{M}|^2$ is the $NN \to NNa$ matrix element summed over nucleon spin states and

$$F_i = F(E_i, \mu_i) = \frac{1}{\exp[(E_i - \mu_i)/T] + 1} \qquad (5.4)$$

is the Fermi-Dirac phase space distribution function for particle i at temperature T, with chemical potential μ_i. The factors $(1 - F_c)$ and $(1 - F_d)$ are the Pauli blocking factors which take into account the inhibiting properties of the exclusion principle in degenerate matter on the final states available to the reaction.

Various approximations which simplify the evaluation of $\dot{\epsilon}_a$ have been made in the literature[42,31,21,56]. Section 5.3 will discuss these approximations. In Section 5.2 calculations of $\dot{\epsilon}_a$ which assume that the OBE approximation is valid will be discussed. However, no kinematical approximations will be made in Section 5.2.

5.2 Relativistic Evaluation of the Axion Emission Rate

It is possible to considerably simplify the evaluation of $\dot{\epsilon}_a$ in equation (5.1) if one makes a number of assumptions concerning the momenta involved in this equation. I shall discuss the approximations used by various authors in Section 5.3. However, it is not necessary to make any kinematical approximations in order to evaluate $\dot{\epsilon}_a$ from equation (5.1). By evaluating $\dot{\epsilon}_a$ directly from equation (5.1) using relativistic kinematics, one can give a concrete assessment of the errors which previous authors have introduced by using approximate expressions. Also, the effective kinematical mass of the nucleons can be much smaller than $1 GeV$ at the temperatures and densities pertinent to the interior of the nascent neutron star (see Section 5.2.5.5) and therefore the usual assumption that non-relativistic kinematics is appropriate may not be good enough for these reduced effective masses. It will be necessary to use a full relativistic calculation of $\dot{\epsilon}_a$ if the effective nucleon mass is small. In this section I shall describe a fully relativistic evaluation of $\dot{\epsilon}_a$.

5.2.1 Reduction of the 15-D Phase Space Integral

Equation (5.1) contains a 15-dimensional integral over the phase space for the five participating particles,

$$dP = dQ_2 dQ_3, \qquad \cdot \qquad (5.5)$$

where dQ_2 and dQ_3 are defined in equations (5.2) and (5.3). I shall examine dQ_2 and dQ_3 separately in Sections 5.1.1.1 and 5.1.2.1. We shall find that it is possible to reduce the 15-dimensional integral to an 8-dimensional integral without making any approximations.

5.2.1.1 Three Particle Phase Space

The three particle phase space for the final-state particles is most conveniently evaluated in the centre of mass frame. Since the phase space is Lorentz invariant,

$$dQ_3' = dQ_3, \qquad (5.6)$$

where the prime is used to denote the centre of mass frame. We have already considered dQ_3' in Section 4.3.1.1. We obtained

$$\int dQ_3' = \frac{1}{256\pi^5} \int_{-1}^{1} d\gamma_c' \int_0^{2\pi} d\phi_c' \int_0^{2\pi} d\phi' \int \int dE_c' dE_d' \qquad (5.7)$$

The use of c.o.m. variables is also convenient for evaluating the matrix element (see Section 5.2.4).

As we saw in Section 4.3.1.3, the four-momenta for all five particles in the c.o.m. frame can be determined independently of ϕ_c'. We shall find that the whole of the integrand in equation (5.1) is independent of ϕ_c'. Integrating gives

$$\int dQ_3' = \frac{1}{128\pi^4} \int_{-1}^{1} d\gamma_c' \int_0^{2\pi} d\phi' \int \int dE_c' dE_d'. \qquad (5.8)$$

5.2.1.2 Two Particle Phase Space

The variables that appear in dQ_3' are the c.o.m. variables γ_c', ϕ', E_c' and E_d'. Using these variables together with the Mandelsta m variable, s, one can

compute the c.o.m. four-momenta of all five particles. The energies that appear in the expression for $\dot{\epsilon}_a$ (5.1) are evaluated in a star fixed frame. In order to calculate the energies of the five particles in this star fixed frame one needs to know the relationship between the two frames. The frames are related by a Lorentz transformation. In the c.o.m. frame one can define a vector $\vec{v}$ which defines the direction and magnitude of a Lorentz boost on the c.o.m. frame which will give the transformation to the star fixed frame. With the variables $\vec{v}$, s, γ'_c, ϕ', E'_c and E'_d one can define any particle energy in the star fixed frame via the equation

$$E_i = \gamma(E'_i - \vec{v}.\vec{p'_i}), \tag{5.9}$$

where $\gamma = 1/\sqrt{1 - v^2}$.

The phase space factor dQ_2 can be expressed in terms of $\vec{v}$ and s as we shall now show.

$$dQ_2 = \frac{d^3p_a d^3p_b}{4(2\pi)^6 E_a E_b}. \tag{5.10}$$

Integrating out unnecessary variables gives

$$dQ_2 = \frac{p_a^2 p_b^2}{2(2\pi)^5 E_a E_b} dp_a dp_b d\gamma_{ab} d\phi_a, \tag{5.11}$$

where γ_{ab} represents the cosine of the angle between $\vec{p}_a$ and $\vec{p}_b$, and ϕ_a represents the angle of rotation of $\vec{p}_a$ around $\vec{p}_a{}'$. For the two particle system alone one could integrate over ϕ_a. However, $\phi_a - \phi'_c$ is required to fully describe the five particle system, and since we have effectively set $\phi'_c = 0$ in dQ_3 we must keep $d\phi_a$ here and define $\phi_a = 0$ to be when $\hat{p}_a$, $\hat{p}'_c$ and $\hat{p}'_a$ are co-planar. Also, a little thought shows that $\phi_a = \phi_v$, where ϕ_v represents the angle of rotation of $\hat{v}$ about $\hat{p}'_a$, since $\hat{p}_a$, $\hat{p}_b$, $\hat{p}'_a$ and $\hat{v}$ must be co-planar.

One can transform from the variable γ_{ab} to E'_a using

$$s = 4E'^2_a = 2m_N^2 + 2E_a E_b - 2p_a p_b \gamma_{ab}, \tag{5.12}$$

to give

$$dQ_2 = \frac{2E'_a}{(2\pi)^5} dE_a dE_b dE'_a d\phi_a, \tag{5.13}$$

where $EdE = pdp$ has also been used.

85

One can make a second transformation from (E_a, E_b) to (v, γ_v) using

$$E_{a,b} = \gamma(E'_a \mp v p'_a \gamma_v), \tag{5.14}$$

where $v = |\vec{v}|$, $\gamma = 1/\sqrt{1-v^2}$ and γ_v represents the cosine of the angle between $\hat{p}'_a$ and $\hat{v}$, to give

$$dQ_2 = \frac{4v^2\gamma^4 E_a'^2 p_a}{(2\pi)^5} dE'_a \, dv \, d\gamma_v \, \phi_v. \tag{5.15}$$

The region of integration is obvious. E'_a is bounded by m_N and ∞, v by 0 and 1, γ_v by -1 and $+1$ and ϕ_v by 0 and 2π, so

$$\int dQ_2 = \frac{4v^2\gamma^4 E_a'^2 p'_a}{(2\pi)^5} \int_{m_N}^{\infty} dE'_a \int_0^1 dv \int_{-1}^1 d\gamma_v \int_0^{2\pi} d\phi_v. \tag{5.16}$$

All that remains is to express the integrand in terms of E'_a, v, γ_v, ϕ_v, γ'_c, ϕ', E'_c and E'_d. The c.o.m. four-momenta in terms of E'_a, γ'_c, ϕ', E'_c and E'_d were given in Section 4.3.1.3 for pion production. The other variables that appear in equation (5.1) are the particle energies in the star fixed frame. These are given by

$$E_i = \gamma(E'_i - \vec{v}.\vec{p}_i{}'). \tag{5.17}$$

5.2.2 Fermi-Dirac Functions: Numerical Difficulties

The expression for evaluating $\dot{\epsilon}_a$, equation (5.1), contains the following combination of Fermi-Dirac functions, F_i, as defined in (5.4);

$$F_T(E_a, \ldots E_d, \mu_a \ldots \mu_d) = F(E_a, \mu_a)F(E_b, \mu_b)[1 - F(E_c, \mu_c)][1 - F(E_d, \mu_d)]. \tag{5.18}$$

If any $\hat{\mu}_i = (\mu_i - m_N) \gg T$, the degenerate nucleon limit, the corresponding Fermi-Dirac function tends to a step function, $i.e.$

$$\lim_{(\hat{\mu}_i/T)\to\infty} (F_i(E_i, \mu_i)) = 1 \quad (E_i < \mu_i)$$
$$= 0 \quad (E_i > \mu_i). \tag{5.19}$$

If we consider $nn \to nna$ or $pp \to ppa$, where $\mu_a = \mu_b = \mu_c = \mu_d = \mu$, this implies

that

$$\lim_{(\hat{\mu}_i/T)\to\infty} (F_i(E_i,\mu_i)) = 1 \quad \text{if} \quad E_a = E_b = E_c = E_d = \mu$$
$$= 0 \quad \text{otherwise.} \tag{5.20}$$

i.e. a delta function. (Note that in this extreme limit $\dot{\varepsilon}_a = 0$ since $E_e = 0$). The implication of the above is that as the nucleons become more degenerate F_T, and therefore the integrand in equation (5.1) becomes very strongly peaked around particular values of E_a, E_b, E_c and E_d. This peaking effect makes numerical evaluation of $\dot{\varepsilon}_a$ particularly difficult for high values of $y = \hat{\mu}/T$. A large number of integrand evaluations are required to evaluate $\dot{\varepsilon}_a$ in this case.

The evaluation of the required $NN \to NNa$ matrix element in equation (5.1), which will be described in Section 5.2.4, is computationally rather lengthy. Combining this with the above numerical difficulties could make the time required to evaluate $\dot{\varepsilon}_a$ prohibitively long for degenerate nucleons. In the next section I shall outline techniques which help to reduce the computer time required for numerically evaluating $\dot{\varepsilon}_a$.

5.2.3 Numerical Integration Technique

One could evaluate $\dot{\varepsilon}_a$ by applying a multi-dimensional integration algorithm directly to the required eight dimensional integral. However this would require evaluating $\sum_{spins}|\mathcal{M}|^2$ for each set of the eight integration variables. $\sum_{spins}|\mathcal{M}|^2$ only depends on the five variables E'_a, γ'_c, ϕ', E'_c and E'_d and, since the evaluation can be computationally lengthy, it wastes computer time to evaluate it for each set of values of all eight variables. For this reason the integration has been split into two sub-integrations such that $\sum_{spins}|\mathcal{M}|^2$ is evaluated only for different values of the five variables on which it depends. This separation is described in Section 5.2.3.1.

In Section 5.2.3.2 the choice of integration variables will be examined. It is possible to choose variables which simplify the integrand in the degenerate limit and thus speed up numerical evaluation of the required integrals.

87

5.2.3.1 Separation into Sub-Integrals

From equations (5.1), (5.8), (5.16) and (5.18) we obtain

$$\dot{\varepsilon}_a = \int f dE'_a dv d\gamma_v d\phi_v d\gamma'_c d\phi' dE'_c dE'_d, \qquad (5.21)$$

where

$$f \equiv \frac{1}{2(2\pi)^9} v^2 \gamma^4 E'^2_a p'_a S[\sum_{spins} |\mathcal{M}|^2] E_e F_T. \qquad (5.22)$$

We can split this integration as follows;

$$\dot{\varepsilon}_a = \int f_1 f_2 dE'_a d\gamma'_c d\phi' dE'_c dE'_d, \qquad (5.23)$$

where

$$f_1 \equiv 2E'_a p'_a v^2 \gamma^4 E_e F_T dv d\gamma_v d\phi_v \qquad (5.24)$$

and

$$f_2 \equiv \frac{E'_a S}{4(2\pi)^9} \sum_{spins} |\mathcal{M}|^2. \qquad (5.25)$$

We can thus view the numerical integration as a five dimensional integration of the functions f_1 and f_2 over the c.o.m. variables E'_a, γ'_c ϕ', E'_c and E'_d. In order to evaluate f_1 we must perform a three dimensional integration which is subordinate to this main integration. The principle advantage of this approach is that one only needs to evaluate the matrix element for different sets of the variables on which it depends. For complicated matrix elements which take a long time to evaluate computationally, this method will reduce the running time of the integration routine.

The total relative error for the combined integration can be evaluated from the relative errors of each individual integration. We can take the relative error for the subordinate three dimensional integration to be ϵ_1, *i.e.*

$$f_1 = (1 \pm \epsilon_1) f_1^N, \qquad (5.26)$$

where f_1^N is the numerically obtained value approximating to f_1. Also, we can take the relative error for the five dimensional integration to be ϵ_2. One then finds

that

$$\dot{\varepsilon}_a = (1 \pm \epsilon_1)(1 \pm \epsilon_2)\dot{\varepsilon}_a^N, \qquad (5.27)$$

where $\dot{\varepsilon}_a^N$ is the numerical approximation to $\dot{\varepsilon}_a$. Taking the same sign in each bracket gives the worst case errors

$$\dot{\varepsilon}_a = [1 \; {}^{+(\epsilon_1+\epsilon_2+\epsilon_1\epsilon_2)}_{-(\epsilon_1+\epsilon_2-\epsilon_1\epsilon_2)}]\dot{\varepsilon}_a^N. \qquad (5.28)$$

For reasonable values of ϵ_1 and ϵ_2 one can assume that $\epsilon_1\epsilon_2 \ll (\epsilon_1 + \epsilon_2)$ and thus obtain a simple expression for the total error, ϵ_T, as

$$\epsilon_T = \epsilon_1 + \epsilon_2, \qquad (5.29)$$

i.e.

$$\dot{\varepsilon}_a = (1 \pm \epsilon_T)\dot{\varepsilon}_a^N. \qquad (5.30)$$

5.2.3.2 Variables Used for Numerical Integration

Even with the split integral formulation the computational time required to evaluate $\dot{\varepsilon}_a$ in the degenerate limit can be prohibitive. This is due to the peaked nature of the integrand which has been traced to the Fermi-Dirac functions. One can ease the difficulty through a careful choice of integration variables.

As a first step we will transform from the variables v and γ_v back to the variables E_a and E_b, i.e. using

$$2v^2\gamma^4 E'_a p'_a dv d\gamma_v = dE_a dE_b, \qquad (5.31)$$

(see Section 5.1.1.2). The region of integration for $dE_a dE_b$ is not as immediately obvious as was the case for $dv d\gamma_v$. The region is most easily obtained by mapping the region of integration for $dv d\gamma_v$ onto the (E_a, E_b) plane. If one does this one

obtains

$$m_N \leq E_a \leq \infty \qquad (5.32)$$

and

$$E_b^{min} \leq E_b \leq E_b^{max}, \qquad (5.33)$$

where

$$E_b^{min,max} = [E_a(E_a'^2 + p_a'^2) \mp 2p_a'E_a'p_a]/m_N^2. \qquad (5.34)$$

This gives

$$f_1 = \int_{m_N}^{\infty} \int_{E_b^{min}}^{E_b^{max}} \int_0^{2\pi} E_e F_a F_b (1 - F_c)(1 - F_d) dE_a dE_b d\phi_v. \qquad (5.35)$$

One can now use the substitutions

$$x_1 \equiv \frac{F(E_a, \mu_a)}{F(m_N, \mu_a)} \qquad (5.36)$$

and

$$x_2 \equiv \frac{F(E_b, \mu_b) - F(E_b^{max}, \mu_b)}{F(E_b^{min}, \mu_b) - F(E_b^{max}, \mu_b)}, \qquad (5.37)$$

to give

$$f_1 = \int_0^1 \int_0^1 \int_0^{2\pi} E_e F(m_N, \mu_a)[F(E_b^{min}, \mu_b) - F(E_b^{max})]$$
$$\times T^2 \frac{(1 - F_c)(1 - F_d)}{(1 - F_a)(1 - F_b)} dx_1 dx_2 d\phi_v, \qquad (5.38)$$

where F_a and F_b can be determined from (5.36) and (5.37). The above integral is considerably easier to evaluate numerically as the integrand is not as sharply peaked as the original integrand. Another advantage of using x_1 and x_2 is that the values which one would expect to be important in computing the integral lie around the middle of the integration region. For example, in the extreme degenerate limit $x_1 = 0.5$ corresponds to $E_a = \mu_a$ and in this limit $\mu_a \simeq \epsilon_F$ the nucleon Fermi energy, which is the energy of all the nucleons which can participate in reactions. Thus by using x_1 as the integration variable one targets the energies around the Fermi energy in the degenerate limit.

One can further target the desired degenerate limit energy range by employing similar transformations to the variables E'_a, E'_c and E'_d. For example, in place of E'_a one can use the variable

$$y_1 \equiv \frac{F(E'_a, \bar{\mu})}{F(m_N, \bar{\mu})}, \qquad (5.39)$$

where

$$\bar{\mu} \equiv \frac{\mu_a + \mu_b}{2}. \qquad (5.40)$$

In doing this one is essentially assuming that the c.o.m. energies are similar to the energies in the star fixed frame, *i.e.* a non-relativistic limit. The validity of this assumption does not affect the final answer and reduces the computer time required to obtain that answer.

5.2.4 $NN \rightarrow NNa$ Matrix Elements

Up to this point an explicit form for $\sum_{spins} |\mathcal{M}|^2$ has not been given. As was observed in Section 4.1, the matrix element for $NN \rightarrow NNa$ is of a very similar form to that for $NN \rightarrow NN\pi^0$ since both the axion and the pion couple as pseudovector particles. I will assume, as have other authors, that the matrix elements for $NN \rightarrow NNa$ factorises in such a way that they can be well represented by Born approximation meson exchange diagrams similar to those employed in Section 4.3.1 to calculate the $pp \rightarrow pp\pi^0$ matrix element. For reasons of computational-speed and clarity the matrix elements are computed directly from the Feynman rules and the spin sums done explicitly rather than making use of trace techniques to evaluate $\sum_{spins} |\mathcal{M}|^2$.

5.2.4.1 pp/nn Matrix Elements

For the processes $pp \rightarrow ppa$ and $nn \rightarrow nna$ the matrix element can obtained from the corresponding $pp \rightarrow pp\pi^0$ matrix element simply by replacing the produced pion coupling constant F_π/m_π by the relevant axion coupling constant g_{ap} or g_{an}, and, of course, at the same time replacing m_π by m_a in any expressions which contain the produced particle mass, *i.e.*

$$\mathcal{M}_{pp \rightarrow pp\pi^0}^{m_{\pi^0} \rightarrow m_a} = \frac{f_\pi}{g_{ap} m_\pi} \mathcal{M}_{pp \rightarrow ppa} = \frac{f_\pi}{g_{an} m_\pi} \mathcal{M}_{nn \rightarrow nna}. \qquad (5.41)$$

The calculation of the spin-summed matrix element follows the technique outlined in Sections 4.3.1.2-3. The relative values of g_{ap} and g_{an} depend on the particular axion model employed, as discussed in Section 2.3.4. For each meson exchange there are eight contributing diagrams; these are shown in Figure 5.2.

5.2.4.2 np Matrix Elements

I shall examine the calculation of the matrix element for the process $np \rightarrow npa$ in some detail since this process has been incorrectly treated by Brinkmann and Turner[42], though this has been the most complete calculation of axion production rates to date (See Section 5.3.3).

a) Isospin considerations

Figure 5.3 shows the eight diagrams which are normally considered to contribute to the one pion exchange matrix element for $np \rightarrow npa$.

The pseudovector coupling constants for each vertex are explicitly given in the figure. In Section 4.2.2 I have described in detail the treatment of Born approximation diagrams for np elastic scattering. The treatment of $np \rightarrow npa$ is exactly analogous. The direct diagrams (1, 2, 3 and 4) and the exchange diagrams (5, 6, 7 and 8) must have a relative minus sign between them since they differ by the exchange of identical fermions, *i.e.* the nucleons. Brinkmann and Turner[42] did not include the relative minus sign between direct and exchange diagrams. Their reason for this was essentially that the neutron and proton are not identical fermions. This is true; however the $NN\pi$ couplings they employed, *i.e.* $f_{nn} = -f_{\pi}$, $f_{pp} = f_{\pi}$ and $f_{np} = \sqrt{2}f_{\pi}$, are derived using a theory which treats the neutron and proton as different states of the same particle, *i.e.* $I_3 = \pm\frac{1}{2}$ states of the nucleon, an $I = \frac{1}{2}$ particle, (see Section 4.2). This being the case one must keep the relative minus sign if one uses Brinkmann and Turner's conventions for the $NN\pi$ couplings. Obviously one can drop the minus sign if one uses $f_{nn} = f_{\pi}$ for the $nn\pi$ coupling. To avoid the above unpleasant confusion it is useful to include isospin Feynman rules as given in Section 4.2.1, and work with nucleon, rather than neutron and proton, states for all meson exchanges.

b)Additional diagrams

Carena and Peccei[17] pointed out that in the case of $np \rightarrow npa$ there are two
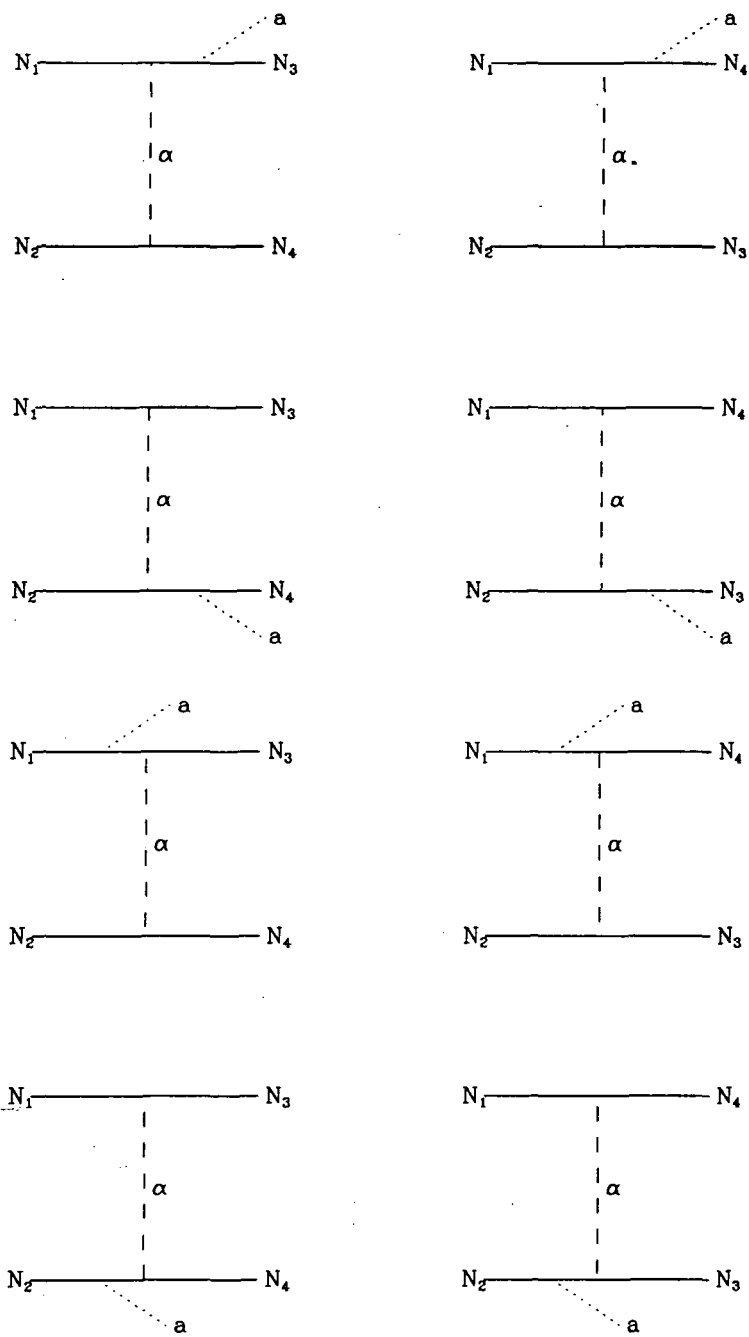
Figure 5.2 OBE Axion Bremsstrahlung Production Diagrams.
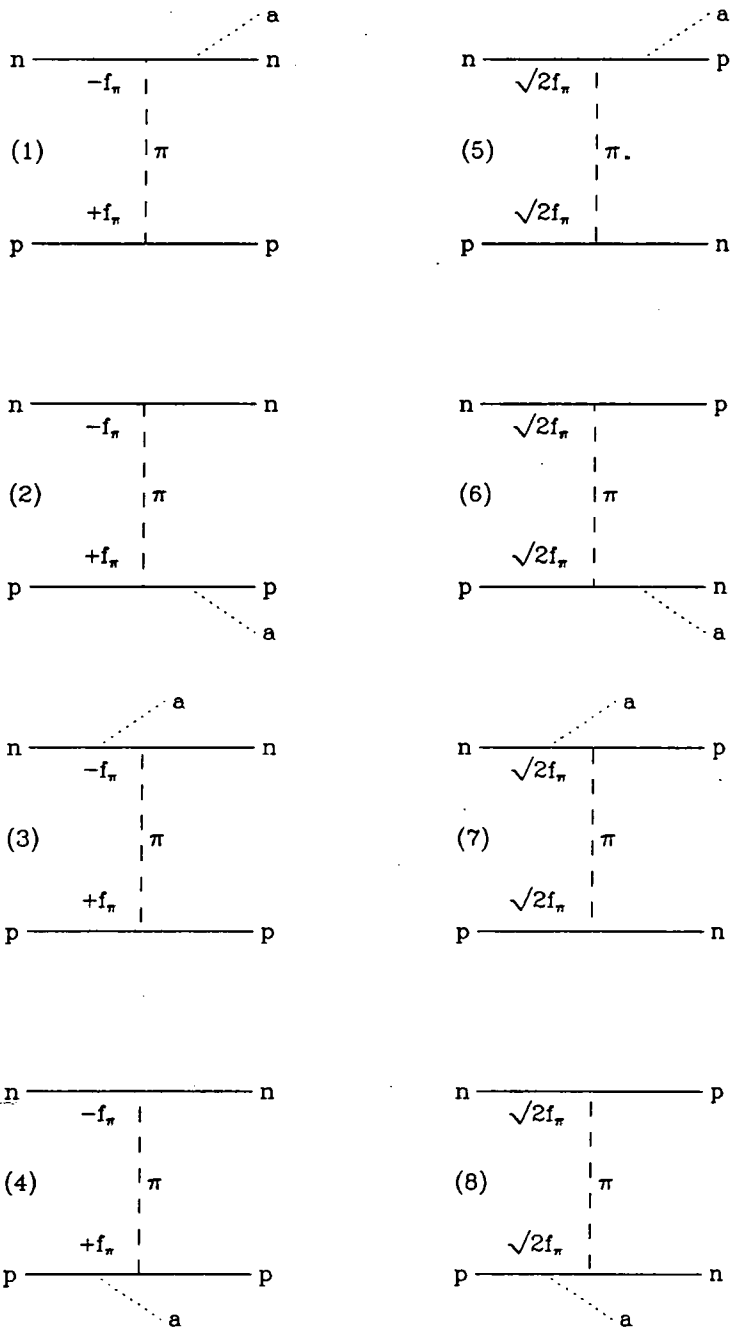
Figure 5.3 OPE $np \rightarrow npa$ Diagrams.
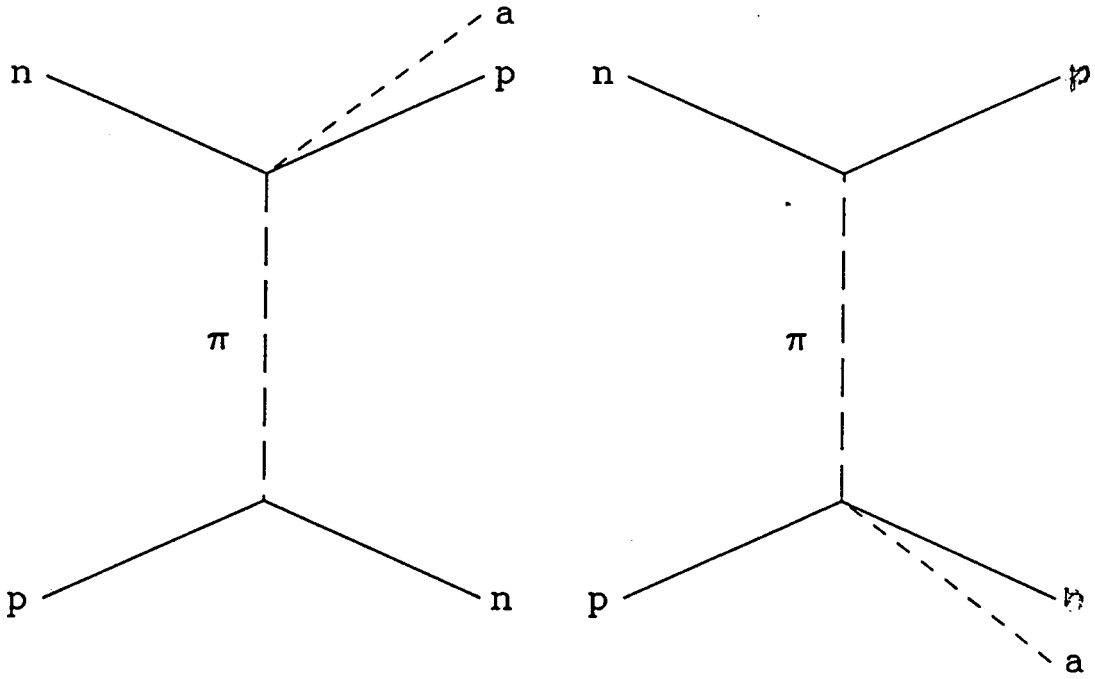
Figure 5.4 Additional OPE $np \to npa$ Diagrams.

OPE diagrams in addition to the eight in Figure 5.3. These are shown in Figure 5.4.

According to Carena and Peccei, the factor for the πnpa vertex is

$$g_{\pi npa}\not{p} = -2\sqrt{2}f_\pi^* \epsilon_{a\pi}\not{p} \tag{5.42}$$

where

$$f_\pi^* = \frac{1}{2F_\pi}, \tag{5.43}$$

$$\epsilon_{a\pi} = \frac{m_\pi}{2f_\pi}(g_{ap} - g_{an}) \tag{5.44}$$

and F_π is the pion decay constant.

These additional diagrams result from the $\pi - a$ mixing and are only present as pion exchange diagrams. In the non-relativistic limit the contribution of these diagrams is small. In Section 5.2.5 I shall present numerical results for the axion production rate in the process $np \to npa$. For simplicity I have only considered

the case for which $g_{an} = g_{ap} = g_a$ and in this case the two additional diagrams shown in Figure 5.4 are identically zero (see (5.43)). For this reason I have not included the additional diagrams in the evaluaton of the matrix element; however, their inclusion is quite straightforward.

5.2.5 Computations of the Axion Energy Emission Rate

The method described in the previous sections has been used to compute the axion emission rate, $\dot{\varepsilon}_a$, for a number of exchanged meson combinations, temperatures and values of chemical potential. The numerical integration was peformed using NAG[47] Library routines D01FCF and D01EAF. The results obtained are discussed in the following subsections. All values are accurate to within 10% and given in units of $C_1 = 16ST^{6.5}m_N^{4.5}g_a^2 f_\pi^4/m_\pi^4$. For a given temperature the axion emission rate is given as a function of $y = \hat{\mu}/T = (\mu - m_N)/T$. The significance of the variable y and the factor C_1 will become clear when we consider the approximations which have been made by other authors. Note, however, that $y \gg 1$ corresponds to the degenerate nucleon limit and $y \ll -1$ corresponds to the non-degenerate nucleon limit.

5.2.5.1 One Pion Exchange

Table 5.1 shows the computed axion emission rates for the process $nn \to nna$, or equivalently $pp \to ppa$, in the one pion exchange approximation, *i.e.* employing the matrix element corresponding to the Feynman diagrams shown in Figure 5.2. Figure 5.5 gives a plot of the values in Table 5.1. The rates are given for temperatures of $T = 20$, 50 and $80 MeV$, ($\hbar = c = k_B = 1$).

For all considered temperatures the OPE axion emission rate appears to be a monotonically increasing function of y. The gradient of the function is large and, in particular, varies from 10^{-13} to 10^{-3} while y varies from -10 to 8. Of course this means that if one wishes to compute the emission rate from a nascent neutron star one must have a good knowledge of the appropriate values of y. Over the range $T = 20 - 80 MeV$ there appears to be little temperature dependence.

Table 5.1 OPE Prediction of the Axion Energy Emission Rate per unit Volume. The values quoted are in units of

$$C_1 = 16ST^{6.5}m_N^{4.5}g_a^2 f_\pi^4/m_\pi^4.$$

$y = \frac{\hat{\mu}}{T}$	$\dot{\varepsilon}_a^{(\pi)}/C_1$ $(T = 20MeV)$	$\dot{\varepsilon}_a^{(\pi)}/C_1$ $(T = 50MeV)$	$\dot{\varepsilon}_a^{(\pi)}/C_1$ $(T = 80MeV)$
−10.	1.2×10^{-13}	1.6×10^{-13}	1.4×10^{-13}
−9.	9.1×10^{-13}	1.2×10^{-12}	1.1×10^{-12}
−8.	6.7×10^{-12}	8.8×10^{-12}	7.9×10^{-12}
−7.	4.9×10^{-11}	6.5×10^{-11}	5.8×10^{-11}
−6.	3.7×10^{-10}	4.8×10^{-10}	4.3×10^{-10}
−5.	2.7×10^{-09}	3.5×10^{-09}	3.2×10^{-09}
−4.	2.0×10^{-08}	2.6×10^{-08}	2.3×10^{-08}
−3.	1.4×10^{-07}	1.9×10^{-07}	1.7×10^{-07}
−2.	1.3×10^{-06}	1.3×10^{-06}	1.1×10^{-06}
−1.	8.1×10^{-06}	7.9×10^{-06}	7.1×10^{-06}
0.	4.1×10^{-05}	4.0×10^{-05}	3.5×10^{-05}
1.	1.5×10^{-04}	1.4×10^{-04}	1.2×10^{-04}
2.	4.2×10^{-04}	3.6×10^{-04}	3.1×10^{-04}
3.	8.4×10^{-04}	6.9×10^{-04}	5.8×10^{-04}
4.	1.3×10^{-03}	1.0×10^{-03}	8.6×10^{-04}
5.	1.9×10^{-03}	1.5×10^{-03}	1.1×10^{-03}
6.	2.5×10^{-03}	1.9×10^{-03}	1.3×10^{-03}
8.	3.2×10^{-03}	2.1×10^{-03}	1.6×10^{-03}

Figure 5.5 The OPE Prediction of the Axion Energy Emission Rate per unit volume as a function of the variable y which is defined in the text.

5.2.5.2 Full One Boson Exchange Model

Table 5.2 shows the computed axion emission rates for the process $nn \rightarrow nna$, or equivalently $pp \rightarrow ppa$, using the previously explained one boson exchange model which includes π, σ, ω, ρ, δ, ϕ and η exchanges. The rate is given for temperatures of $T = 20$, 50 and $80 MeV$. Figure 5.6 shows a plot of the values in Table 5.2 along with the OPE result for $T = 50 MeV$.

As was the case for OPE, the full OBE axion emission rate appears to be a monotonically increasing function of y and the gradient of the function is again large. There is a slightly larger variation with temperature than was the case for OPE, about a factor of 2 over the temperature range $20 - 80 MeV$.

The full OBE rate is not much different from the OPE rate which suggests that, at least for $nn \rightarrow nna$ and $pp \rightarrow ppa$, the OPE aproximation is reasonable since the other contributions almost cancel. This is not the case for the $np \rightarrow npa$ rate as we shall see in Section 5.2.5.4. The ratio of the full OBE rate to the OPE rate is greatest for higher values of y and T; for example at $y = 6$ and $T = 80 MeV$ this ratio is around 3. For lower values of y and T the ratio is less than 3.

5.2.5.3 Alternative Exchange Combinations

Table 5.3 shows the computed axion emission rates for the process $nn \rightarrow nna$, or equivalently $pp \rightarrow ppa$, using matrix elements which include:

i) π and ρ exchange diagrams and

ii) π, σ, ω and ρ exchange diagrams.

The rates are given for a temperature of $50 MeV$. Figure 5.7 shows a plot of these rates along with the OPE and full OBE rates at $T = 50 MeV$.

As was the case for OPE, these axion emission rates appear to be monotonically increasing functions of y. The gradients of the functions are again large. At a specific value of y these rates are not much different from the OPE rates or the OBE rates.

π plus ρ exchange was considered, in the non-relativistic approximation, by Ericson and Mathiot[56] who found that this rate was approximately a factor of $\frac{1}{6}$ smaller than the OPE rate. This is not confirmed by the above relativistic

Table 5.2 Full OBE Model Prediction of the Axion Emission Rate per unit volume. The values quoted are in units of

$$C_1 = 16ST^{6.5}m_N^{4.5}g_a^2 f_\pi^4/m_\pi^4.$$

$y = \frac{\tilde{\mu}}{T}$	$\dot{\varepsilon}_a^{(\pi\sigma\omega\rho\delta\phi\eta)}/C_1$ $(T = 20MeV)$	$\dot{\varepsilon}_a^{(\pi\sigma\omega\rho\delta\phi\eta)}/C_1$ $(T = 50MeV)$	$\dot{\varepsilon}_a^{(\pi\sigma\omega\rho\delta\phi\eta)}/C_1$ $(T = 80MeV)$
−10.	1.0×10^{-13}	1.4×10^{-13}	1.8×10^{-13}
−9.	7.4×10^{-13}	1.0×10^{-12}	1.3×10^{-12}
−8.	5.5×10^{-12}	7.5×10^{-12}	9.6×10^{-12}
−7.	4.0×10^{-11}	5.5×10^{-11}	7.2×10^{-11}
−6.	3.0×10^{-10}	4.1×10^{-10}	5.2×10^{-10}
−5.	2.2×10^{-09}	3.0×10^{-09}	3.8×10^{-09}
−4.	1.6×10^{-08}	2.2×10^{-08}	2.8×10^{-08}
−3.	1.2×10^{-07}	1.6×10^{-07}	2.0×10^{-07}
−2.	8.0×10^{-07}	1.1×10^{-06}	1.4×10^{-06}
−1.	5.0×10^{-06}	6.9×10^{-06}	8.7×10^{-06}
0.	2.5×10^{-05}	3.6×10^{-05}	4.3×10^{-05}
1.	9.6×10^{-05}	1.4×10^{-04}	1.7×10^{-04}
2.	2.4×10^{-04}	3.9×10^{-04}	4.7×10^{-04}
3.	5.4×10^{-04}	8.1×10^{-04}	9.9×10^{-04}
4.	9.1×10^{-04}	1.4×10^{-03}	1.8×10^{-03}
5.	1.4×10^{-03}	2.1×10^{-03}	2.7×10^{-03}
6.	1.9×10^{-03}	2.9×10^{-03}	3.8×10^{-03}
8.	2.9×10^{-03}	4.6×10^{-03}	6.2×10^{-03}
10.	−	6.3×10^{-03}	−
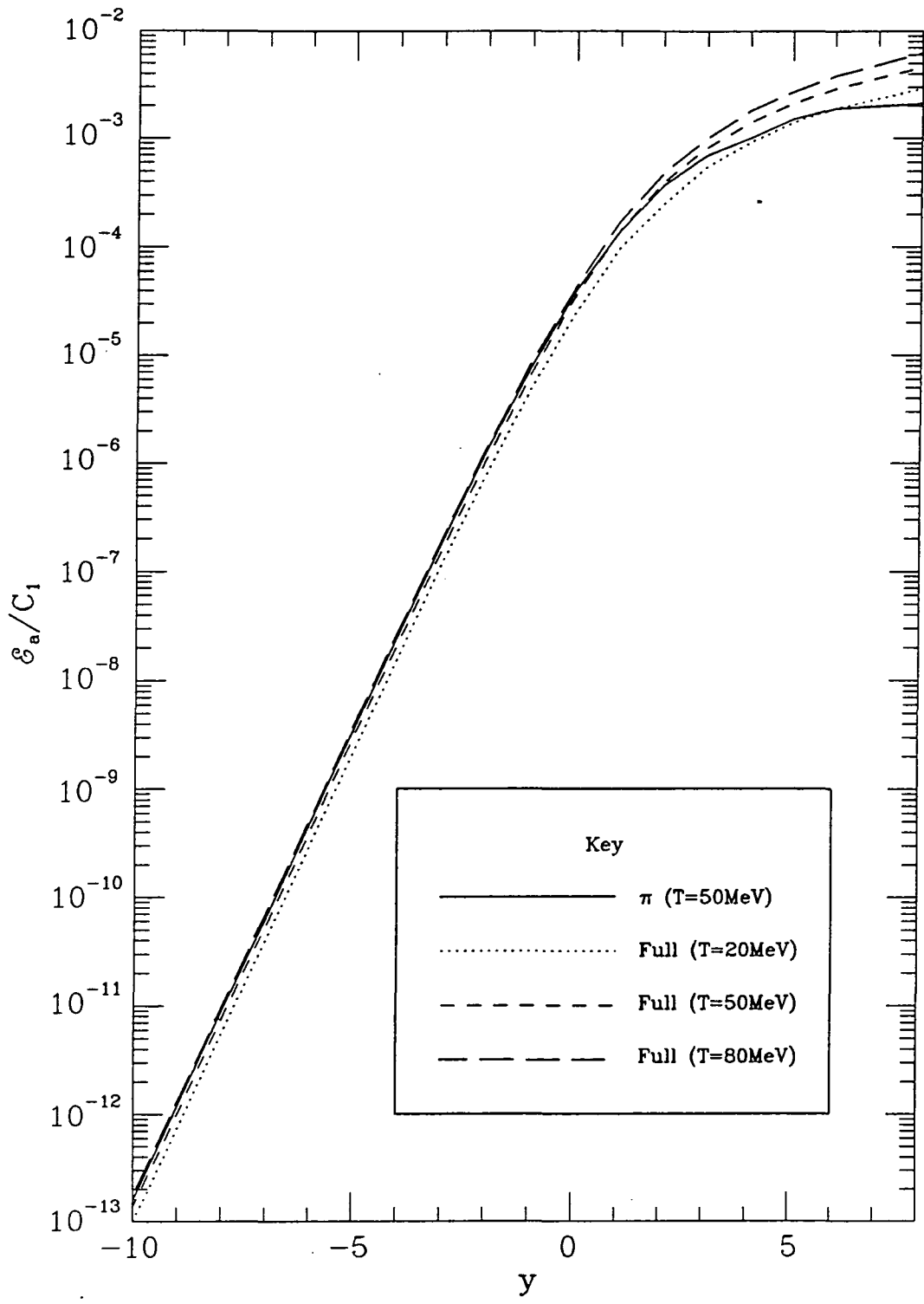
Figure 5.6   The Full OBE Model Prediction of the Axion Energy
Emission Rate per unit volume as a function of the variable y which is
defined in the text.

Table 5.3 π, ρ and $\pi, \sigma, \omega, \rho$-exchange Prediction of the Axion Energy Emission Rate per unit volume. The values quoted are in units of $C_1 = 16ST^{6.5}m_N^{4.5}g_a^2 f_\pi^4/m_\pi^4$.

$y = \frac{\hat{\mu}}{T}$	$\dot{\varepsilon}_a^{(\pi\rho)}/C_1$	$\dot{\varepsilon}_a^{(\pi\sigma\omega\rho)}/C_1$
−10.	1.1×10^{-13}	1.1×10^{-13}
−9.	8.1×10^{-13}	8.4×10^{-13}
−8.	6.0×10^{-12}	6.2×10^{-12}
−7.	4.4×10^{-11}	4.6×10^{-11}
−6.	3.3×10^{-10}	3.4×10^{-10}
−5.	2.4×10^{-9}	2.5×10^{-9}
−4.	1.8×10^{-8}	1.8×10^{-8}
−3.	1.3×10^{-7}	1.3×10^{-7}
−2.	8.6×10^{-7}	9.4×10^{-7}
−1.	5.4×10^{-6}	5.9×10^{-6}
0.	2.6×10^{-5}	2.9×10^{-5}
1.	1.0×10^{-4}	1.1×10^{-4}
2.	2.7×10^{-4}	3.2×10^{-4}
3.	5.6×10^{-4}	6.9×10^{-4}
4.	9.4×10^{-4}	1.2×10^{-3}
5.	1.4×10^{-3}	1.8×10^{-3}
6.	2.0×10^{-3}	2.7×10^{-3}
8.	−	4.0×10^{-3}

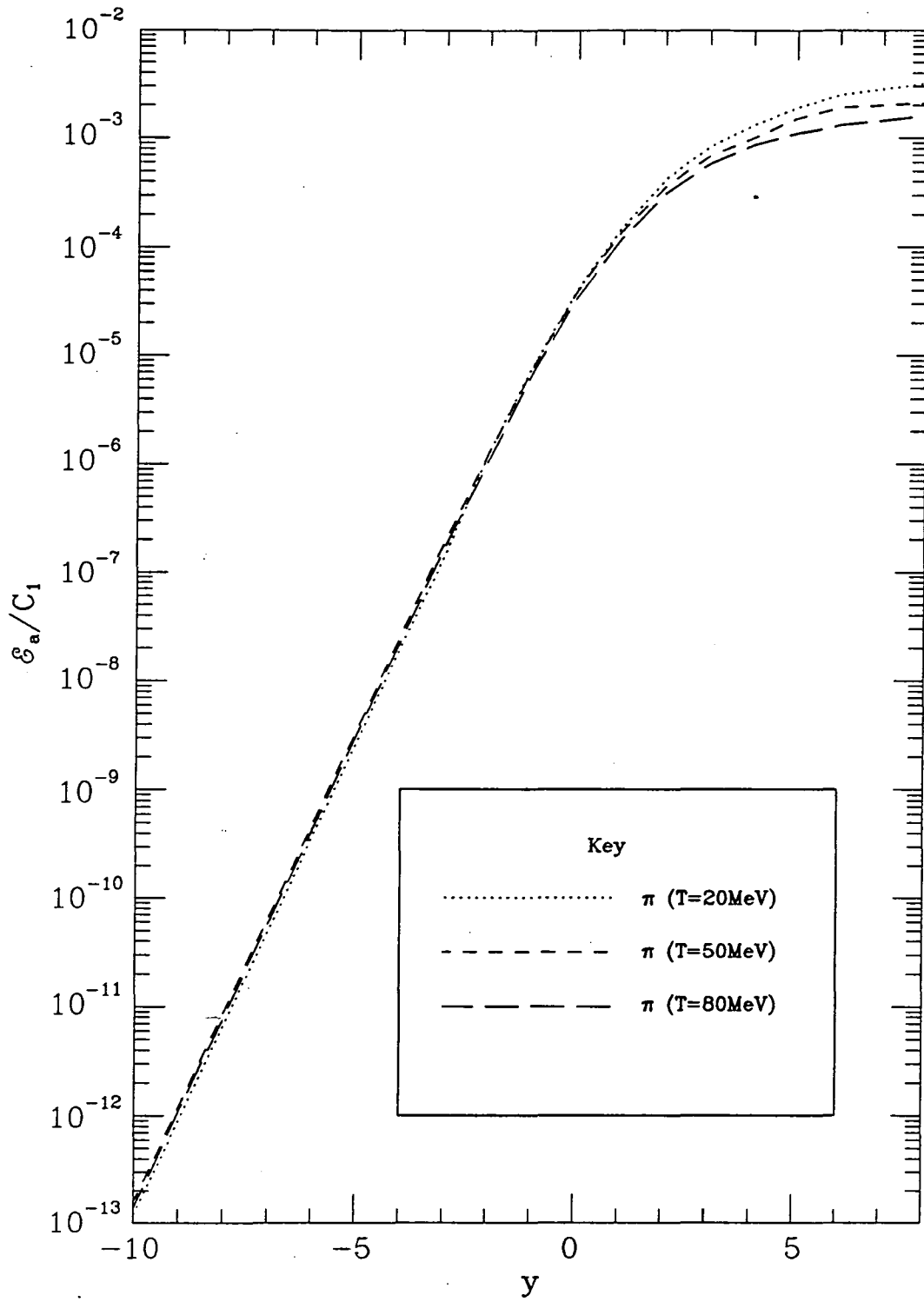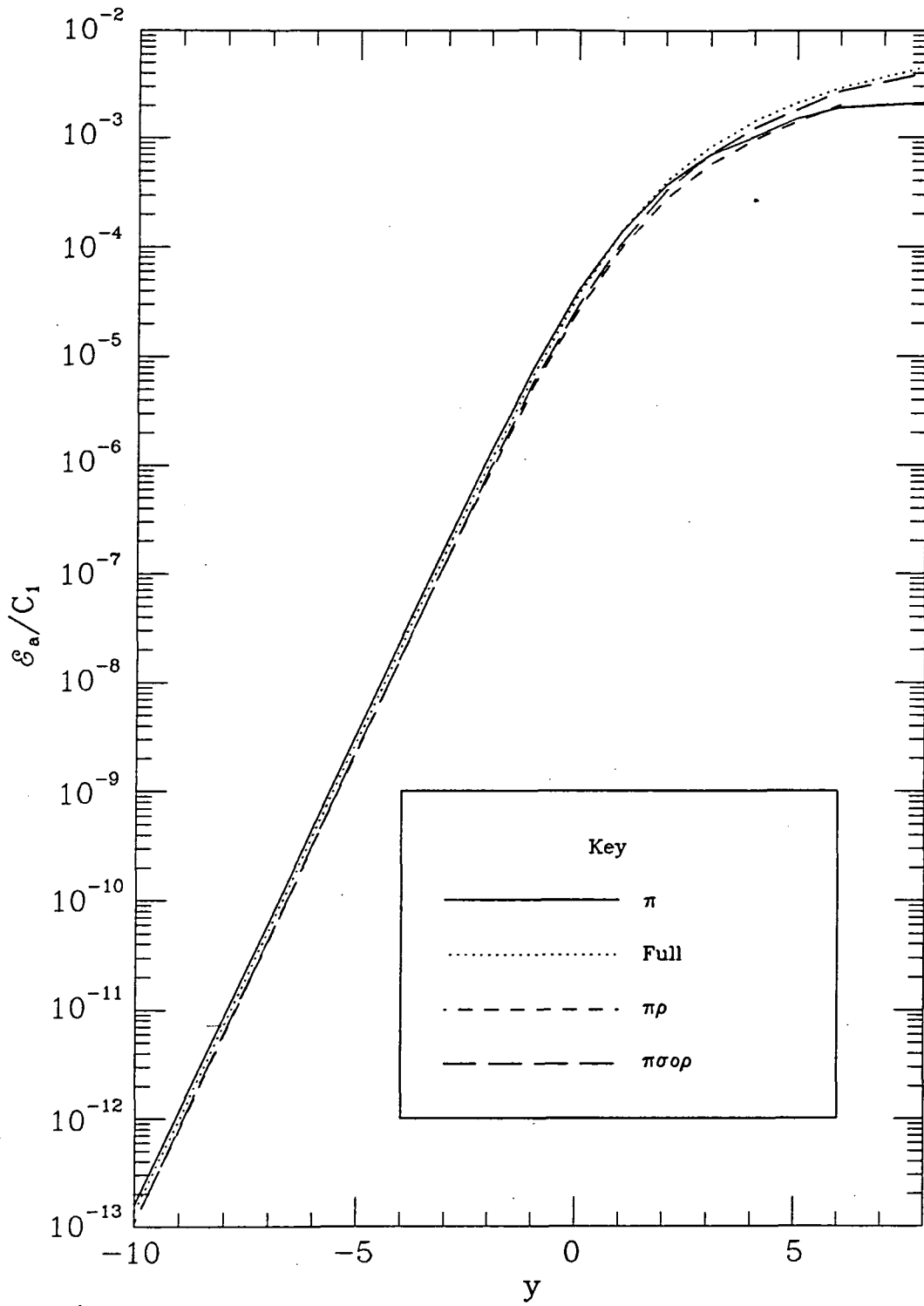**Figure 5.7**   The π, ρ and $\pi, \sigma, \omega, \rho$-exchange Prediction of the Axion Energy Emission Rate per unit volume as a function of the variable y which is defined in the text.

treatment which gives at most a factor of $\frac{1}{2}$. This calls into question either the non-relativistic approximation or Ericson and Mathiot's form for the $\pi + \rho$ exchange matrix element. We shall see in later sections that the non-relativistic approximation is reasonable which implies that the difference between Ericson and Mathiot's result and the above result can be traced to the matrix elements used. Figure 5.8 shows two corresponding π and ρ-exchange diagrams. If we just consider the matrix element, $\mathcal{M}_{\pi\rho}^{(2)}$, for these two diagrams then

$$\sum_{spins} |\mathcal{M}_{\pi\rho}^{(2)}|^2 = \sum_{spins} |\mathcal{M}_{\pi}^{(1)} + \mathcal{M}_{\rho}^{(1)}|^2$$

$$= \sum_{spins} \{|\mathcal{M}_{\pi}^{(1)}|^2 + |\mathcal{M}_{\rho}^{(1)}|^2 + \mathcal{M}_{\pi}^{(1)*}\mathcal{M}_{\rho}^{(1)} + \mathcal{M}_{\rho}^{(1)*}\mathcal{M}_{\pi}^{(1)}\}.$$

Since π has a pseudovector coupling and ρ has a vector coupling to neutrons,

$$\mathcal{M}_{\pi}^{(1)*}\mathcal{M}_{\rho}^{(1)} = \mathcal{M}_{\rho}^{(1)*}\mathcal{M}_{\pi}^{(1)} \equiv 0.$$

However in Ericson and Mathiot's work[56],

$$\mathcal{M}_{\pi}^{(1)*}\mathcal{M}_{\rho}^{(1)} = \mathcal{M}_{\rho}^{(1)*}\mathcal{M}_{\pi}^{(1)} \neq 0,$$

and is thus incorrect.

The $\pi + \sigma + \omega + \rho$ exchange combination was treated because these are the particles with the largest coupling constants (see Section 4.2.3). It seems that these contributions cancel in calculating the axion emission rate.

5.2.5.4 The Process $np \to npa$

Tables 5.4 and 5.5 show the computed axion emission rates for the process $np \to npa$ using matrix elements which include the OPE diagrams and all considered meson exchange diagrams respectively. The rates are given as functions of $\bar{y} \equiv (y_n + y_p)/2$ and $\Delta y \equiv |y_n - y_p|/2$ and for a temperature of $50MeV$. Note that as well as being a monotonically increasing function of $\bar{y}$ both emission rates are monotonically decreasing functions of Δy. Also recall that $S = 1$ for the np case as opposed to $S = 1/4$ for the pp or nn rates so that the np rates have an additional factor of 4 over and above any factor indicated in Tables 5.4 and 5.5
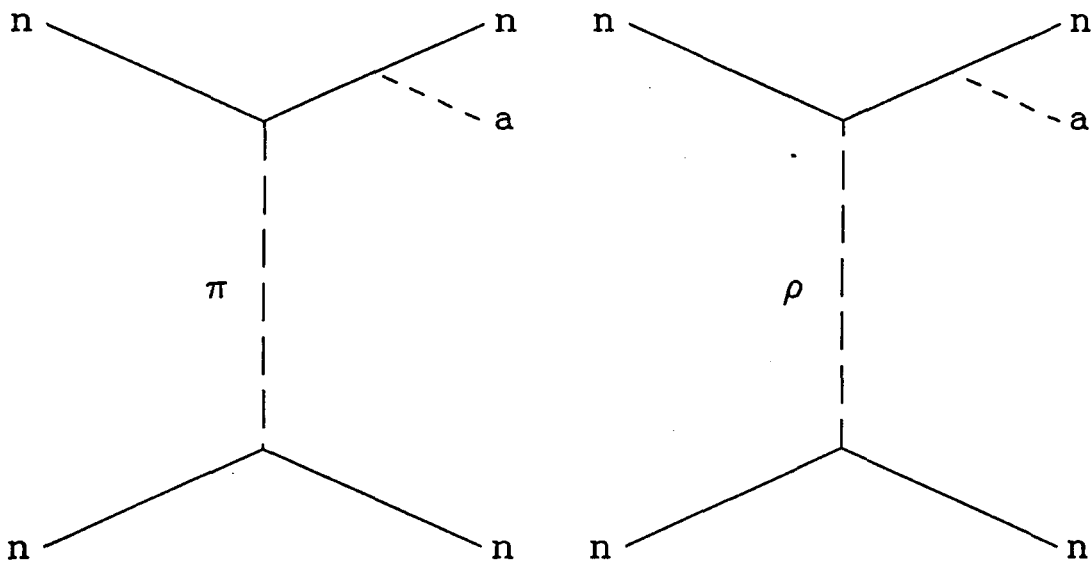
Figure 5.8 π and ρ Exchange Axion Bremsstrahlung Diagrams.

when compared to the pp or nn rates. We can see that for the np process the OBE rates are as much as a factor of $\frac{1}{3}$ smaller that the OPE rates.

5.2.5.5 Density Dependence

In the extreme conditions of a nascent neutron star, masses and coupling constants can be functions of temperature, pressure and density. The effective nucleon mass m_N^* could be around $0.5m_N$[5,21] which brings into question the non-relativistic approximations which have been used by previous authors since Fermi momenta of $\sim 400MeV$ are possible. As an initial examination I have computed the axion emission rate with $m_N^* = 0.5m_N$. For the purposes of this initial exploration I have kept all other quantities, the coupling constants and masses, at their vacuum values. Since I have employed the pseudovector coupling for the axion,the pion and the eta particles it is the pseudovector coupling constants

105

Table 5.4 OPE Prediction of the Axion Energy Emission Rate per unit volume for $np \rightarrow npa$ at $T = 50MeV$. The values quoted are in units of $C_1 = 16ST^{6.5}m_N^{4.5}g_a^2 f_\pi^4/m_\pi^4$.

$\bar{y}$	$\Delta y = 0$	$\Delta y = 2$	$\Delta y = 4$	$\Delta y = 6$	$\Delta y = 8$	$\Delta y = 10$
-10	5.1×10^{-13}	5.1×10^{-13}	5.1×10^{-13}	5.0×10^{-13}	4.7×10^{-13}	3.4×10^{-13}
-8	2.8×10^{-11}	2.8×10^{-11}	2.7×10^{-11}	2.6×10^{-11}	1.9×10^{-11}	6.0×10^{-12}
-6	1.5×10^{-9}	1.5×10^{-9}	1.4×10^{-9}	1.0×10^{-9}	3.3×10^{-10}	7.3×10^{-11}
-4	8.1×10^{-8}	7.7×10^{-8}	5.6×10^{-8}	1.8×10^{-8}	3.9×10^{-9}	5.6×10^{-10}
-2	4.1×10^{-6}	3.0×10^{-6}	1.1×10^{-6}	2.2×10^{-7}	3.1×10^{-8}	3.7×10^{-9}
0	1.2×10^{-4}	6.0×10^{-5}	1.2×10^{-5}	1.7×10^{-6}	2.0×10^{-7}	2.4×10^{-8}
2	9.0×10^{-4}	4.5×10^{-4}	8.8×10^{-5}	1.1×10^{-5}	1.3×10^{-6}	1.5×10^{-7}
4	2.2×10^{-3}	1.4×10^{-3}	4.4×10^{-4}	6.3×10^{-5}	8.4×10^{-6}	1.0×10^{-6}
6	3.2×10^{-3}	2.4×10^{-3}	1.2×10^{-3}	3.3×10^{-4}	5.4×10^{-5}	7.0×10^{-6}
8	3.7×10^{-3}	3.1×10^{-3}	1.9×10^{-3}	8.7×10^{-4}	2.5×10^{-4}	4.2×10^{-5}

Table 5.5 Full OBE Model Prediction of the Axion Energy Emission Rate per unit volume for $np \rightarrow npa$ at $T = 50MeV$. The values quoted are in units of $C_1 = 16ST^{6.5}m_N^{4.5}g_a^2 f_\pi^4/m_\pi^4$.

$\bar{y}$	$\Delta y = 0$	$\Delta y = 2$	$\Delta y = 4$	$\Delta y = 6$	$\Delta y = 8$	$\Delta y = 10$
-10	1.9×10^{-13}	1.9×10^{-13}	1.9×10^{-13}	1.9×10^{-13}	1.8×10^{-13}	1.3×10^{-13}
-8	1.0×10^{-11}	1.0×10^{-11}	1.0×10^{-11}	9.6×10^{-12}	6.9×10^{-12}	2.6×10^{-12}
-6	5.6×10^{-10}	5.5×10^{-10}	5.2×10^{-10}	3.8×10^{-10}	1.4×10^{-10}	2.8×10^{-11}
-4	3.0×10^{-8}	2.8×10^{-8}	2.0×10^{-8}	7.8×10^{-9}	1.5×10^{-9}	2.4×10^{-10}
-2	1.5×10^{-6}	1.1×10^{-6}	4.1×10^{-7}	8.3×10^{-8}	1.3×10^{-8}	1.8×10^{-9}
0	4.2×10^{-5}	2.1×10^{-5}	4.5×10^{-6}	7.3×10^{-7}	9.5×10^{-8}	1.3×10^{-8}
2	3.6×10^{-4}	1.9×10^{-4}	3.8×10^{-5}	5.2×10^{-6}	7.0×10^{-7}	7.1×10^{-8}
4	1.2×10^{-3}	7.4×10^{-4}	2.1×10^{-4}	3.6×10^{-5}	5.1×10^{-6}	7.2×10^{-7}
6	2.4×10^{-3}	1.8×10^{-3}	7.7×10^{-4}	2.2×10^{-4}	3.7×10^{-5}	5.5×10^{-6}
8	4.1×10^{-3}	3.2×10^{-3}	1.7×10^{-3}	8.4×10^{-4}	2.2×10^{-4}	4.1×10^{-5}

Table 5.6 Predictions of the Axion Energy Emission Rate per unit volume with $m_N^* = 0.5m_N$ and at T=50MeV). The values quoted are in units of $C_1 = 16ST^{6.5}m_N^{4.5}g_a^2 f_\pi^4/m_\pi^4$.

$y = \frac{\hat{\mu}}{T}$	$\dot{\varepsilon}_a^{(\pi)}(m_N^* = 0.5m_N)/C_1$	$\dot{\varepsilon}_a^{(\pi\sigma\omega\rho\delta\phi\eta)}(m_N^* = 0.5m_N)/C_1$
-10	6.5×10^{-15}	2.1×10^{-14}
-8	3.5×10^{-13}	1.2×10^{-12}
-6	1.9×10^{-11}	6.3×10^{-11}
-4	1.0×10^{-9}	3.4×10^{-9}
-2	6.5×10^{-8}	1.7×10^{-7}
0	2.1×10^{-6}	6.0×10^{-6}
2	2.1×10^{-5}	7.7×10^{-5}
4	6.7×10^{-5}	3.3×10^{-4}
6	1.2×10^{-4}	7.6×10^{-4}
8	1.6×10^{-4}	1.2×10^{-3}

that I have kept at their vacuum values.

Table 5.6 shows the computed axion emission rates for the process $nn \to nna$, or equivalently $pp \to ppa$, using matrix elements which include:

i) OPE diagrams alone and

ii) all considered OBE diagrams.

The rates are given as a function of y and for a temperature of $50MeV$ with a dividing factor of C_1 (N.B. m_N in C_1 is the vacuum value). This factor allows a point by point comparison with the previous OPE and OBE emission rates which were calculated using the vacuum nucleon mass. The values in Table 5.6 are plotted in Figure 5.9 along with the corresponding curves(from Sections 5.2.5.1-2) which employed the vacuum nucleon mass. For the OPE case one can see that the rates which had $m_N^* = 0.5m_N$ are a factor of ($\sim \frac{1}{15} - \frac{1}{20}$) smaller than the rates which employed the vacuum nucleon mass. The effect is not as dramatic for the full OBE matrix element although there is still a factor of around $\frac{1}{5}$. Although one must remember that these results do not take into account the density dependence of any of the other "constants" which appear in the matrix elements, and so can

107
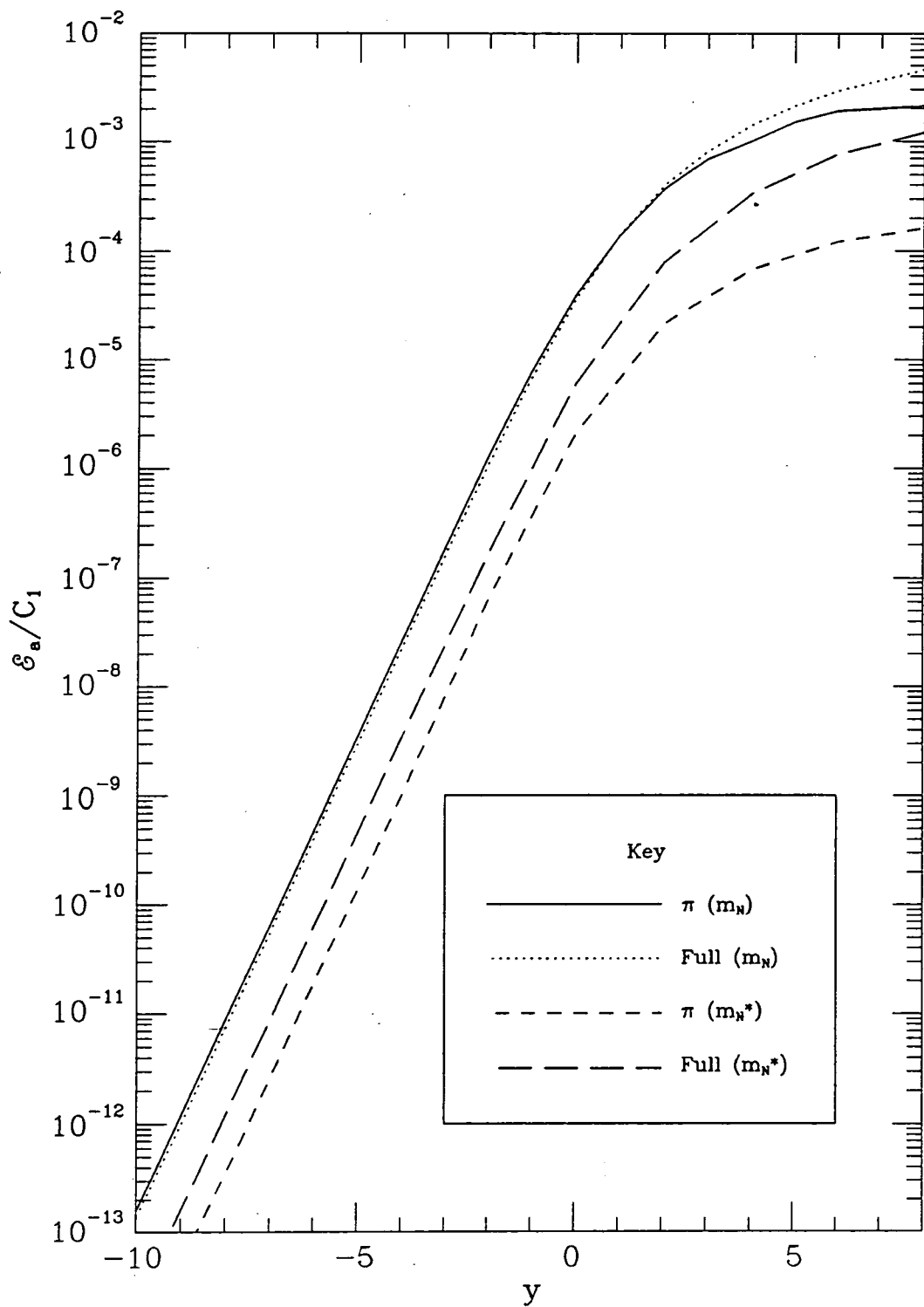
Figure 5.9   The Predictions of Axion Emission Rate per unit volume for the Full OBE model and the OPE model at reduced masses of m_N and $m_N^* = 0.5m_N$.

not in any way be considered as complete, they do give an indication of the order of magintude of the changes which may occur.

5.3 Approximate Evaluation of the Axion Energy Emission Rate

In this section I shall examine the various approximations, kinematical and otherwise, which have been made in the literature in calculating the axion energy emission rate from a nascent neutron star. The first two subsections will discuss the approximations made in the evaluation of the phase space and the matrix element respectively. The third will outline the results which have been obtained and discuss the errors introduced as compared to the relativistic evaluations of Section 5.2. The fourth will outline the possible changes which the relativistic results would make to limits on the axion decay constant and mass which have been derived using non-relativistic approximations.

5.3.1 Phase Space Integrals and Fermi-Dirac Functions[42]

In calculating the axion energy production rate one integrates over dP_F where

$$dP_F = dQ_2 dQ_3 F_a F_b (1 - F_c)(1 - F_d), \tag{5.45}$$

and the F_i and the dQ_i were defined in Section 5.1. For $T \ll m_N$ it is sufficient to employ non-relativistic (NR) kinematics[42]. In this case $E_i \simeq m_N + p_i^2/(2m_N)$ and one can define the dimensionless quantities $y_i = \hat{\mu}_i$ and $u_i = p_i^2/(2m_N T)$ where $\hat{\mu}_i = \mu_i - m_N$ is the NR chemical potential. With these definitions,

$$F_i = F(E_i, \mu_i) \simeq f_i = \frac{1}{e^{u_i - y_i} + 1}. \tag{5.46}$$

The evaluations of dQ_3 is most straightforward in the centre of mass (c.o.m.) frame. One can define the centre of mass momentum as $\vec{p}_+ \equiv (\vec{p}_a + \vec{p}_b)/2$ and the relative momentum as $\vec{p}_- \equiv (\vec{p}_a - \vec{p}_b)/2$. The momenta of nucleons c and d in the c.o.m. frame are found by using a Galilean transformation,

$$\vec{p}_c\,' = \vec{p}_c - \vec{p}_+ \tag{5.47}$$

and

$$\vec{p}_d\,' = \vec{p}_d - \vec{p}_+, \tag{5.48}$$

where the prime denotes the c.o.m. frame. In the non-relativistic limit the final state nucleons will, on average, carry essentially all of the final state momentum. Neglecting the axion momentum one can see that

$$\vec{p}_c{}' = -\vec{p}_d{}'$$.

from momentum conservation. The axion energy in the star fixed frame is given by

$$
\begin{aligned}
E_e &= E_a + E_b - E_c - E_d \\
&= \frac{\vec{p}_a^2}{2m_N} + \frac{\vec{p}_b^2}{2m_N} - \frac{\vec{p}_c^2}{2m_N} - \frac{\vec{p}_d^2}{2m_N} \\
&= \frac{\vec{p}_-^2}{m_N} - \frac{\vec{p}_+^2}{m_N}
\end{aligned}
\tag{5.49}
$$

With the above definitions

$$dQ_2 = 8\frac{d^3p_+}{(2\pi)^3 2m_N}\frac{d^3p_-}{(2\pi)^3 2m_N}, \tag{5.50}$$

where E_a and E_b in the denominators of the phase space factors (5.2) have been approximated by m_N. Also

$$dQ_3 = (2\pi)^4 \frac{d^3p_c'}{(2\pi)^3 2m_N}\frac{E_e d\Omega_e}{(2\pi)^6 4m_N}, \tag{5.51}$$

where the δ function in the definition of dQ_3 (5.3) has been integrated over.

In the next subsection we shall see that $\sum_{spins}|\mathcal{M}|^2$ only depends on p_+, p_c' and γ_c' , in the non-relativistic limit, so we can integrate over the other variables to give

$$dP_F = \frac{16 E_e f_T}{(2\pi)^7 (2m_N)^4} p_+^2 dp_+ p_-^2 dp_- p_c'^2 dp_c' d\gamma_c' d\gamma_-, \tag{5.52}$$

where γ_c' and γ_- are the cosines of the angles of $\vec{p}_c'$ and $\vec{p}_-$ with respect to $\hat{p}_+$ and $f_T = f_a f_b(1 - f_c)(1 - f_d)$, or, in terms of dimensionless variables[57],

$$dP_F = \frac{f_T T^{5.5} m_N^{0.5}}{2^{4.5}\pi^7}(u_+ u_- u_c')^{\frac{1}{2}}(u_- - u_c')du_+ du_- du_c' d\gamma_- d\gamma_c', \tag{5.53}$$

where

$$u_{a,b} = u_+ + u_- \pm 2(u_+ u_-)^{\frac{1}{2}}\gamma_-, \tag{5.54}$$

$$u_{c,d} = u'_c + u_- \pm 2(u'_c + u_+)^{\frac{1}{2}}\gamma'_c, \tag{5.55}$$

$$\gamma_- = \hat{p}_+ \cdot \hat{p}_- \tag{5.56}$$

and

$$\gamma'_c = \hat{p}_+ \cdot \hat{p}'_c. \tag{5.57}$$

5.3.2 The One Pion Exchange Matrix Element

In order to calculate the axion energy emission rate via nucleon-nucleon-axion bremsstrahlung one needs to know $\sum_{spins} |\mathcal{M}|^2$ as a function of the momenta of the relevant particles. There is, of course, no direct experimental measurement of the $NN \to NNa$ cross-section which can be employed and so one has to calculate the $NN \to NNa$ matrix element by using some theoretical model. As we have already discussed, as a first approximation one can treat the $NN \to NNa$ matrix element in the one pion exchange approximation. This entails evaluating $\sum_{spins} |\mathcal{M}|^2$ from the eight Feynman diagrams shown in Figure 5.2, with $\alpha = \pi$. This OPE approximation is employed almost exclusively in the literature. All the reported work on OPE NNa bremsstrahlung has employed the non-relativistic limit of $\sum_{spins} |\mathcal{M}|^2$ as computed from the eight diagrams in Figure 5.2.

5.3.2.1 Iwamoto's OPE Matrix Element

Iwamoto[31] was the first to calculate $\sum_{spins} |\mathcal{M}|^2$ for $NN \to NNa$ in the OPE approximation. He found that for the neutron-neutron process, $nn \to nna$,

$$
\begin{aligned}
\sum_{spins} |\mathcal{M}|^2 = &\frac{256}{3}(2m_N g_{an})^2 \frac{f_\pi^4}{m_\pi^4} m_N^2 \\
&\left[\frac{p_k^4}{(p_k^2 + m_\pi^2)^2} + \frac{p_l^4}{(p_l^2 + m_\pi^2)^2} + \frac{p_k^2 p_l^2}{(p_k^2 + m_\pi^2)(p_l^2 + m_\pi^2)} \right],
\end{aligned}
\tag{5.58}
$$

where $p_k = |\vec{p}_k|$ and $p_l = |\vec{p}_l|$ are the moduli of the three momentum transfers, $\vec{p}_k = \vec{p}_d - \vec{p}_b$ and $\vec{p}_l = \vec{p}_c - \vec{p}_b$. Iwamoto only computed the matrix element for the process $nn \to nna$ as he was concerned with axion production in a neutron star. In a stable, cooled neutron star there are very few protons. This is not the case in a newly-born, hot neutron star in which proton reactions must also be considered.

Brinkmann and Turner[42] have calculated a modified version of Iwamoto's matrix element. They found that for $nn \to nna$

$$\sum_{spins} |\mathcal{M}|^2 = \frac{256}{3} (2m_N g_{an})^2 \frac{f_\pi^4}{m_\pi^4} m_N^2$$

$$\times \left[\frac{p_k^4}{(p_k^2 + m_\pi^2)^2} + \frac{p_l^4}{(p_l^2 + m_\pi^2)^2} + (1 - \beta) \frac{p_k^2 p_l^2}{(p_k^2 + m_\pi^2)(p_l^2 + m_\pi^2)} \right],$$

$$(5.59)$$

where β depends on the degree of degeneracy of the neutrons (see Brinkmann and Turner[42]). In the degenerate neutron limit $\beta = 0$ and in the non-degenerate neutron limit $\beta = 1.0845$. Brinkmann and Turner have also calculated $\sum_{spins} |\mathcal{M}|^2$ for the pp and np processes. For the pp process one simply replaces g_{an} by g_{ap} in equation (5.59). For the np process they find that

$$\sum_{spins} |\mathcal{M}|^2 = \frac{256}{3} (2m_N)^2 \frac{f_\pi^4}{m_\pi^4} m_N^2 \frac{(g_{an} + g_{ap})^2}{4}$$

$$\times \left[\frac{p_l^4}{(p_l^2 + m_\pi^2)^2} - \frac{4\beta}{3} \frac{p_k^2 p_l^2}{(p_k^2 + m_\pi^2)(p_l^2 + m_\pi^2)} \right]$$

$$+ \frac{256}{3} (2m_N)^2 \frac{f_\pi^4}{m_\pi^4} m_N^2 \frac{(g_{an}^2 + g_{ap}^2)}{2}$$

$$\times \left[\frac{p_k^4}{(p_k^2 + m_\pi^2)^2} + \frac{2p_l^4}{(p_l^2 + m_\pi^2)^2} + \frac{2(3 - \beta)}{3} \frac{p_k^2 p_l^2}{(p_k^2 + m_\pi^2)(p_l^2 + m_\pi^2)} \right],$$

$$(5.60)$$

However, in their calculation they have treated isospin incorrectly (see Section 5.2.4.2). To correct the above expression one must introduce an additional minus sign in front of the terms which are proportional to $p_k^2 p_l^2$, thus giving

$$\sum_{spins} |\mathcal{M}|^2 = \frac{256}{3} (2m_N)^2 \frac{f_\pi^4}{m_\pi^4} m_N^2 \frac{(g_{an} + g_{ap})^2}{4}$$

$$\times \left[\frac{p_l^4}{(p_l^2 + m_\pi^2)^2} + \frac{4\beta}{3} \frac{p_k^2 p_l^2}{(p_k^2 + m_\pi^2)(p_l^2 + m_\pi^2)} \right]$$

$$+ \frac{256}{3} (2m_N)^2 \frac{f_\pi^4}{m_\pi^4} m_N^2 \frac{(g_{an}^2 + g_{ap}^2)}{2}$$

$$\times \left[\frac{p_k^4}{(p_k^2 + m_\pi^2)^2} + \frac{2p_l^4}{(p_l^2 + m_\pi^2)^2} - \frac{2(3 - \beta)}{3} \frac{p_k^2 p_l^2}{(p_k^2 + m_\pi^2)(p_l^2 + m_\pi^2)} \right].$$

$$(5.61)$$

5.3.2.2 The Constant Matrix Element Approximation

Almost all of the reported work on axion production in the nascent neutron star has employed an additional approximation as regards $\sum_{spins} |\mathcal{M}|^2$. According to Brinkmann and Turner[42] $p_k^2 \sim 3m_N T$, and thus for the temperatures appropriate to the nascent neutron star (*i.e.* $10 - 80 MeV$), $p_k^2 \gg m_\pi^2$. If we employ this approximation, Brinkmann and Turner's adjusted version of Iwamoto's matrix element, equation (5.59), becomes

$$\sum_{spins} |\mathcal{M}|^2 = \frac{256}{3}(2m_N g_{an})^2 \frac{f_\pi^4}{m_\pi^4} m_N^2 (3 - \beta), \qquad (5.62)$$

which is a constant. Using this constant matrix element greatly simplifies the calculation of axion emission rate. Despite the introduction of β, Brinkmann and Turner effectively use $\beta = 0$ for all their computations of axion emission rate, *i.e.* for the *nn* process they use

$$\sum_{spins} |\mathcal{M}|^2 = 256(2m_N g_{an})^2 \frac{f_\pi^4}{m_\pi^4} m_N^2. \qquad (5.63)$$

This is equivalent to redefining $g_{an} = \sqrt{(3 - \beta)g_{an}^2/3}$.

Some reservations about using this approximation have been expressed[56]. On the face of things it does seem a rather odd approximation, since combined with the non-relativistic approximation we are effectively saying that

$$m_\pi \ll p_k \ll m_n. \qquad (5.64)$$

There is only a very narrow range of p_k in which both of these conditions will be satisfied.

There is no doubt that the constant matrix element approximation allows great simplifications in the calculation of the axion emission rate; however, it may well be an oversimplification. I shall examine this question in more detail in Section 5.3.3.

5.3.3 Reported Calculations of the Axion Emission Rate

Various authors have derived limits on axion parameters by considering axion emission from supernovae (see Section 3.6). All but one of these use the OPE

constant matrix element approximation in order to calculate the axion energy emission rate. An exception is the paper by Ericson and Mathiot who consider the full momentum dependence of the non-relativistic OPE approximation and also include the ρ-exchange contribution to the production process.

The most comprehensive study of axion emission rate (to date) is that of Brinkmann and Turner. In this section I shall mainly concentrate on their work.

5.3.4 The Non-Degenerate Nucleon Limit[42]

In the non-relativistic limit we can combine equation (5.53), the NR expression for dP_F, with $E_e S \sum_{spins} |\mathcal{M}|^2$ to give

$$
\dot{\varepsilon}_a = \frac{ST^{6.5}m_N^{0.5}}{2^{3.5}\pi^7} \int_0^\infty du_+ \int_0^\infty du_- \int_0^{u_-} du_c' \int_{-1}^1 d\gamma_- \int_{-1}^1 d\gamma_c'
$$
$$
\times \sum_{spins} |\mathcal{M}|^2 \sqrt{u_+ u_- u_c'}(u_- - u_c')^2 f_T. \tag{5.65}
$$

If we employ the constant matrix element approximation $\sum_{spins}|\mathcal{M}|^2$ can be taken out of the integral. In this case it is clear that $\dot{\varepsilon}_a$ is proportional to $T^{6.5}$ times a function of y only.

In the non-degenerate (ND) limit for the nucleons $(y_i \ll -1)$, $\exp(u_i - y_-)$ is very small and this implies that

$$
(1 - f_i) \simeq 1 \tag{5.66}
$$

and

$$
f_i \simeq e^{(y_i - u_i)}, \tag{5.67}
$$

thus giving

$$
\dot{\varepsilon}_a^{(ND)} = \frac{ST^{6.5}m_N^{0.5}}{2^{3.5}\pi^7} e^{(y_a + y_b)} \int_0^\infty du_+ \int_0^\infty du_- \int_0^{u_-} du_c'
$$
$$
\times 4\sqrt{u_+ u_- u_c'}(u_- - u_c')^2 e^{-2(u_+ - u_-)}, \tag{5.68}
$$

where the γ_- and γ_c' integrations have been done. On performing the other inte-

grations one obtains

$$\dot{\varepsilon}_a^{(ND)} = \frac{S \sum_{spins} |\mathcal{M}|^2 T^{6.5} m_N^{0.5} e^{y_a + y_b}}{140\pi^{6.5}}. \tag{5.69}$$

If we take the nn process we can substitute

$$S \sum_{spins} |\mathcal{M}|^2 = 64(2m_N)^2 \frac{f_\pi^4 m_N^2}{m_\pi^4} \tag{5.70}$$

from equation (5.63) to give, with $y_a = y_b = y$,

$$\dot{\varepsilon}_a^{(ND)} = \frac{64 T^{6.5} m_N^{4.5} e^{2y} g_{an}^2 f_\pi^4}{35\pi^{6.5} m_\pi^4}, \tag{5.71}$$

which is equivalent to the results for the ND limit as given in reference [42]. $(\dot{\varepsilon}_a^{(ND)}/C_1 = \dot{\varepsilon}_a^{(ND)} m_\pi^4/(4T^{6.5} m_N^{4.5} g_{an}^2 f_\pi^4) = (16/35\pi^{6.5})\exp(2y)$ is given as a function of y in Table 5.7 and plotted in Figure 5.10.)

5.3.5 The Degenerate Nucleon Limit[31,42]

In the degenerate (D) nucleon limit ($y \gg 1$), Iwamoto[31] has shown the axion emission rate for the $nn \to nna$ process to be

$$\dot{\varepsilon}_a^{(D)} = \frac{31\sqrt{2}}{945\pi} m_N^{4.5} T^{6.5} g_{an}^2 \frac{f_\pi^4}{m_\pi^4} \sqrt{y}. \tag{5.72}$$

Brinkmann and Turner have verified this result. $\dot{\varepsilon}_a^{(ND)}/C_1$, where $C_1 = 4T^{6.5} m_N^{4.5} g_{an}^2 f_\pi^4$, is given as a function of y in Table 5.7 and plotted in Figure 5.10.

5.3.6 Arbitrary Degeneracy

Neither the degenerate nor the non-degenerate nucleon limits are appropriate for the nascent neutron star. Various authors[20,21,56,58,59] have used one or the other of these rates in order to derive bounds on axion parameters. Brinkmann and Turner[42] have computed the axion emission rate for arbitrary degeneracy in the non-relativistic limit with a constant matrix element. To perform the calculation

115

they first performed the γ_- and γ_c' integrations of equation (5.65) analytically and obtained

$$\dot{\varepsilon}_a = \frac{S \sum_{spins} |\mathcal{M}|^2 m_N^{0.5} T^{6.5}}{2^{5.5}\pi^7} \int_0^1 dq_+ \int_0^1 dq_- \int_0^1 dv$$

$$\times \frac{U_-^3(1-v)^2 q_+ q_-}{\sqrt{u_+}(e^{-2y} - q_+^2 q_-^2)(1 - e^{2y - 2vu_- - 2u_+})}$$

$$\times \ln\left(\frac{\cosh^2[(\sqrt{u_+} + \sqrt{u_-})^2/2 - y/2]}{\cosh^2[(\sqrt{u_+} - \sqrt{u_-})^2/2 - y/2]}\right) \ln\left(\frac{\cosh^2[(\sqrt{vu_-} + \sqrt{u_+})^2/2 - y/2]}{\cosh^2[(\sqrt{vu_-} - \sqrt{u_+})^2/2 - y/2]}\right),$$

$$(5.73)$$

which may be written as

$$\dot{\varepsilon}_a = S \sum_{spins} |\mathcal{M}|^2 m_N^{0.5} T^{6.5} I(y), \qquad (5.74)$$

where $v \equiv u_c'/u_-$ and $q_\pm \equiv e^{-u_\pm}$. They numerically evaluated this three dimensional integral and their results, accurate to within 1%, are shown in Table 5.7 and Figure 5.10 alongside the D and ND approximate rates. One can see that the rate for arbitrary degeneracy approaches the ND rate much more quickly than the D rate. Of the D and ND approximations the ND approximation is better in the conditions pertinent to the nascent neutron star.

As a check, I have used the relativistic integration technique of Section 5.2 with the constant matrix element assumed by Brinkmann and Turner. The results of this integration for $T = 1MeV$ and $50MeV$ are shown in Table 5.8 and are accurate to within 1%. We can see that the rates at 1MeV are almost identical to those of Brinkmann and Turner. This demonstrates that the NR approximation to the phase space integral is very good for $T = 1MeV$. For $T = 50MeV$ there is a small difference which reflects the small temperature dependence of the relativistic evaluation of the rate. However, the results shown in Table 5.8 are somewhat different to those obtained with the relativistic OPE or OBE matrix elements (see Tables 5.1 and 5.2, Section 5.2.5). In the next section I shall examine this discrepancy by introducing successively more refined approximations to the OPE matrix element.

Table 5.7 NR, OPE Constant Matrix Element Predictions of the Axion Energy Emission Rate per unit Volume after Brinkmann and Turner[42]. The values quoted are in units of $C_1 = 16ST^{6.5} m_N^{4.5} g_a^2 f_\pi^4 / m_\pi^4$.

$y = \frac{\hat{\mu}}{T}$	$\dot{\epsilon}_{a(C)}^{BTAD}/C_1$	$\dot{\epsilon}_{a(C)}^{ND}/C_1$	$\dot{\epsilon}_{a(C)}^{D}/C_1$
−10.0	5.53×10^{-13}	5.52×10^{-13}	−
−4.0	8.85×10^{-8}	8.99×10^{-8}	−
−3.5	2.38×10^{-7}	2.44×10^{-7}	−
−3.0	6.36×10^{-7}	6.64×10^{-7}	−
−2.5	1.68×10^{-6}	1.81×10^{-6}	−
−2.0	4.36×10^{-6}	4.91×10^{-6}	−
−1.5	1.10×10^{-5}	1.33×10^{-5}	−
−1.0	2.68×10^{-5}	3.63×10^{-5}	−
−0.5	6.17×10^{-5}	9.86×10^{-5}	−
0	1.32×10^{-4}	2.68×10^{-4}	0
0.5	2.61×10^{-4}	7.28×10^{-4}	2.61×10^{-3}
1.0	4.72×10^{-4}	1.98×10^{-3}	3.69×10^{-3}
1.5	7.79×10^{-4}	5.38×10^{-3}	4.52×10^{-3}
2.0	1.18×10^{-3}	1.46×10^{-2}	5.22×10^{-3}
2.5	1.67×10^{-3}	3.98×10^{-2}	5.83×10^{-3}
3.0	2.22×10^{-3}	1.08×10^{-1}	6.39×10^{-3}
3.5	2.82×10^{-3}	−	6.90×10^{-3}
4.0	3.43×10^{-3}	−	7.38×10^{-3}
5.0	4.64×10^{-3}	−	8.25×10^{-3}
6.0	5.77×10^{-3}	−	9.04×10^{-3}
8.0	7.75×10^{-3}	−	1.04×10^{-2}
10.0	9.37×10^{-3}	−	1.17×10^{-2}
50.0	2.52×10^{-2}	−	2.61×10^{-2}
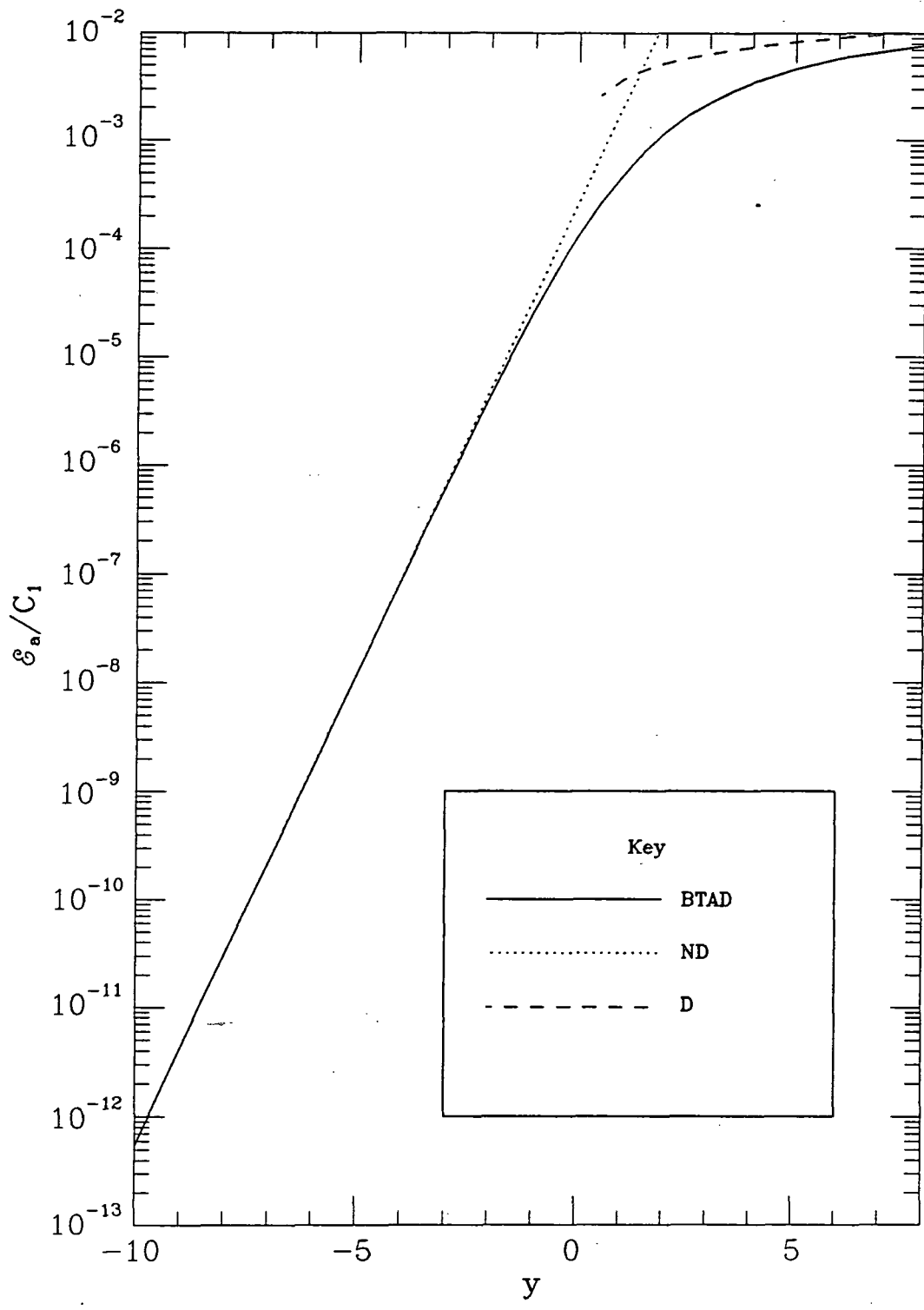
Figure 5.10 NR, OPE Constant Matrix Element Predictions of the Axion Energy Emission Rate per unit volume for Degenerate nucleons (D), Non-degenerate nucleons (ND) and Arbitrary Degeneracy of nucleons (BTAD) after Brinkmann and Turner[42].

Table 5.8   OPE Constant Matrix Element Predictions of the Axion Energy Emission Rate per unit Volume using Relativistic Phase Space. The values quoted are in units of $C_1 = 16ST^{6.5}m_N^{4.5}g_a^2 f_\pi^4/m_\pi^4$.

$y = \frac{\hat{\mu}}{T}$	$\dot{\varepsilon}_a^C/C_1$ $(T = 1MeV)$	$\dot{\varepsilon}_a^C/C_1$ $(T = 50Mev)$
$-10.$	5.53×10^{-13}	5.25×10^{-13}
$-9.$	4.09×10^{-12}	3.88×10^{-12}
$-8.$	3.02×10^{-11}	2.87×10^{-11}
$-7.$	2.23×10^{-11}	2.12×10^{-11}
$-6.$	1.64×10^{-09}	1.56×10^{-09}
$-5.$	1.21×10^{-08}	1.15×10^{-08}
$-4.$	8.85×10^{-08}	8.34×10^{-08}
$-3.$	6.35×10^{-07}	6.03×10^{-07}
$-2.$	4.35×10^{-06}	4.13×10^{-06}
$-1.$	2.67×10^{-05}	2.54×10^{-05}
$0.$	1.32×10^{-04}	1.24×10^{-04}
$2.$	1.18×10^{-03}	1.14×10^{-03}
$4.$	3.42×10^{-03}	3.50×10^{-03}

5.3.7 Successive Approximations to the OPE Axion Energy Emission Rate for Arbitrary Degeneracy

Table 5.9 and Figure 5.11 show four different approximations to the OPE $nn \rightarrow nna/pp \rightarrow ppa$ axion emission rates. All of these approximations use the relativistic version of the phase space integrals and only differ in the approximation to the OPE matrix element which is used to describe the process. The first column in Table 5.9 gives the values, $\dot{\varepsilon}_a^{(C)}/C_1$, computed using the constant matrix element approximation. For the values in the second column, $\dot{\varepsilon}_a^I/C_1$, Iwamoto's[31] spin summed matrix element, equation (5.58), was employed. The matrix element

$$\sum_{spins} |\mathcal{M}|^2 = \frac{256}{3}(2m_N g_{an})^2 \frac{f_\pi^4}{m_\pi^4} m_N^2$$

$$\left[\left(\frac{\Lambda^2 - m_\pi^2}{\Lambda^2 + p_k^2} \right)^4 \frac{p_k^4}{(p_k^2 + m_\pi^2)^2} + \left(\frac{\Lambda^2 - m_\pi^2}{\Lambda^2 + p_l^2} \right)^4 \frac{p_l^4}{(p_l^2 + m_\pi^2)^2} \right. \tag{5.75}$$

$$\left. + \left(\frac{\Lambda^2 - m_\pi^2}{\Lambda^2 + p_k^2} \right)^2 \left(\frac{\Lambda^2 - m_\pi^2}{\Lambda^2 + p_l^2} \right)^2 \frac{p_k^2 p_l^2}{(p_k^2 + m_\pi^2)(p_l^2 + m_\pi^2)} \right],$$

which is the same as Iwamoto's except that $\pi - N - N$ vertex form factors have been introduced, was used to cmopute the values in the third column, $\dot{\varepsilon}_a^{IF}/C_1$. The fourth column gives the values determined using the relativistic OPE matrix element, $\dot{\varepsilon}_a^\pi/C_1$. One can see a definite progression towards the relativistic OPE results. It seems that the largest source of error in the constant matrix element approximation is the omision of a form factor at the $\pi - N - N$ vertices. The ratio $(\dot{\varepsilon}_a^C/C_1)/(\dot{\varepsilon}_a^\pi/C_1)$ is ~ 4 at $y = -10$, and the ratio $(\dot{\varepsilon}_a^C/C_1)/(\dot{\varepsilon}_a^{IF}/C_1)$ is ~ 2, whereas the ratio $(\dot{\varepsilon}_a^C/C_1)/(\dot{\varepsilon}_a^I/C_1)$ at $y = -10$ is 1.2. Higher values of y lead to a similar conclusion.

If one includes Brinkmann and Turner's β dependence[42] the constant matrix element is slightly improved; for example, at $y = -10$ with $\beta = 1.0845$ $\dot{\varepsilon}_a^C/C_1$ becomes $\sim 3.5 \times 10^{-13}$.

5.3.8 np Axion Emission Rates Using the Constant Matrix Element Approximation

I have computed the $np \to npa$ axion production rates with $g_{an} = g_{ap} = g_a$ using the relativistic version of the phase space and employing the OPE constant matrix element approximation ($\beta = 0$). The values obtained are shown in Table 5.10 which gives $\dot{\varepsilon}_a^{Cnp}/C_1$ as a function of $\bar{y}$ and Δy at $T = 50 MeV$. Table 5.11 shows the corresponding rates as calculated by Brinkmann and Turner[42]. The two sets of data show reasonable agreement as was the case for the nn/pp rates. Note that in Table 5.11 the emission rates are given in units of $C_T = 16 S T^{6.5} m_N^{4.5} g_{aN} f_\pi / m_\pi$ rather than in units of C_1. g_{aN} is defined by[42] [1],

$$g_{aN}^2 \equiv \frac{15 - 2\beta}{9} \left(\frac{g_{an}^2 + g_{ap}^2}{2} \right) + \frac{6 - 4\beta}{9} \left(\frac{g_{an} + g_{ap}}{2} \right)^2, \tag{5.76}$$

---

[1] N.B. In Brinkmann and Turner's work g_{aN} represents the effective pseudoscalar coupling constant. Here g_{aN} represents the pseudovector coupling constant so as to be consistent with the earlier use of g_a, g_{an} and g_{ap}.

Table 5.9 Successive OPE Approximations to the nn/pp Axion Energy Emission Rate per unit Volume as described in the text. The values quoted are in units of $C_1 = 16ST^{6.5}m_N^{4.5}g_a^2 f_\pi^4/m_\pi^4$.

| $y = \frac{\hat{\mu}}{T}$	$\dot{\epsilon}_a^C/C_1$	$\dot{\epsilon}_a^I/C_1$	$\dot{\epsilon}_a^{IF}/C_1$	$\dot{\epsilon}_a^\pi/C_1$
−10.	5.3×10^{-13}	4.4×10^{-13}	2.5×10^{-13}	1.6×10^{-13}
−9.	3.9×10^{-12}	3.2×10^{-12}	1.9×10^{-12}	1.2×10^{-12}
−8.	2.9×10^{-11}	2.4×10^{-11}	1.4×10^{-11}	8.8×10^{-12}
−7.	2.1×10^{-10}	1.8×10^{-10}	1.0×10^{-10}	6.5×10^{-11}
−6.	1.6×10^{-9}	1.3×10^{-9}	7.5×10^{-10}	4.8×10^{-10}
−5.	1.2×10^{-8}	9.5×10^{-9}	5.5×10^{-9}	3.5×10^{-9}
−4.	8.4×10^{-8}	7.0×10^{-8}	4.0×10^{-8}	2.6×10^{-8}
−3.	6.0×10^{-7}	5.0×10^{-7}	2.9×10^{-7}	1.9×10^{-7}
−2.	4.1×10^{-6}	3.4×10^{-6}	2.0×10^{-6}	1.3×10^{-6}
−1.	2.5×10^{-5}	2.1×10^{-5}	1.2×10^{-5}	7.9×10^{-6}
0.	1.3×10^{-4}	1.1×10^{-4}	5.9×10^{-5}	4.0×10^{-5}
1.	4.5×10^{-4}	3.9×10^{-4}	2.0×10^{-4}	1.4×10^{-4}
2.	1.1×10^{-3}	9.7×10^{-4}	4.7×10^{-4}	3.6×10^{-4}
3.	2.1×10^{-3}	1.9×10^{-3}	8.2×10^{-4}	6.9×10^{-4}
4.	3.4×10^{-3}	3.1×10^{-3}	1.2×10^{-3}	1.0×10^{-3}
5.	4.6×10^{-3}	4.1×10^{-3}	1.5×10^{-3}	1.5×10^{-3}
6.	6.0×10^{-3}	5.4×10^{-3}	1.8×10^{-3}	1.9×10^{-3}
8.	8.2×10^{-3}	7.6×10^{-3}	2.0×10^{-3}	2.1×10^{-3}
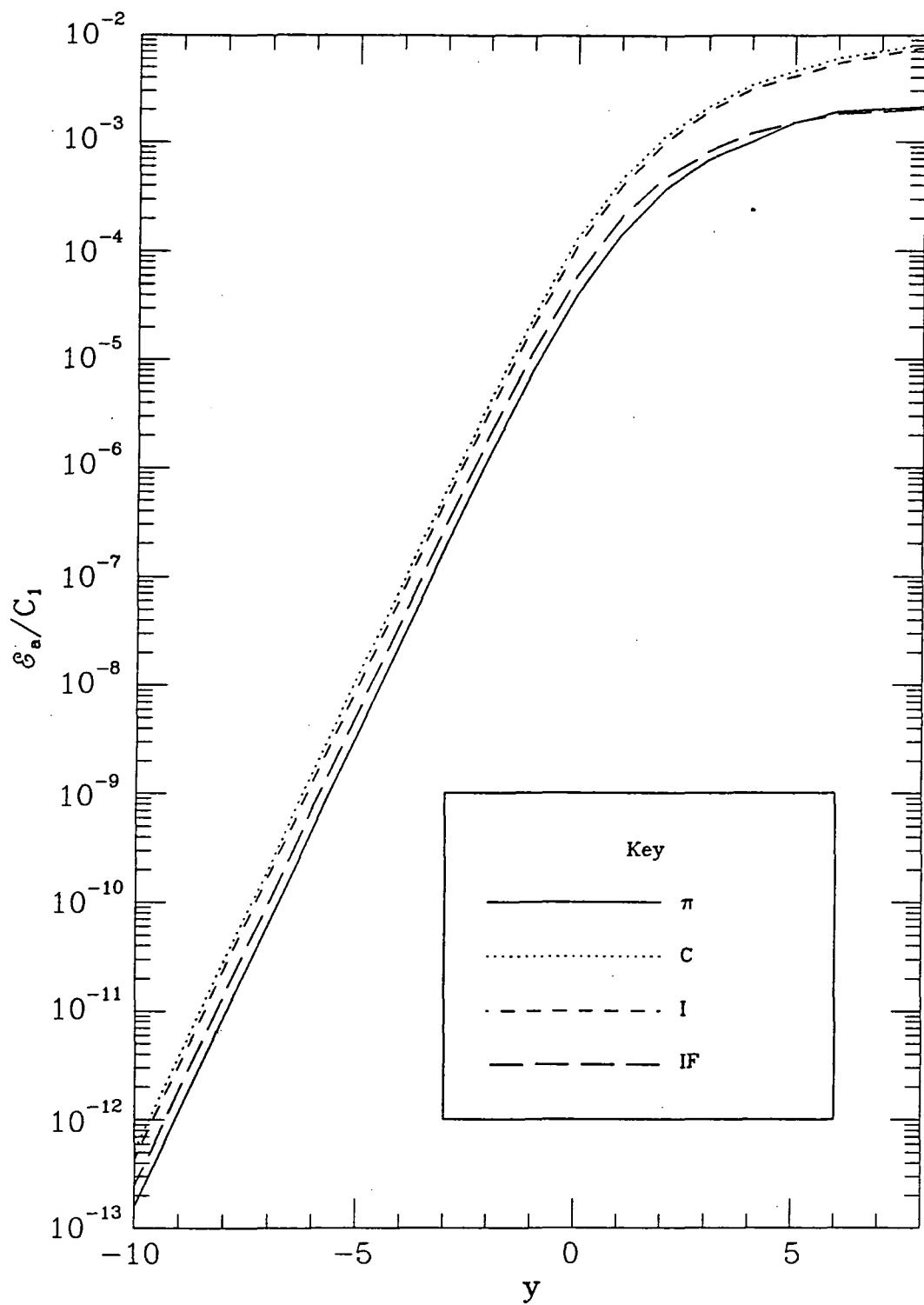
Figure 5.11 Successive OPE Approximations to the nn/pp Axion Energy Emission Rate as described in the text.

Table 5.10 OPE Constant Matrix Element Approximation Predictions of the Axion Emission Rates per unit volume for $np \to npa$ at $T = 50Mev$. The values quoted are in units of $C_1 = 16ST^{6.5}m_N^{4.5}g_a^2 f_\pi^4/m_\pi^4$.

$\bar{y}$	$\Delta y = 0$	$\Delta y = 2$	$\Delta y = 4$	$\Delta y = 6$	$\Delta y = 8$	$\Delta y = 10$
-10	5.3×10^{-13}	5.3×10^{-13}	5.3×10^{-13}	5.2×10^{-13}	5.0×10^{-13}	3.7×10^{-13}
-8	2.9×10^{-11}	2.9×10^{-11}	2.8×10^{-11}	2.7×10^{-11}	2.0×10^{-11}	8.1×10^{-12}
-6	1.6×10^{-9}	1.6×10^{-9}	1.5×10^{-9}	1.1×10^{-9}	4.4×10^{-10}	9.6×10^{-11}
-4	8.4×10^{-8}	8.1×10^{-8}	6.0×10^{-8}	2.3×10^{-8}	5.2×10^{-9}	8.6×10^{-10}
-2	4.1×10^{-6}	3.2×10^{-6}	1.3×10^{-6}	2.9×10^{-7}	4.7×10^{-8}	6.9×10^{-9}
0	1.3×10^{-4}	6.6×10^{-5}	1.5×10^{-5}	2.5×10^{-6}	3.7×10^{-7}	5.3×10^{-8}
2	1.1×10^{-3}	6.0×10^{-4}	1.3×10^{-4}	2.1×10^{-5}	2.9×10^{-6}	4.0×10^{-7}
4	3.4×10^{-3}	2.3×10^{-3}	8.0×10^{-4}	1.4×10^{-4}	2.2×10^{-5}	3.0×10^{-6}
6	6.0×10^{-3}	4.8×10^{-3}	2.8×10^{-3}	8.5×10^{-4}	1.6×10^{-4}	2.3×10^{-5}
8	8.2×10^{-3}	7.1×10^{-3}	5.0×10^{-3}	2.7×10^{-3}	8.8×10^{-4}	1.7×10^{-4}

Table 5.11 NR OPE Constant Matrix Element Approximation Predictions of the Axion Emission Rate per unit volume for $np \to npa$ from Brinkmann and Turner[42]. The values quoted are in units of $C_T = 16ST^{6.5}m_N^{4.5}g_{aN}^2 f_\pi^4/m_\pi^4$.

$\bar{y}$	$\Delta y = 0$	$\Delta y = 2$	$\Delta y = 4$	$\Delta y = 6$	$\Delta y = 8$	$\Delta y = 10$
-10	5.53×10^{-13}	5.53×10^{-13}	5.53×10^{-13}	5.49×10^{-13}	5.21×10^{-13}	3.88×10^{-13}
-8	3.02×10^{-11}	3.02×10^{-11}	3.00×10^{-11}	2.84×10^{-11}	2.12×10^{-11}	8.41×10^{-12}
-6	1.65×10^{-9}	1.64×10^{-9}	1.55×10^{-9}	1.16×10^{-9}	4.59×10^{-10}	1.00×10^{-10}
-4	8.86×10^{-8}	8.47×10^{-8}	6.31×10^{-8}	2.51×10^{-8}	5.46×10^{-9}	8.91×10^{-10}
-2	4.36×10^{-6}	3.42×10^{-6}	1.37×10^{-6}	2.98×10^{-7}	4.86×10^{-8}	7.12×10^{-9}
0	1.32×10^{-4}	7.05×10^{-5}	1.61×10^{-5}	2.65×10^{-6}	3.89×10^{-7}	5.47×10^{-8}
2	1.18×10^{-3}	6.35×10^{-4}	1.37×10^{-4}	2.11×10^{-5}	2.98×10^{-6}	4.13×10^{-7}
4	3.43×10^{-3}	2.41×10^{-3}	8.29×10^{-4}	1.54×10^{-4}	2.24×10^{-5}	3.09×10^{-6}
6	5.77×10^{-3}	4.79×10^{-3}	2.70×10^{-3}	8.77×10^{-4}	1.60×10^{-4}	2.29×10^{-5}
8	7.75×10^{-3}	6.92×10^{-3}	5.05×10^{-3}	2.78×10^{-3}	8.98×10^{-4}	1.63×10^{-4}

which for $g_{an} = g_{ap} = g_a$ and $\beta = 0$ gives

$$g_{aN}^2 = \frac{7g_a^2}{3},$$ (5.77)

which would imply that the two sets of emission rates from Tables 5.10 and 5.11 are not the same. However the definition (5.76) contains the error in isospin factors which was discussed in Section 5.2.4.2. Correcting this error gives an alternative definition for g_{aN},

$$g_{aN}^2 \equiv \frac{3+2\beta}{9}\left(\frac{g_{an}^2 + g_{ap}^2}{2}\right) + \frac{6+4\beta}{9}\left(\frac{g_{an} + g_{ap}}{2}\right)^2,$$ (5.78)

which for $g_{an} = g_{ap} = g_a$ and $\beta = 0$ gives

$$g_{aN}^2 = g_a^2,$$ (5.79)

and thus the two tables *are* equivalent provided one uses the correct definition for g_{aN}.

5.4 Conclusion: Axion Emission Rates and Bounds

In Section 5.2 I presented the results of numerical evaluations of the axion emission rate which assume that the OBE approximation is valid but do not involve any approximations concerning the momenta involved. In Section 5.3 I discussed the various approximations which have been employed by other authors. The non-relativistic OPE constant matrix element approximation (see Section 5.3.2.2.) has been the most widely used. I shall take this to be the base case and discuss the changes to axion emission rate which result from improving upon this approximation.

In Section 5.3.3.3 the conclusion was reached that the non-relativistic approximation to the phase space integrals performs well, particularly in the non-degenerate nucleon limit ($y << -1$).

The constant matrix element approximation is not as satisfactory. For the nn/pp emission rates the largest source of error is the omission of the $\pi - N - N$ form factors (see Section 5.3.3.5). The maximum ratio between the constant matrix

element rate (with $\beta = 0$) and the fully relativistic OPE rate is ~ 3. Including additional exchanged mesons makes little difference to the emission rates, the change is at most a factor of ~ 1.5. This conclusion contradicts an earlier study by Ericson and Mathiot which suggests that adding ρ exchange reduced the emission rate by a factor of $\sim \frac{1}{6}$.

The situation is different for the np rates. Firstly, previous constant matrix element treatments of this rate were incorrect as isospin was not treated correctly (see Section 5.2.4.2). Correcting previous constant matrix element results lead to a reduction in the np emission rate by a factor of ~ 2 ($\beta = 0$). The fully relativistic OPE rates are quite similar to the constant matrix element results except at high $\bar{y}$ and high Δy. However, adding all seven considered additional exchanges gives a maximum reduction factor of ~ 3 at $\Delta y = 0$ which is much more significant than was the case for the nn/pp rates. For higher Δy the reduction factor is even greater.

The largest change in the axion emission rates resulted from using a reduced effective kinematical mass for the nucleon $m_N^* = 0.5 m_N$. This reduced the emission rate by a factor of as much as ~ 20 for OPE alone. This result is only preliminary since the variation of the coupling constants ($g_a, f_\pi, g_\sigma \ldots etc.$) and masses, other than the nucleon mass, ($m_\pi, m_\sigma \ldots etc.$) was not considered. However, the large reduction in the emission rate which is caused by changing only the effective nucleon mass suggests that a more comprehensive study of the density dependence of the axion emission rate is required. Changes to the effective masses and couplings have the potential to significantly alter the derived axion emission rate. Other authors[5,56] have considered high density effects on the axion emission rate by substituting effective masses and couplings into approximate, non-relativistic expressions for the emission rate. However such non-relativistic expressions may not be sufficiently accurate when $m_N^* \simeq 0.5 m_N$. In the conditions of the nascent neutron star nucleon fermi momenta $O(\sim 100 MeV)$ are not unreasonable.

In order to assess concretely the effect that changes in the axion emission rate have on subsequently derived bounds, one should use the altered rates in conjunction with a nascent neutron star simulation code such as those of Mayle et al[20,21] and Burrows et al[32]. If one does not do this one cannot properly account for the affect of axion energy drain on the conditions within the core. If we assume that the core conditions are not altered and take the maximum factor

by which axion emission rates change, as discussed above, then we can obtain a crude estimate of affect on the axion bounds. Since $\dot{\epsilon}_a$ is proportional to g_a^2 an upper bound on g_a of B_g, i.e.,

$$g_a \lesssim B_g$$

will become,

$$g_a \lesssim \frac{B_g}{\sqrt{R}}$$

when the axion emission rates are reduced by a factor of R. I shall take a maximum reduction factor of 6 to relate to the reduction in the axion emission rate induced by using relativistic expressions with the full OBE model amplitudes. The factor of 6 is for $\Delta y = \bar{y} = 0$ and contains a factor of ~ 2 from the correction of the isospin treatment and a factor of 3 from the introduction of more complexity into the axion production matrix element. This factor implies an altered bound of,

$$g_a \lesssim B_g \sqrt{6}$$

which can be converted into bounds on F_a and m_a of

$$F_a \gtrsim B_F / \sqrt{6}$$

and,

$$m_a \lesssim B_m \sqrt{6}$$

where B_F and B_m are the original bounds on the axion decay constant and mass respectively. Table 5.12 show the effect this factor has on the bounds published by Mayle et al[21] and Burrows et al [32].

The results of table 5.12 imply that the bounds which were derived using non-relativistic expressions and the constant matrix element approximation are not changed much when the more complete approach of Section 5.2 is used. When we consider the other possible sources of error, the details of supernovae theory and the sparsity of neutrino detections from SN1987A, this error in the emission rates is not very significant. The change of the emission rate when a reduced nucleon mass is used is much more significant and warrants further investigation of density dependent effects.

126

Table 5.12   The Changes to the Published Bounds which Result when the Axion Emmission Rate is Reduced by a Factor of 6.

Authors	Published Bounds		Revised Bounds	
	F_a ($10^9 GeV$)	m_a ($10^{-3} eV$)	F_a ($10^9 GeV$)	m_a $10^{-3} eV$
Mayle et al[21]				
(NQM)	$\gtrsim 17$	$\lesssim 0.36$	$\gtrsim 6.9$	$\lesssim 0.88$
(EMC)	$\gtrsim 4.3$	$\lesssim 1.4$	$\gtrsim 1.8$	$\lesssim 3.4$
Burrows et al[32]				
(NQM)	$\gtrsim 6.0$	$\lesssim 1.0$	$\gtrsim 2.4$	$\lesssim 2.4$

References

1. R.D.Peccei and H.R.Quinn, *Phys. Rev. Lett.* **38**, 223 (1978).

2. R.D.Peccei and H.R.Quinn, *Phys. Rev.* **D16**, 1791 (1977).

3. P. Sikivie, UF-TP-83-6 (1983).

4. P. Sikivie, UF-TP-86-28 (1986).

5. G.G. Raffelt, *Phys. Rep.* **198**, 1 (1990).

6. H.-Y. Cheng, *Phys. Rep.* **158**, 1 (1988).

7. J.E. Kim, *Phys. Rep.* **150**, 1 (1987).

8. F. Halzen and A.D. Martin, in *Quarks and Leptons: An Introductory Course in Modern Particle Physics* (Wiley Interscience,1984).

9. P.D.B. Collins, A.D. Martin and E.J. Squires, in *Particle Physics and Cosmology* (Wiley Interscience,1989).

10. V. Baluni, *Phys. Rev.* **D19**, 2227 (1979).

11. R.J. Crewther, P. Di Vecchia, G. Veneziano and E.Witten, *Phys. Lett.* **B88**, 123 (1979).

12. S.Weinberg, *Phys. Rev. Lett.* **40**, 1223 (1978).

13. F.Wilczek, *Phys. Rev. Lett.* **40**, 279 (1978).

14. J.E.Kim, *Phys. Rev. Lett.* **43**, 103 (1979).

15. M.Dine, W.Fischler and M.Srednicki, *Phys. Lett.* **B104**, 199 (1981).

16. N.Iwamoto, *Phys. Rev.* **D39**, 2120 (1989).

17. M.Carena and R.D.Peccei, *Phys. Rev.* **D40**, 652 (1989).

18. D.B.Kaplan, *Nucl. Phys.* **B260**, 215 (1985).

19. M.Srednicki, *Nucl. Phys.* **B260**, 689 (1985).

20. R.Mayle, J.R.Wilson, J.Ellis, K.Olive, D.N.Schramm and G.Steigman, *Phys. Lett.* **B203**, 188 (1988).

21. R.Mayle, J.R.Wilson, J.Ellis, K.Olive, D.N.Schramm and G.Steigman, *Phys. Lett.* **B229**, 515 (1989).

22. J.Ellis and R.Flores, *Phys. Lett.* **B198**, 393 (1987).

23. D.B.Kaplan and A.Manohar, HUTP-88/A021 (1988).

24. J.Ellis and M.Karliner, *Phys. Lett.* **B213**, 73 (1988).

25. Particle Data Group, *Phys. Lett.* **B239**, (1990). .

26. A.Pantziris and K.Kang, *Phys. Rev.* **D33**, 3509 (1986).

27. G.Raffelt, *Phys. Rev.* **D33**, 897 (1986).

28. D.S.P.Dearborn, D.N.Schramm and G.Steigman, *Phys. Rev. Lett.* **56**, 26 (1986).

29. G.Raffelt and D.Dearborn, *Phys. Rev.* **D36**, 2211 (1987).

30. M.Nakagwa, T.Adachi, Y.Kokyama and N.Itoh, *Astrophys. J* **326**, 241 (1988).

31. N.Iwamoto, *Phys. Rev. Lett.* **56**, 26 (1986).

32. A.Burrows, M.S.Turner and R.P.Brinkmann, *Phys. Rev.* **D39**, 1020 (1989).

33. R.L.Davis and E.P.S.Shellard, *Nucl. Phys.* **B324**, 167 (1989).

34. D.Harari and P.Sikivie, *Phys. Lett.* **B195**, 361 (1987).

35. J.N.Bahcall, in *Neutrino Astrophysics* (Cambridge University Press,1989).

36. R.J.Taylor, in *The Stars: Their Structure and Evolution* (Wykeham Publications Ltd.,1970).

37. T.J.Haines *et al*, *Phys. Rev. Lett.* **57**, 1986 (1986).

38. M.Nakahata *et al*, *Phys. Rev.* **55**, 3786 (1986).

39. K.S.Hirata, T.Kajita, M.Koshoba, *et al*, *Phys. Rev. Lett.* **58**, 1490 (1987).

40. R.M.Bonita *et al*, *Phys. Rev. Lett.* **58**, 1494 (1987).

41. T.J.Loredo and D.D.Lamb, *Ann. N.Y. Acad. Sci.* **571**, 601 (1989).

42. R.P. Brinkmann and M.S. Turner, *Phys. Rev.* **D38**, 2338 (1988).

43. A.Burrows, M.T.Ressel and M.S.Turner, Fermilab-Pub-90/81-A (1990).

44. K.Holinde, *Phys. Rep.* **68**, 121 (1981).

45. K.Erkelenz, *Phys. Rep.* **13C**, 191 (1974).

46. R.Machleidt, K.Holinde and Ch.Elster, *Phys. Rep.* **149**, 1 (1987).

47. İn *The NAG Fortran Library Manual* (The Numerical Algorithms Group Limited, 1988).

48. J.Bystricky and F.Lehar, in *Nucleon-Nucleon Scattering Data Nr11-1* (Fach-informationszentrum, 1978).

49. V.Flaminio, W.G.Moorhead, D.R.O.Morrison and N.Rivoire, CERN-HERA 84-01 (1984).

50. B.J.VerWest and R.A.Arndt, *Phys. Rev.* **C25**, 1979 (1982).

51. M.S.Turner, H.-S.Kang and G.Steigman, Fermilab-Pub-88/204-A (1988).

52. H.Georgi, in *Weak Interactions and Modern Particle Theory* (Benjamin / Cummins, 1984).

53. A.Konig and P.Kroll, *Nucl. Phys* **A356**, 345 (1981).

54. K.Choi, K.Kang and J.E.Kim, *Phys. Rev. Lett.* **62**, 849 (1989).

55. E.Byckling and K.Kajantie, in *Particle Kinematics* (Wiley and Sons, 1973).

56. T.E.O.Ericson and J.-F.Mathiot, *Phys. Lett.* **B219**, 507 (1989).

57. R.P. Brinkmann and M.S. Turner, *Phys. Rev.* **D38**, 2338 (1988).

58. M.S.Turner, *Phys. Rev. Lett.* **60**, 1797 (1988).

59. G.G.Raffelt and D.Seckel, *Phys. Rev. Lett.* **60**, 1793 (1988).